UNIVERSITY OF SOUTHAMPTON

FACULTY OF SOCIAL AND HUMAN SCIENCES

School of Mathematics

Mathematical Modelling of Lithium Ion Batteries

by

Rahifa Ranom

Thesis for the degree of Doctor of Philosophy

October 2014

UNIVERSITY OF SOUTHAMPTON

ABSTRACT

FACULTY OF SOCIAL AND HUMAN SCIENCES
School of Mathematics

Doctor of Philosophy

MATHEMATICAL MODELLING OF LITHIUM ION BATTERIES

by Rahifa Ranom

In this study, we discuss a lithium battery model based on dilute electrolyte theory and fast diffusion of lithium in the electrode particle and calculate some novel solutions to the model. We then discuss moderately concentrated electrolyte theory and outline how homogenisation techniques can be applied to this theory, in combination with a microscale model for lithium transport in the electrode particles in order to derive a Newman type model of the battery [59]. We formulate a numerical method, based on the method of lines in order to solve this model, and apply it to the cases of a half cell graphite anode and a half cell $LiFePO_4$ cathode. In both scenarios, the results show very good agreement to experimental discharge curves.

Contents

DECLARATION OF AUTHORSHIP **xv**

List of Publications **xvii**

Acknowledgements **xix**

1 Introduction **1**
1.1 Lithium batteries as energy storage solution 1
1.2 Battery materials for Lithium ion batteries 3
1.2.1 Desirable electrode and electrolyte properties 3
1.2.2 The cathode material 4
1.2.3 The anode material 4
1.2.4 The electrolyte 5
1.3 Charge-transfer reaction 5
1.4 Battery Terminology 6
1.5 The half-cell 7
1.6 Battery modelling 9
1.6.1 Statement of originality 10

2 Dilute electrolyte modelling of battery **13**
2.1 Introduction 13
2.2 Derivation of a model for a dilute electrolyte 13
2.2.1 Charge neutrality 14
2.3 Reaction kinetics on the electrode particle surfaces 15
2.4 The electrode particles 17
2.5 Homogenisation of model accounting for microstructure on electrode particle scale 19
2.5.1 The current collectors 21
2.5.2 The separator 21
2.5.3 The initial conditions 21
2.5.4 The relation between current and global reaction rate 22
2.5.5 Summary of the battery model and comparison to other models . . 22
2.6 Numerical and analytical solutions for the full cell model 23
Equilibrium solution 24
2.6.1 Nondimensionalization 24
2.6.1.1 Size of dimensionless parameters 26
2.6.2 The Tafel equation approximation for $\Omega_a << 1$ and $\Omega_c << 1$ . . . 27
2.6.3 The quasi steady approximations for $\Gamma << 1$ 27

2.6.4 Solution for flat discharge curves . . . 28
Solution before the particles are fully discharged. . . . 29
Numerical procedure . . . 30
2.6.5 Results and Discussion . . . 30
2.7 The half cell cathode model . . . 33
2.7.1 Quasi-steady state limit $\Gamma \to 0$ . . . 35
2.7.2 Flat discharge curve approximation for $LiFePO_4$ cathode . . . 36
2.7.3 Analytic solutions . . . 37
2.7.3.1 Before the development of a free boundary . . . 37
Numerical solution procedure . . . 38
2.7.3.2 After development of free boundary . . . 38
Numerical solution procedure . . . 39
2.7.3.3 Results and discussion . . . 40
2.8 Summary . . . 41

3 Modelling moderately concentrated electrolytes 45
3.1 Introduction . . . 45
3.2 Stefan-Maxwell equations . . . 46
3.2.1 Chemical potential ($\bar{\mu}$) and electrochemical potential (μ) of the electrolyte at constant pressure and temperature . . . 46
Chemical potential . . . 46
Electrochemical potential . . . 47
3.3 The Stefan Maxwell equations for the binary 1:1 electrolyte . . . 47
Averaged approximation to Poisson's equation . . . 48
Non-dimensionalising Poisson's equation . . . 49
Charge neutrality . . . 50
Equations for the current density $\mathbf{j}$ . . . 50
Derivation of the ion velocities in terms of the electrolyte chemical potential μ_e and $\boldsymbol{j}$. . . . 52
Diffusion equation for the electrolyte concentration . . . 53
3.3.1 Summary of model for moderately concentrated electrolyte . . . 53
3.3.2 An ideal solution . . . 54
3.3.3 How might we deal with the electric potential . . . 54
3.3.4 The potential measured with respect to Lithium electrode . . . 55
Remarks . . . 56
3.4 Thermodynamic fitting to data . . . 56
3.5 Summary . . . 58

4 Review of homogenisation technique for moderately concentrated electrolyte model 59
4.1 Introduction . . . 59
4.2 The cell scale electrolyte equations by homogenisation technique . . . 60
Boundary conditions on the surface of the electrode particles 60
General set of microscale electrolyte equations. . . . 61
The asymptotic expansions. . . . 62
The solution to the moderately concentrated electrolyte model. . . . 64

4.3 Butler-Volmer reaction equations . . . 64
4.3.1 The general version of Butler-Volmer equations for insertion material 64
4.3.2 The Butler-Volmer equations of electrode materials for lithium battery . . . 67
LiC_6 anode material . . . 67
$LiFePO_4$ and $LiCoO_2$ cathode materials . . . 67
4.4 Summary of the resulting model . . . 68
4.4.1 Boundary conditions for the full cell battery . . . 69
4.5 Summary . . . 70

5 Models for electrode particles 71
5.1 Introduction . . . 71
5.2 Two phase Lithium insertion/extraction . . . 71
5.2.1 "Shrinking-core" model . . . 73
Nondimensionalisation . . . 74
5.2.1.1 Solution Procedure . . . 76
5.2.1.2 Asymptotic solution of shrinking core diffusion . . . 77
Summary. . . . 78
5.2.2 Phase-field model . . . 79
5.3 More than two phases . . . 80
5.4 Diffusion equation in the spherical coordinate . . . 81
Current density in the electrode . . . 81
5.5 Summary . . . 82

6 Numerical Procedure 83
6.1 Introduction . . . 83
6.2 Method of Lines . . . 85
6.3 Development of sparse matrix for the system . . . 86
6.3.1 The development of the solution vector $\boldsymbol{u}$ . . . 87
6.3.2 The development of matrices for electrolyte concentration, c . . . 88
Summary . . . 89
6.3.3 The development of matrices for electrolyte potential, $\hat{\phi}$ . . . 89
6.3.4 The development of matrices for the electrode potential, $\hat{\phi}_s$ . . . 90
6.3.5 The development of matrices for concentration in the electrode particles, c_s . . . 91
6.3.6 The development of $\boldsymbol{A}$, $\boldsymbol{M}$ and $\boldsymbol{f}$ . . . 93
6.4 ode15s . . . 93
Convergence . . . 94
6.5 Summary . . . 96

7 The Half cell Anode 97
7.1 Introduction . . . 97
7.2 The half cell anode model . . . 97
7.3 Nondimensionalisation . . . 99
Remarks. . . . 99
Discussion of dimensionless parameters . . . 101
7.4 Model - experimental comparisons for the natural graphite electrode . . . 102
7.4.1 Results and Discussions . . . 104

7.4.1.1 An approximation solution . . . 107
Summary . . . 108
7.4.1.2 Concentration-dependent of diffusion coefficient . . . 108
7.5 Summary . . . 112

8 Half cell cathode **115**
8.1 Introduction . . . 115
8.2 Transport data and parameter values used in the simulation . . . 116
8.2.1 Nondimensionalisation . . . 118
Parameter Values . . . 119
Numerical Procedure . . . 121
8.3 Model-experimental comparison . . . 121
8.4 The effects of parameter variations on the discharge of a nanostructured half-cell cathode . . . 123
8.5 Summary . . . 136

9 Conclusions and Future Works **137**
9.1 Conclusions . . . 137
9.2 Future works . . . 139
The effect of different sizes of particles . . . 139
The effect of changes in particle shape and packing upon cell performance . . . 139

List of Figures

1.1 A schematic diagram of the Lithium Ion Battery during discharge [59]. The current flowing out of the positive electrode drives the extraction of lithium ion from negative electrode (anode) particles to the electrolyte across the porous separator (by diffusion and advection) into the positive electrode (cathode) and insert into the positive electrode (cathode). The charge of electrons are moving from the negative electrode particles to the negative electrode current collector and from the positive electrode current collector to the positive electrode particles. 2

1.2 Structure of the electric double layer near a solid electrolyte interface when external electric field is applied. The electric drops linearly from the electrode potential ϕ_s to the electrolyte potential ϕ in a thin layer. . . 6

1.3 Schematic diagram for typical half cell anode. The cathode material is a lithium-foil which is reacting as reference electrode. During discharge, the Lithium ions are conducted through the electrolyte solution to the lithium electrode. Here $x^* = 0$ is the anode current collector and $x^* = L$ is the separator. 8

1.4 A schematic diagram for a typical half-cell cathode. The anode material is a lithium-foil. Here $x^* = 0$ is the separator and $x^* = L$ is at cathode current collector 8

2.1 Reaction rate on the solid electrolyte interface in anode and cathode. . . . 15

2.2 Different types of open circuit potential i.e. $U^*_{eqc}(y)$ curves for different cathode materials with respect to the insertion chemistry of the materials, y (normalized capacity). 17

2.3 Different types of open circuit potential i.e $U^*_{eqa}(x)$ curves for different anode materials with respect to the insertion chemistry of the materials, x (normalized capacity). 18

2.4 Schematic representation of the mathematical domains in particle scale. . 20

2.5 The solution of dimensionless electrolyte potential, $\tilde{\phi}(x)$ from (symbols) analytical expression (2.91) compared to (line) numerical simulation using MATLAB 'bvp4c' at discharge current $\bar{I} = 1.32$. 31

2.6 Graph of dimensionless electrolyte concentration $c(x)$ at different discharge currents $\bar{I} = 1.0, 1.2, 1.4, 1.7$ as a function of position. This analytical solutions are obtained by equation (2.91). 32

2.7 Graph of dimensionless electrolyte potential $\tilde{\phi}(x)$ at different discharge currents $\bar{I} = 1.0, 1.2, 1.4, 1.7$ as a function of position. This figure is obtained by relation to the electrolyte concentration as stated in (2.77). . 32

2.8 Dimensionless intercalated Lithium concentration distribution in the particle for anode ($0 < x < 1$) and cathode ($1 < x < 2$), c_{sa} and c_{sc}, respectively (by solving (2.88)-(2.90) numerically) for discharge current (a) $\bar{I} = 1$ and (b) $\bar{I} = 1.5$. Here $0 < x < 1$ is the anode and $1 < x < 2$ is the cathode. The profiles are measured at $t^* = 100s, 200s, 300s, 400s, ...$ 34
2.9 The free boundary problem; (a) $x < s(t)$ - Cathode particles are full with Lithium ($c_{sc} = 1$) and (b) $x > s(t)$ - Cathode particles are partially filled ($c_{sc} < 1$) 36
2.10 Dimensionless concentration profiles of the model before the free boundary develops by (symbol) analytical solution (2.119) and (solid line) numerical simulation for $\bar{I} = 1$. 40
2.11 Lithium ion concentration distribution in the solid particles by equation (2.122) at $\bar{I} = 1$. The profiles are measured at $t = 0.05, 0.1, 0.15, 0.2, ...$ At certain time ($t = \hat{t}$), the concentration in the solid reaches maximum ($c_{sc} = 1$) in region near separator and at later time ($t > \hat{t}$), free boundary develops. Here $\hat{t} = 0.55$ 41
2.12 (a) Upper figure: the concentration of lithium in solid particles that reaches the maximum capacity at $x = s(t)$. The solubility rate of lithium no longer at the same rate at this point forward because of the concentration profiles of electrolyte. (b) Lower figure: The concentration profiles across the cell in comparison to the time before ($t < \hat{t}$) (by equation (2.119)) and after ($t > \hat{t}$) (by equation (2.132)) formation of free boundary. The profiles are discharged at $\bar{I} = 0.5$. The arrow shows the direction of increasing time and $\hat{t} = 0.64$. 43
2.13 The concentration of Lithium in solid particles and Lithium ions electrolyte at $\bar{I} = 1$ discharge rate. The arrow shows the direction of time increases ($t = 0.55, 0.6, 0.65, ...$) and $\hat{t} = 0.55$. 44

3.1 Structure of the electric double layer near a solid/electrolyte interface. When external electric field is applied, bulk motion of an electrolyte caused by Coulombic forces acting on ions in the electric double layer. The electric double layer, composed of a Stern layer(layer 1), Debye layer(layer 2) and bulk solution(layer 3). The bottom graph shows the difference of potential energy in each layer before the mobile ions extending into the bulk solution. 49
3.2 Diffusion coefficient as a function of concentration; line represents the fit to (3.71) and circles are the experimental data from Riemers [90]. 57
3.3 Concentration-dependent of electrolyte conductivity; line represents the fit to (3.72) and circles are the experimental data from Riemers [90]. . . . 57

4.1 Illustration of the microstructured boundary 63

5.1 Illustration of the shrinking-core model with the side by side of the two phases and the movement of the phase boundary. The processes during discharge are illustrated and the pictures below showing concentration of Lithium as a function of r for different times. The dark region represents the Lithium-rich region and the bright region represents the Lithium-poor region. 73

5.2 The lithium concentration profiles in solid particle during discharge where $\mathcal{Q} = 1$ and $\Upsilon = 20$. The vertical lines indicate the position of the phase boundary. When the surface concentration reaches 1, the reaction rate ceases hence stop the discharge. The times plotted are $t = 0.01, 0.02, 0.03, 0.04, 0.05, \cdots$. 77
5.3 The comparison of lithium concentration profiles in solid particle during discharge ($\mathcal{Q} = 1$, $\Upsilon = 20$) between the numerics and asymptotic solutions (see (5.38)-(5.39)). The solid lines represent numerics, and dash lines represent asymptotic solutions. 79
5.4 Phase boundary morphology that occurs between $FePO_4$ (black regions) and $LiFePO_4$ (grey regions) as discharge rate is increased. From left to right; (a) $\frac{I}{I_0}$=0.001, (b) $\frac{I}{I_0}$=0.01, (c) $\frac{I}{I_0}$=0.033, (d) $\frac{I}{I_0}$=0.05. Reprinted from [63]. 80

6.1 The plot of 10300-by-10300 sparse matrix of the Jacobian pattern for $n = 100$. The empty elements are the zeros. The elements 1-100 are for c, 101-200 are for ϕ, 201-300 are for ϕ_s and 301-10300 are for c_s^i. 95

7.1 The comparison of model-experimental data for the graphite half cell discharge curve at different currents. Solid lines represent the numerical results and symbols represent experimental data at various discharge currents. The dashed curve represents our fit to the equilibrium potential curve. 105
7.2 The dimensionless concentration profiles of the intercalated Lithium in the solid at different positions across the cell for the discharge rate $1C$. The profiles are measured at $t^* = 104s, 208s, 312s, 416s, 520s$. 105
7.3 (a) The concentration profile of Lithium ions in the electrolyte; (b) The potential in the electrolyte; (c) The solid concentration at the particle surface and (d) The potential in the solid at $1C$ discharge rate. $\uparrow$ is the direction of increasing time. The profiles are measured at $t^* = 104s, 208s, 312s, 416s, 520s$. 106
7.4 The comparison of analytic-numerical solution for the graphite half cell discharge curves at different currents. Solid lines represent the analytic solutions and symbols represent the numerical solution. The dashed curve represents the equilibrium potential curve. 109
7.5 Experimental data of composition-dependant diffusion coefficient by Zhang *et al.* [102] and Verbrugge *et al.* [91]. The solid lines and dots are fitting to the experimental data by Verbrugge *et al.* and Zhang *et al.* respectively. 110
7.6 The concentration of Lithium within the electrode particle with diffusion coefficients from fitting to the data from Verbrugge *et al.* [91] as shown in Figure 7.5 at $3C$ discharge rate. The profiles are measured at $t^* = 15s, 30s, 45s, 60s, 75s$. 111
7.7 Discharge curves plot with the diffusion coefficient data given by Verbrugge *et al.* (red) and Zhang *et al.* (blue) at $3C$ discharge rate. The large difference magnitude of $D_s(c_s)$ (see Figure 7.5) results in lithium depletion at the surface in a relatively short time (see Figure 7.6). 111

7.8 The comparison of non linear diffusion coefficient-experimental data for the graphite half cell discharge curves at different currents. The curves are obtained by analytic approximation solution (7.34) where the diffusion equation in the solid (see (7.23)-(7.24)) is solved numerically. The nonlinear diffusion coefficient (the fitting to the data from Zhang *et al.* [102]) is given by equation (7.36). Solid lines represent the analytic solutions and symbols represent experimental data at various discharge currents. The dashed curve represents the equilibrium potential curve. 112
7.9 The dimensionless concentration of Lithium within the electrode particle at $3C$ discharge rate where $D_s(c_s)$ is calculated using data from Zhang *et al.* [102] (see formula (7.36)). The profiles are measured at $t^* = 30s, 60s, 90s, 120s, 150s$. 113

8.1 The equilibrium potential of the $LiFePO_4$ electrode as a function of c_s (the state of discharge, $c_s = c_s^*/c_{max}$) (see equation (8.27)). 120
8.2 The comparison of model with the experimental data for the $LiFePO_4$ half cell discharge curves at different currents. Solid lines represent the analytic solutions and symbols represent experimental data at various discharge currents. 123
8.3 The concentration of solution in the electrolyte across the electrode at (a) $0.8C$ and (b) $3.2C$ discharge rate. The profiles are measured at (a) $t^* = 393s, 785s, 1178s, 1571s, 1963s$ and (b) $t^* = 162s, 325s, 487s, 585s, 650s$. . 124
8.4 The concentration of Lithium in the solid at the electrode particle surfaces as a function of position in the electrode at (a) $0.8C$ and (b) $3.2C$ discharge rate. The profiles are measured at (a) $t^* = 393s, 785s, 1178s, 1571s, 1963s$ and (b) $t^* = 162s, 325s, 487s, 585s, 650s$. 125
8.5 The reaction rate (per unit surface area) at the particle electrolyte interface as a function of position in the electrode for discharge at $3.2C$. The profiles are measured at $t^* = 162s, 325s, 487s, 585s, 650s$. 126
8.6 The dimensionless concentration in the electrode particle as a function of radius at different positions in the electrode for discharge at $3.2C$. The profiles are measured at $t^* = 162s, 325s, 487s, 585s, 650s$. 126
8.7 The concentration of solution in the electrolyte across the electrode at $8C$ discharge rate. The profiles are measured at $t^* = 33s, 48s, 58s, 62s, 65s$. . 127
8.8 The concentration of Lithium in the solid at the electrode particle surfaces as a function of position in the electrode at $8C$ discharge rate. The profiles are measured at $t^* = 33s, 48s, 58s, 62s, 65s$. 127
8.9 The voltage curves for different conductivity ratios in the solid (σ_s) and electrolyte (κ_{max}) phases. The cell is discharged at $1.6C$. 128
8.10 The dimensionless solid concentration profiles at the electrode particle surfaces as a function of position in the electrode for different conductivity ratios in the solid (σ_s) and electrolyte (κ_{max}) phases. The cell is discharged at $1.6C$. 129
8.11 The electrolyte concentration profiles across the electrode for different conductivity ratios in the solid (σ_s) and electrolyte (κ_{max}) phases. The cell is discharged at $1.6C$. 130
8.12 The dimensionless solid concentration profiles in the electrode particles as a function of radius at different positions when the cell is discharged for the 3 different cases. The cell is discharged at $1.6C$. 132

8.13 The distribution of dimensionless current density in the solid (j_s) and in the electrolyte (j) across the cathode for different conductivity ratios in the solid (σ_s) and electrolyte (κ) phases. The cell is discharged at $1.6C$. 133
8.14 The dimensionless reaction rate (G_c) across the cathode for different conductivity ratios in the solid (σ_s) and electrolyte (κ_{max}) phases. The cell is discharged at $1.6C$. 134
8.15 Distribution of the dimensionless electrolyte current density (j) across the electrode when the cell is discharged at $1.6C$ for $400s$ with different conductivity ratios in the solid (σ_s) and electrolyte (κ_{max}) phases. 135
8.16 The dimensionless reaction rate across cathode when the cell is discharged at $1.6C$ for $400s$ with different conductivity ratios in the solid (σ_s) and electrolyte (κ_{max}) phases. 136

DECLARATION OF AUTHORSHIP

I, **Rahifa Ranom**, declare that the thesis entitled **Mathematical Modelling of Lithium Ion Batteries** and the work presented in the thesis are both my own, and have been generated by me as the result of my own research. I confirm that:

- this work was done wholly or mainly while in candidature for a research degree at this University;
- any part if this thesis has previously been submitted for a degree or any other qualification at this University or any other institution, this has been clearly stated;
- where I have consulted the published work of others, this is always clearly attributed;
- where I have quoted from the work of others, the source is always given. With the exception of such quotations this thesis entirely my own work;
- I have acknowledged all main sources of help;
- where the thesis is based on work done by myself jointly with others, I have made clear exactly what was done by others and what I have contributed myself;
- parts of this work have been published.

Signed:
Date: *31st October 2014*

List of Publications

1. Ranom R., Richardson G., Please C., (2011). **Steady state solution during discharge in lithium ion batteries with Tafel kinetics**, International Conference of Chemical Engineering and Industrial Biotechnology (ICCEIB), November 28 - December 1, 2012, Pahang, Malaysia.

2. Ranom R., Richardson G., Please C.P., (2012). **Discharge of half cell cathode of lithium ion battery**. British Applied Mathematics Colloquium (BAMC), April 6 - 9, 2012, London, UK.

3. Adesokan B., Ayass W.A., Lim S., Peace A, & Rahifa R., (2013), **Assessing molecular properties for oral drug delivery.**, 5th UK Graduate Modelling Camp, April 9-12 2013, Oxford, UK.

4. Rahifa R., Foster J.M., Richardson G., (2014), **Mathematical modelling of half-cell Lithium ion battery in moderately dilute solution.**, International Meeting of Lithium Batteries, June 10-14 2014. Lake Como, Italy.

Acknowledgements

Thanks to Almighty Allah S.W.T. for graciously bestowing me the perseverance to undertake this research. Special thanks are due to: University of Southampton for the opportunity to carry out research; Universiti Teknikal Malaysia Melaka (UTeM) for the financial support and Kementerian Pengajian Tinggi (KPT). Warmest thanks and a deepest appreciation to the following people: My parents, Ranom and Hamidah, for a lifetime of love and support; My lovely husband, Ahmad Fuad, for an eternity love and full support; My academic father, Dr. Giles Richardson, for all his help and expert advice, for the encouragement and inspiration; Dr. Jamie Foster, for his numerical expertise; My daughter and son, Arissa Humaira and Isyhadh Umayr, for make my life full of happiness and laughters; My family and friends, for all their support and for sharing me so often with my problems.

To my lovely Ahmad Fuad, Arissa Humaira and Isyhadh Umayr

To my dearest parents, Ranom and Kamidah . . .

Chapter 1

Introduction

The demand for more efficient renewable energy resources is rapidly growing as energy and environmental based issues becomes of increasing concern. Lithium ion batteries are currently the state of art of rechargeable electrochemical storage devices. These batteries provide high volumetric energy densities, high cyclability and are highly flexible as regards to design, size and application. They are used in many applications in portable electronics such as mobile phones, laptops and power tools; and are being considered for use in electric vehicles. Lithium ion batteries have thus gained much attention from researchers worldwide. Moreover, the development of lithium batteries has become a key focus for researchers in automotive companies who are investigating their use in hybrid electric vehicles (HEV), plugin hybrid vehicles (PHEV), and purely electric vehicles (EV); the markets for all of which are expected to grow substantially in the future years.

1.1 Lithium batteries as energy storage solution

The lithium ion battery is one of the most successful electrochemical batteries and billion of these cells are produced every year. They provide rechargeable energy storage at high energy density, with no memory effect, and slow loss of charge when not in use [11]. They are of growing interest to the automotive industry, amongst others. Thus, there is a big drive to increase their efficiency, storage performance and the speed at which they can be charged and recharged. Many approaches have been taken to simulate the operation of such devices in order to better understand their behaviour.

The Lithium ion cell consists of four parts, namely (I) the anode which is comprised of negative electrode particles, (II) the cathode which is comprised of positive electrode particles, (III) the separator that lies between the electrodes (this is a porous insulator that prevents direct electrical contact between the electrodes while allowing passage of

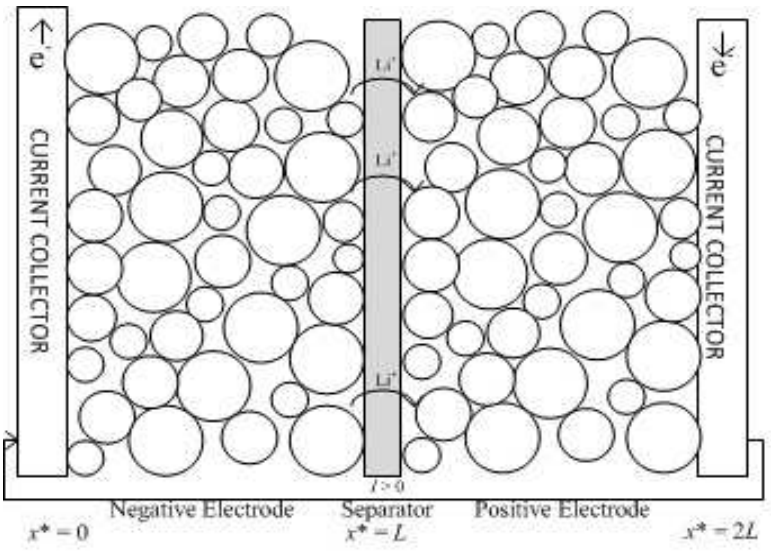

Figure 1.1: A schematic diagram of the Lithium Ion Battery during discharge [59]. The current flowing out of the positive electrode drives the extraction of lithium ion from negative electrode (anode) particles to the electrolyte across the porous separator (by diffusion and advection) into the positive electrode (cathode) and insert into the positive electrode (cathode). The charge of electrons are moving from the negative electrode particles to the negative electrode current collector and from the positive electrode current collector to the positive electrode particles.

the electrolyte) and (IV) the Lithium ion electrolyte which transports ions (and thus charge) between the anode and cathode. A schematic diagram of such a cell (during discharge) is shown in Figure 1.1. At the outer boundaries of electrodes there are current collectors (charge collectors) that connect to an external circuit.

During discharge, Lithium diffuses through the negative electrode (anode) particles to the solid-electrolyte interface where it undergoes a charge transfer reaction (refer Figure 1.1) in which a Lithium ion (Li^+) is released into the electrolyte and an electron (e^-) is released into the electrode particle (de-intercalation). The Lithium ion advects, and diffuses, through the electrolyte solution to the positive electrode (cathode). A similar reaction occurs on the surface of a positive electrode (cathode) particle in which the Lithium ion is absorbed into the electrode particle (by a process known as intercalation) and takes up an electron from the electrode as it does so. The negative ions (N^-), on the other hand, remain in the electrolyte throughout. Thus the Lithium ions (Li^+) carry all the charge through the electrolyte (and separator diaphragm) from the anode to cathode. Typically, the reaction rate on an electrode particle surface depends upon the lithium concentration on the electrode surface, the lithium ion concentration in the adjacent electrolyte, and the potential drop between the electrode and electrolyte [36]. When the cell is charging, the process is reversed: an external electrical power source (the charging circuit) applies a higher voltage than that produced by the battery, forcing

current to pass in the reverse direction. The Lithium ions then migrate from the cathode to the anode, where they become embedded in the electrode material (intercalation).

The anode and cathode materials are selected so that the anode preferentially gives up electrons (and thus also lithium ions), and the cathode preferentially accepts electrons (and thus lithium ions). The tendency of a material to give up or accept electrons is determined by its standard electrode potential. The difference in the standard electrode potential of the anode and the cathode gives the voltage of the cell at equilibrium (the potential difference between the current collectors). The equilibrium potential is the difference between the electrical potential of the two current collectors when no external electric current flows between them. It is a function of the electrode materials used. In the following sections, an overview of battery materials for Lithium ion rechargeable batteries is provided.

1.2 Battery materials for Lithium ion batteries

Typically, both electrodes (anode and cathode) in a lithium ion battery are intercalation compounds, that is, they have a lattice structure in which small atoms, such as lithium, can be inserted and extracted. In contrast, the electrolyte allows the flow of electrical charge (in the form of lithium ions) between the anode and cathode. This section reviews battery materials for anodes, cathodes and electrolytes.

1.2.1 Desirable electrode and electrolyte properties

In designing a battery, the properties of electrode materials and electrolytes are important in order to achieve a successful cell once they are assembled. They should, for example be chosen so that the cell is stable and safe to minimizes the risk of short circuits. The key requirements for a successful electrolyte are high conductivity (high mobility of Lithium ions), stability (at high temperatures and in high voltage application) [82], and safety (low flammability [10]). Electrolyte decomposition and side reactions in lithium ion batteries can create thermal runaway [11]. Thus, the electrolyte selection has to balance between flammability and electrochemical performance.

Good electrode materials should have high lithium diffusivity in the host matrix; high electrical conductivity; stability (not change structure over many charge cycles); high capacity [95]; thermal stability [10], high cyclability and be non toxic and low cost [11]. The two electrode materials also be chosen to give the cell a high voltage. The solid electrolyte interface (SEI layer) is another key factor that influences the performance of battery. The roles of this layer is to eliminate the transfer of negative ions from the electrolyte to the electrodes and to limit the transfer of electrons from the electrodes to the electrolytes [48]. However, the SEI layer must also be a good Lithium ion conductor.

1.2.2 The cathode material

In 1991, the first type of cathode material to go into commercial production, was cobalt oxide ($LiCoO_2$) [95]. It (de)intercalates lithium ions at around $4V$ and has a theoretical capacity of 140 mAh/g [88]. The other advanced cathode materials include lithium metal oxides (such as $LiMn_2O_4$), olivines (such as $LiFePO_4$), and rechargeable lithium oxides [82].

In 1996, Goodenough patented a new kind of lithium ion cathode material which is iron phosphate $LiFePO_4$ [65]. This material is more powerful and less likely to catching fire, which are important considerations for automotive applications. $LiFePO_4$ has already found in many industrial applications due to its reasonable voltage of $3.5V$, high theoretical capacity ($170mAh/g$) [52], low cost, low toxicity, and high thermal stability [65]. Because of its potential, much research has been directed towards optimizing synthesis routes for $LiFePO_4$ cathodes. A disadvantage of this material is low conductivity. However carbon coating of the electrode particles increases the conductivity of the electrode [47]. $LiFePO_4$ is also thermodynamically stable [67], and its has a lattice structure so that the insertion/extraction lithium ions process does not change structure of the host material [95].

Lithium metal oxides contain cobalt and nickel. They show a high stability in the high-voltage range but cobalt has limited availability in natural resources and is toxic [22]. Manganese offers very good rate capabilities but has poor cycling behaviour. Therefore, mixtures of these three materials are often used for a good cathode material.

1.2.3 The anode material

The commercial anode material in lithium ion batteries is graphitic carbon (LiC_6) which can store up to one Li^+ for every six carbon atoms in between its graphene layers. The material is highly conducting and supports high current densities [13]. However, the theoretical capacity (372 mAh/g) is poor in comparison to that of pure lithium (3,862 mAh/g) [97] and it exhibits moderate charge/discharge rate performance which limits the lifetime of the cell [69]. The parameters used to increase the performance of this anode material are its thickness, and its porosity.

Alloy anodes such as Li-Al (Lithium Aluminium) have high capacities but exhibits substantial volume changes, which results in low cyclability [22]. Reducing the size of this electrode particles to the order of a few nanometres stops phase transitions occurring that typically accompany alloy formation [10] and reduces the size of the volume changes. Lithium titanate operates at a $2.4V$, a voltage for which lithium ions are stable with respect to the electrolyte [11] (which is a requirement in this material because it does not form an SEI layer). A disadvantage of the lithium titanate battery is lower capacity and voltage than the conventional anode material. Silicon has an extremely high

capacity (4,199 mAh/g) corresponding to a composition of Si_5Li_{22} [22]. However, the large volume changes that occur during the insertion and extraction processes cause severe cracking of the electrode, which in turn leads to very significant capacity fade during cycling [98]. The cyclability of this electrode can be improved by adding Ketjen-black carbon, which gives a chainlike structure that maintains a stable electronic contact between silicon particles [98]. They can also be improved by nanostructuring [10].

1.2.4 The electrolyte

Liquid electrolytes conduct lithium ions and acting as a carrier between the cathode and the anode. The electrolytes typically used in lithium ion cells are mainly based on an organic solvent based. Examples of electrolyte salts used in applications include lithium hexafluorophosphate ($LiPF_6$), lithium hexafluoroarsenate monohydrate ($LiAsF_6$), lithium perchlorate ($LiClO_4$), lithium tetrafluoroborate ($LiBF_4$), and lithium triflate ($LiCF_3SO_3$). $LiClO_4$ provides a stable charge-discharge efficiency that increases the cycling capacity of the cell [10]. $LiBF_4$ is less toxic than $LiAsF_6$ and safer than $LiClO_4$ but has only moderate ionic conductivity [47]. $LiCF_3SO_3$ is resistant to oxidation, nontoxic, thermally stable, and insensitive to ambient temperature in contrast to $LiPF_6$. However, it has low conductivity in nonaqueous solvents as compared to other salts [47].

Currently, $LiPF_6$ is the standard electrolyte in commercial batteries. It has qualities such as high conductivity, high solubility in organic solvents, and stability in the solvents mixture and on common electrode materials [22]. The organic solvent that often used in battery electrolyte is a mixture of ethylene carbonate and dimethyl carbonate (1:1 EC:DMC). Ethylene carbonate (EC) has ability to form a good SEI layer on common anode materials and dimethyl carbonate (DMC) has ability to lower the EC melting point [22]. In this study, we chose the most common electrolyte solution, which is $LiPF_6$ salts dissolved in a mixture of 1:1 EC:DMC. This combination performs well enough in current battery systems.

1.3 Charge-transfer reaction

The reactions in which charges are transferred across a solid electrolyte interface are called charge transfer reactions. Here both electrodes are either oxidized or reduced;

$$Li_{(s)} \rightleftharpoons Li^+ + e^-.$$

Charge separation occurs when charge transfers across the electrode surface. The excess charge on the electrode surface is counterbalanced by the accumulation of oppositely

charged ions, on the electrolyte phase. The layer across which this charge separation occurs is called the electrical double layer, and is extremely thin (typically of order 1nm) compared with the width of the electrolyte and electrodes. In its simplest form the double layer is described by the Helmholtz model, which describes the double layer as a parallel plate capacitor with a small plate separation (see Figure 1.2). In this model, the potential changes linearly from the electrode potential ϕ_s to the electrolyte potential ϕ in a thin layer. This layer is referred to as the Helmholtz layer.

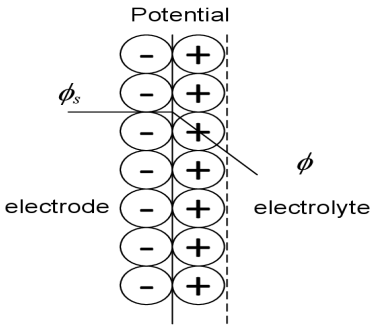

Figure 1.2: Structure of the electric double layer near a solid electrolyte interface when external electric field is applied. The electric drops linearly from the electrode potential ϕ_s to the electrolyte potential ϕ in a thin layer.

The electrical double layer translates into boundary layers in the concentration profiles. Near an electrode that is negatively charged we expect an excess of Li^+ ions and a deficit of N^- ions. These differences are only expected close to the electrode surface, thus it is usual to assume charge neutrality in the bulk of the solution. Further details on charge neutrality will be discussed later. The overpotential, $q\eta$ is defined such that η gives the change in the electrochemical potential of a Li^+ between the electrolyte and the electrode. It takes the form

$$\eta = \phi - \phi_s + U_{eq}$$

where ϕ is the electrolyte potential, ϕ_s is the solid potential and U_{eq} is the equilibrium potential of the electrode material (qU_{eq} is the change in chemical potential of Li^+ ion between the electrode and electrolyte). The equilibrium potential, or open circuit potential, is the difference of electrical potential between the two terminals of a device when there is no electric current flows between them. Usually it is measured at a very low discharge rate.

1.4 Battery Terminology

- **Capacity.** The capacity is a measurement of how many electrons can be extracted from an electrode during each charge or discharge cycle and has unit in

milliamp hours per gram. A symbol Q is used for this parameter. This quantity is often normalized by mass, so that it is unaffected by the size of the battery. The maximum capacity of a cell is determined by the amount of charge when the cell is discharged at a very low rate. Current cathode materials have maximum capacities in the range of $Q_{max} = 100 - 200mAh/g$ and graphitic carbon (the most common anode material) which has a maximum capacity of around $Q_{max} = 300mAh/g$.

- **Specific Power.** Another important parameter for battery operation is how much power can be provided per unit mass. This value, measured in watts per kilogram, is particularly important for high power applications such as acceleration of electric vehicles where a large amount of energy must be provided in a short time. Specific power is heavily influenced by the voltage difference between the anode and cathode and the speed of ion transfer between the electrodes.

- **Cell Voltage.** A key parameter in maximizing the specific power of a battery is the voltage difference between the anode and cathode. This difference is determined by the relative voltages at which the (de)intercalation reactions take place. In this thesis, discharge curves are plotted showing the cell voltage as a function of the state of discharge and at certain specific discharge rates.

- **Discharge rate, C-rate.** The discharge rate is the rate at which current is taken from a cell. It is reported as a C-rate with $1C$ corresponding to a battery being completely charged or discharged in one hour. High rate capability is essential for quick charging batteries and high power applications. For instance, for a battery with a capacity of $100A/hours$, this equates to a discharge current of $100Amps$. A $5C$ rate for this battery would be $500Amps$, and a $C/2$ rate would be $50Amps$.

- **State of charge / discharge.** The state of charge (SOC) is defined as the capacity still available in the cell. It is normally expressed as a ratio of the rated capacity to the maximum capacity and a 0 SOC battery is fully discharged while a 1 SOC battery is fully charged battery. The state of discharge (SOD) is defined as the ratio of battery capacity that has been discharged to the maximum capacity. State of charge/discharge can be calculated as the current multiplied by the time and divided by the maximum capacity of the cell (It/Q_{max}).

1.5 The half-cell

In order to test a particular electrode in the lab it is usual to perform experiments on a half-cell. This consists of a single electrode (working electrode either anode or cathode) and a pure Lithium electrode (reference electrode) as the other electrode (see Figures 1.3 and 1.4). Since the electrochemical potential of lithium in a lithium electrode does not change as it charges / discharges, it also acts as a reference electrode. Indeed in

applications it is usual to define potential with respect to a lithium electrode such that its potential is defined to be zero. The voltage drop across the half cell is then determined by the potential of the current collector. This motivated Newman to formulate his models [60] in terms of a lithium reference potential rather than the real potential. Theoretical treatment of half-cells include works by Newman et. al. [84] and Farrell et.al. [23]. Fundamental research on electrode material is usually conducted in half-cell systems. Figure 1.3 shows a schematic diagram of a half-cell anode and Figure 1.4 that for a half-cell cathode.

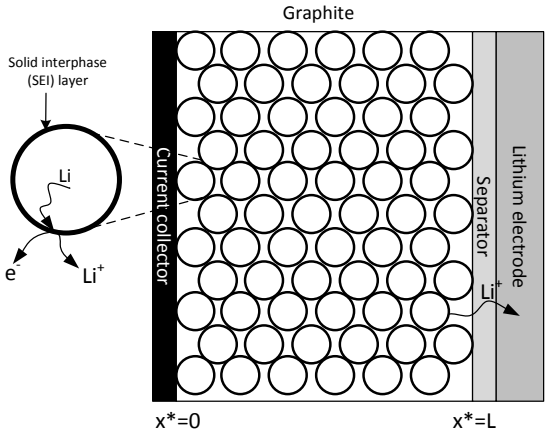

Figure 1.3: Schematic diagram for typical half cell anode. The cathode material is a lithium-foil which is reacting as reference electrode. During discharge, the Lithium ions are conducted through the electrolyte solution to the lithium electrode. Here $x^* = 0$ is the anode current collector and $x^* = L$ is the separator.

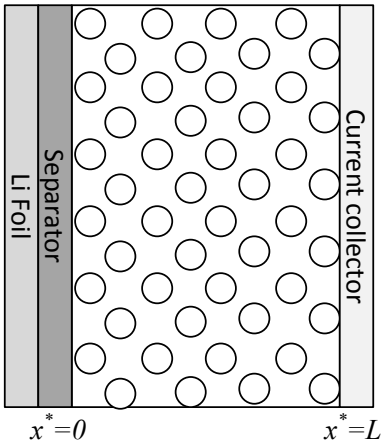

Figure 1.4: A schematic diagram for a typical half-cell cathode. The anode material is a lithium-foil. Here $x^* = 0$ is the separator and $x^* = L$ is at cathode current collector

1.6 Battery modelling

Electrochemical battery models are based on the numerous chemical processes that take place in the battery. In particular they must account for conservation of ion species in the electrolyte, charge transfer at electrolyte/electrode interfaces [19] and transport of intercalated Lithium in the electrodes. These processes take place over a wide range of scales ranging from that of the electrode particles (microscopic) to that of the full cell (macroscopic). Thus, modelling capable of directly relating the geometry of the microstructure to the coefficients in a macroscopic model of battery behaviour provides a useful tool. Microscopic modelling on the particle lengthscale should account for charge transfer at the solid particle surface, diffusion of lithium in the electrode particles and diffusion of lithium and charge transport in the electrolyte around the particles. These microscopic and interfacial phenomena largely control the rate of electrochemical reactions. Macroscopic models on the electrode lengthscale can be used to account for charge transport, electrolyte lithium transport and charge transfer reactions all in an averaged sense.

The typical voltage and charge capacity of lithium-ion cells can be computed using classical electrochemistry or measured with simple experiments. However, understanding the dynamic processes that occur during charge and discharge of the battery is necessary in order to improve the power density and cycle life of the battery. Study of the charge/discharge processes is made more difficult by the range of length scales involved [21]. The charge carriers inside the battery move via a combination of diffusion and advection in an electric field. Their movement causes potential differences [64]. The reaction rate for the deintercalation/intercalation of lithium from the electrodes may be limited by diffusion of Lithium ions in the electrolyte, diffusion of Lithium in the electrode particles or by the electrical resistivity of the electrolyte or electrodes [36, 74]. Thus, it is important to investigate the relative importance of these processes.

John Newman, a chemical engineer at the University of California at Berkeley, has developed a modelling framework for lithium ion batteries [58]. In [57] Newman and his co-worker use this framework to predict battery behaviour. The modelling approach is based on transport equations for Lithium ions in the electrolyte as well as Lithium transport in the electrode particles of the cathode and the anode, and Butler-Volmer equations describing the charge-transfer kinetics at the electrode particle surfaces (between electrode and electrolyte). Solutions of such models can be used to predict cell voltage as a function of current and time. In addition they can be used to predict the potentials in the electrolyte and electrode phases, salt concentration, reaction rates and current density in the electrolyte as functions of time and position.

A model based on loss of the active lithium ions due to the electrochemical parasitic reaction and rise of the anode film resistance has been developed by Gang Ning *et al.* [61]. Loss of cyclable lithium ions occurs when irreversible solvent reduction reaction

takes place on the surface anode and hence increased the resistances on the surface of anode particle. Safari *et al.* [77] simulated the ageing phenomena in a commercial graphite/$LiFePO_4$ cell.

The effects of interionic drag in non-dilute solution has been incorporated into Newman framework [60] but requires the model to be calibrated again experimental electrolyte data. An example of such data is found in the work of Riemers et. al [90] which measures conductivity, diffusivity and transference number as function of ions concentration in the electrolyte $LiPF_6$ in 1:1 EC:DMC. Fuller, Doyle and Newman [28, 36] incorporated the effects of the chemical activity in the electrolyte into their modelling framework.

Recent work has shown that performance of Lithium ion battery can be improved through emphasis on engineering the microstructural architecture of the electrodes see [41, 83, 39]. Typically the effects of the microstructure in macroscopic models, such as Newman's [58], are represented by a few phenomenological parameters which can be crudely related to the properties of the microstructure. A more systematic approach, that is capable of relating the geometry of the microstructure coefficients in the macroscopic model, has been developed by Richardson et.al [74] in the case of dilute electrolytes. Here we shall extend this method to a moderately concentrated electrolyte.

Solutions to a battery model based on a dilute electrolyte model in which Lithium diffusion in the electrode particles is extremely fast are discussed in Chapter 2. In Chapter 3 we discuss an electrolyte model of a moderately concentrated electrolyte and fit the model to real electrolyte diffusion, conductivity and transference number data. In Chapter 4, we discuss the application of homogenisation techniques to a model based on the moderately concentrated electrolyte model discussed in Chapter 3. In Chapter 5, we discuss Lithium transport in electrode particles (in particular the $LiFePO_4$ and the LiC_6 electrode materials), this is crucial for understanding intercalation. In Chapter 6, we discuss the numerical method that we use to solve the homogenised model presented in Chapter 4. Solutions to the model are compared against experimental data for half-cell Li_xC_6 (graphite) anodes (Chapter 7) and half-cell $LiFePO_4$ cathodes (Chapter 8). Finally, we draw our conclusions in Chapter 9.

1.6.1 Statement of originality

Here, we highlight the original parts in this study. In Chapter 2 we obtain new solutions of battery model in dilute electrolyte theory. In Chapter 3, we review the existing moderately concentrated electrolyte model (originally formulated in [59]) and highlights some errors and give corrections. In Chapter 4, we extend the results of the homogenisation in [74] to a battery model in moderately concentrated electrolyte. The numerical procedure developed in Chapter 6 to solve battery problems is new and is very efficient. The results in Chapter 7 follow the work of Srinivasan and Newman [85] for a half

cell anode but are significantly extended and provide considerably better agreement to experimental data. The results for the half cell cathode in Chapter 8 are all new.

Chapter 2

Dilute electrolyte modelling of battery

2.1 Introduction

In this section we develop a battery model based on dilute electrolyte theory. We start in §2.2, by discussing a model for a dilute electrolyte. We then discuss lithium transport between the electrolyte and the electrode particles in §2.3 before briefly discussing transport in the electrode particles in §2.4 and illustrating how homogenisation can be used to derive a model on the scale of the battery model in §2.5. In §2.6 and §2.7 we derive some solutions to this battery scale model that illustrate the behaviour of a certain class of cell.

2.2 Derivation of a model for a dilute electrolyte

The Nernst-Planck theory has been used to describe a sufficiently dilute electrolyte [60]. This theory describes conservation equations for the ionic species that diffuse by ionic concentration gradient and advect by an electric field. Here we discuss the derivation of battery model in a dilute electrolyte, which previously has been described in Richardson *et al.* [74].

The general conservation of mass equation for two species, concentrations c_n^* and c_p^* (mol m^{-3}), that diffuse independently are

$$\frac{\partial c_i^*}{\partial t^*} + \nabla \cdot \boldsymbol{q}_i^* = 0 \qquad \boldsymbol{q}_i^* = -D_i \nabla c_i^* \qquad \text{for } i = n, p. \tag{2.1}$$

where $\boldsymbol{q}_i^*$ is the ion flux of species i. The second equation is Fick's Law of diffusion which states that the diffusive flux is proportional to the concentration gradient. Here D_n and

D_p are the diffusion coefficient of species n and p. To extend Fick's Law of diffusion to charged species (ions) we need to include electric forces arising from the electric field, $\boldsymbol{E} = -\nabla\phi^*$ where ϕ^* is the electric potential. Consider an ion of charge q, it experiences a force, $\boldsymbol{F} = q\mathbf{E}$. As the ion moves through the solvent, it also experiences a frictional drag force, $\boldsymbol{F} = \kappa\boldsymbol{\upsilon}$. Here the drag coefficient κ is related to the mobility, μ of the ion by $\kappa = 1/\mu$. The drift velocity is reached when both forces balance, i.e for $q\boldsymbol{E} = \boldsymbol{\upsilon}/\mu$. This gives the drift velocity, $\boldsymbol{\upsilon} = q\boldsymbol{E}\ \mu$. Thus, the advection-diffusion equation for a negatively charged ion species with charge $-q_n$ and a positively charged ion species with charge $+q_p$ is

$$\frac{\partial c_n^*}{\partial t^*} + \nabla \cdot \boldsymbol{q}_n^* = 0 \qquad \boldsymbol{q}_n^* = -(D_n \nabla c_n^* - q_n \mu_n c_n^* \nabla \phi^*), \quad \text{for anions} \tag{2.2}$$

$$\frac{\partial c_p^*}{\partial t^*} + \nabla \cdot \boldsymbol{q}_p^* = 0 \qquad \boldsymbol{q}_p^* = -(D_p \nabla c_p^* + q_p \mu_p c_p^* \nabla \phi^*), \quad \text{for cations} \tag{2.3}$$

The Einstein relation relates mobility to the diffusion coefficient D_i via $\mu_i = D_i/kT$ where k is Boltzmann's constant and T is the absolute temperature.

The electric potential obeys Poisson's equation

$$\nabla \cdot (\varepsilon \nabla \phi^*) = -\rho, \tag{2.4}$$

where ρ is the charge density (C m^{-3}). Equation (2.4) can be rewritten in terms of the ion concentration

$$\nabla \cdot (\varepsilon \nabla \phi^*) = F(c_n^* - c_p^*) \tag{2.5}$$

where ε is the permittivity of the electrolyte and F is Faraday's constant (C mol^{-1}). It is also useful to write the current density in terms of ion fluxes, $\boldsymbol{q}_p^*$ and $\boldsymbol{q}_n^*$

$$\mathbf{j}^* = F(\mathbf{q}_p^* - \mathbf{q}_n^*) \tag{2.6}$$

2.2.1 Charge neutrality

Here we consider a 1:1 electrolyte in which the charge of the negative ions is $-q_n = -q$ and of the positive ions ions is $q_p = +q$ and q is the charge on a proton. For all reasonable concentrations the Debye length is very small (of the order of nanometres) so that the standard charge neutrality assumption $c_p^* \approx c_n^*$ is appropriate [73]. Writing $c_n^* = c_p^* = c^*$ in (2.2)-(2.3) allows us to rewrite the model in the form

$$\frac{\partial c^*}{\partial t^*} = \nabla \cdot (D_n \nabla c^* - \frac{D_n F}{RT} c^* \nabla \phi^*), \tag{2.7}$$

$$\frac{\partial c^*}{\partial t^*} = \nabla \cdot (D_p \nabla c^* + \frac{D_p F}{RT} q c^* \nabla \phi^*), \tag{2.8}$$

Here we use the fact that $q/k = F/R$ where F is Faraday's constant and R is the universal gas constant. Now we can manipulate (2.7)-(2.8) by multiplying (2.8) by D_n and (2.7) by D_p, respectively and adding the resulting equations to obtain a diffusion equation for the electrolyte concentration c

$$\frac{\partial c^*}{\partial t^*} = \nabla \cdot \left(\left(\frac{2D_n D_p}{D_n + D_p} \right) \nabla c^* \right) \tag{2.9}$$

Subtracting (2.7) from (2.8) leads to an equation for the current density as defined in (2.6)

$$\nabla \cdot \boldsymbol{j}^* = 0 \tag{2.10}$$

$$\boldsymbol{j}^* = -(D_n + D_p) \left[\frac{F}{RT} c^* \nabla \phi^* - \frac{D_n - D_p}{D_n + D_p} \nabla c^* \right] \tag{2.11}$$

We emphasize that the resulting conservation equation (2.9) only works for constant diffusion coefficients. However, this is not an accurate behaviour of electrolyte and non-linear diffusion coefficient has to be taken into account. The non-linear diffusion coefficients can be adapted into the model using more complicated multicomponent diffusion equations [8]. These are discussed in Chapter 3 (for a moderately concentrated electrolyte model).

2.3 Reaction kinetics on the electrode particle surfaces

Here we consider the intercalation reaction that takes place on the surface of the electrode particles and which is responsible for transport of lithium out of the electrode particles into the electrolyte and vice versa.

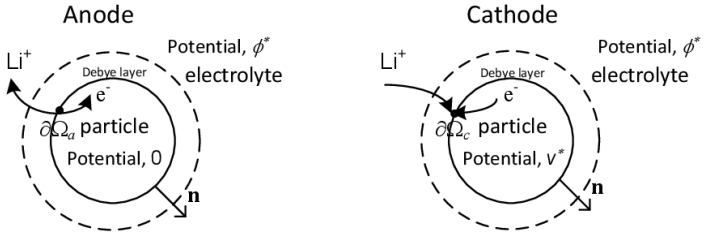

Figure 2.1: Reaction rate on the solid electrolyte interface in anode and cathode.

On the particle electrolyte interface (Figure 2.1), conservation of lithium ions and negative ions are described by the relations

$$\mathbf{n} \cdot \mathbf{q}_p^* = G_a^*, \qquad \mathbf{n} \cdot \mathbf{q}_n^* = 0 \qquad \text{on } \partial\Omega_a \tag{2.12}$$

$$\mathbf{n} \cdot \mathbf{q}_p^* = G_c^*, \qquad \mathbf{n} \cdot \mathbf{q}_n^* = 0 \qquad \text{on } \partial\Omega_c \tag{2.13}$$

where G_a^* and G_c^* are surface reaction rates giving the flux of lithium ions out of the anode and cathode electrode particles respectively. The surface reaction rates depend typically upon the intercalated lithium concentration on the electrode surface, and the concentration of ions in the electrolyte at the surface. They are usually modelled by the phenomenological Butler-Volmer equation. Here we shall assume that individual particles are electronically well-connected to the current collector and effectively neglect resistance within the electrodes. Without loss of generality we take the potential of the negative electrode (anode) particles to be 0. The overpotential in the anode (the change in electrochemical potential that a charged species goes through as it passes through an anode particle surface into the electrolyte) is $\phi^* + U_{eqa}^*$ [55]. The Butler Volmer relation for the surface reaction rate depends on the overpotential in the following manner

$$G_a^* = \frac{i_{0a}}{F}\left(\exp\left[\frac{-F}{2RT}(\phi^* + U_{eqa}^*(c_s^*))\right] - \exp\left[\frac{F}{2RT}(\phi^* + U_{eqa}^*(c_s^*))\right]\right) \quad \text{in } 0 < x^* < L \tag{2.14}$$

Here i_{0a} is the exchange current density in anode. In the cathode (positive electrode) we denote the potential V^* so that the overpotential is $\phi^* - V^* + U_{eqc}^*$ and the Butler Volmer relation takes the form

$$G_c^* = \frac{i_{0c}}{F}\left(\exp\left[\frac{-F}{2RT}(\phi^* - V^* + U_{eqc}^*(c_s^*))\right] - \exp\left[\frac{F}{2RT}(\phi^* - V^* + U_{eqc}^*(c_s^*))\right]\right) \quad \text{in } L < x^* < 2L \tag{2.15}$$

where i_{0c} is the exchange current density in cathode. Here $U_{eqa}^*(c_s^*)$ and $U_{eqc}^*(c_s^*)$ are the anodic and cathodic equilibrium potentials respectively and vary with the intercalated lithium concentrations c_s^* on the surface of the electrode particles. The open circuit potentials can vary widely depending on the insertion chemistry of the material. The work [36] gives analytic expression for $U_{eqc}^*(y)$ that fits to the experimental data for $Li_yMn_2O_4$ where y is the amount of lithium inserted. This expression shows a small step decrease of potential around the middle of the discharge (see Figure 2.2(b)). In the case of Li_yFePO_4, the discharge curve shows hardly any variation until the cell is entirely discharged [84] (see Figure 2.2(c)). Moreover, the open circuit potential of cobalt dioxide, Li_yCoO_2 varies with changes in y [37] (see Figure 2.2(a))). The open-circuit potential curves for different cathode materials and anode materials are shown in Figures 2.2 and 2.3. The analytic expression for $U_{eqa}^*(x)$ of Li_xC_6 which has been given in [36] shows significant variation with changes in x (refer Figure 2.3(a)). Lithium titanate ($Li_xTi_5O_{12}$) has a flat

discharge curve [80] (see Figure 2.3(c)) whereas silica (Li_xSi_5) is more like Li_xC_6 in that its discharge curve varies significantly with changes in composition x (see Figure 2.3(b)).

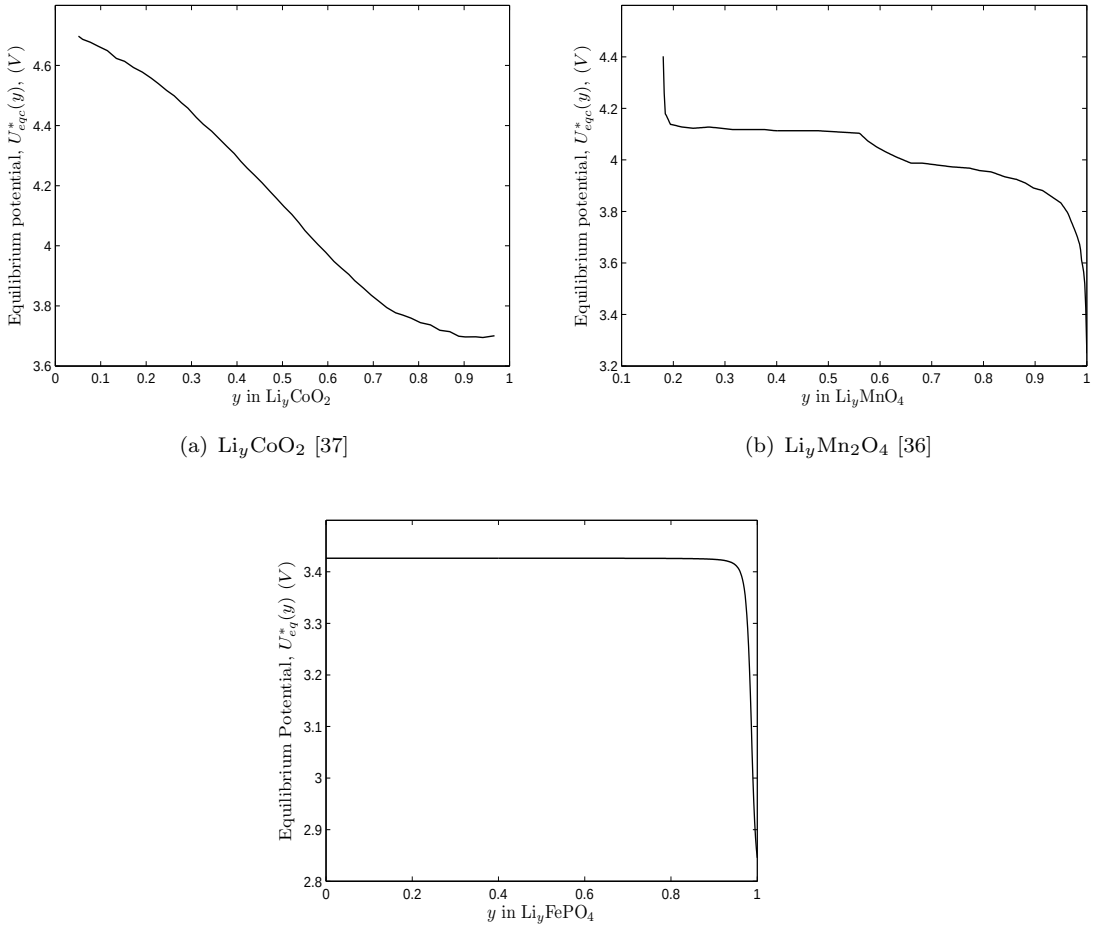

(a) Li_yCoO_2 [37]

(b) $Li_yMn_2O_4$ [36]

(c) Li_yFePO_4 [84]

Figure 2.2: Different types of open circuit potential i.e. $U^*_{eqc}(y)$ curves for different cathode materials with respect to the insertion chemistry of the materials, y (normalized capacity).

2.4 The electrode particles

In the anode particles (as the cell is discharged), lithium diffuses to the electrolyte-solid interface where the chemical reaction occurs, transferring lithium ions to the solution and electrons to the collector [14]. The lithium ions thus produced, flow through the electrolyte solution to the positive electrode, where, at the interface of the solid material, they react and insert into the metal oxide solid particles.

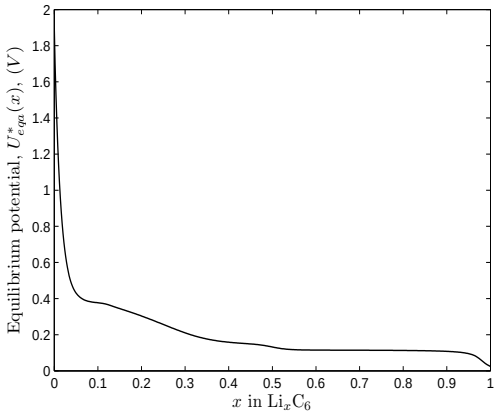

(a) Li_xC_6 [36]

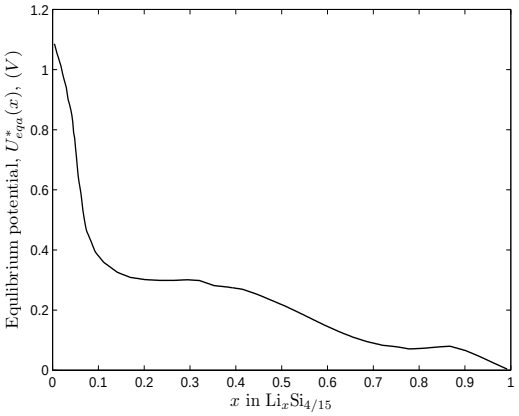

(b) Li_xSi_5 [16]

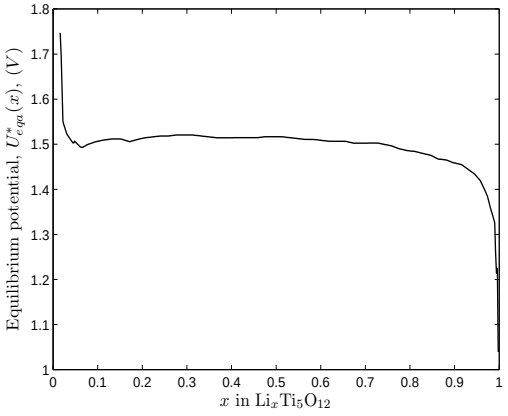

(c) $Li_xTi_5O_{12}$ [80]

Figure 2.3: Different types of open circuit potential i.e $U^*_{eqa}(x)$ curves for different anode materials with respect to the insertion chemistry of the materials, x (normalized capacity).

This process is enabled by diffusion of Lithium into (and out of) the electrode particle. At the surface of the particles, lithium ions are released into the electrolyte by the surface electrode reaction. In [28], diffusion of lithium in the solid phase is described by the diffusion equation in spherical coordinates;

$$\frac{\partial c_s^*}{\partial t^*} = D_s \frac{\partial c_s^*}{\partial r^*}, \qquad 0 \leq r^* \leq R_0 \tag{2.16}$$

$$\left.\frac{\partial c_s^*}{\partial r^*}\right|_{r^*=0} = 0, \qquad \left. D_s \frac{\partial c_s^*}{\partial r^*}\right|_{r^*=R_0} = -G^* \tag{2.17}$$

where c_s^* is the concentration in the electrode particle, D_s is the lithium diffusion in the electrode particle, R_0 is the radius and G^* is the surface reaction rate (per unit area). Here, we follow [74] in which it is assumed that the electrode particles are sufficiently small so that diffusion of intercalated lithium within the particle is much faster than

that of ions in the electrolyte across the battery. Thus, the Lithium concentration in the solid particles can be approximated as a function of time only. The material balance for the lithium ions in anode and cathode particles on radius R_a and R_c, respectively are thus governed by

$$\frac{\partial}{\partial t^*}\left(\frac{4}{3}\pi R_a^3 c_{sa}^*\right) = -4\pi R_a^2 G_a^*, \qquad \frac{\partial}{\partial t^*}\left(\frac{4}{3}\pi R_c^3 c_{sc}^*\right) = -4\pi R_c^2 G_c^*. \tag{2.18}$$

These equations describe conservation of lithium within a particle accounting for the total rate of lithium intercalation on its surface.

2.5 Homogenisation of model accounting for microstructure on electrode particle scale

We now set out to write down a model for a battery based on the dilute electrode solution theory discussed in §2.2 and on the typical battery structures discussed in Chapter 1 (see Figure 1.1 for an illustration). At the battery-scale, the number of variables governing performance increases enormously and can only be analyzed at a reasonable cost in an appropriate mathematical framework. Recent work has shown that the performance of lithium ion technology can be improved through emphasis on engineering the microstructural architecture of the electrodes see [41, 23]. Here we follow Richardson *et al.* [74] and incorporate the microscale effects into the macro-scale problem through homogenization.

Newman had written down macroscopic battery equations based on phenomenological grounds [58] which have been used subsequently in a number of applications [28, 36, 23, 29]. In [74], however, the equations are derived systematically using homogenisation techniques. The macroscopic model is characterized by the Lithium-ion concentration in the liquid phase, c^*, and the electric potential of the liquid phase, ϕ^* and the Lithium concentration in the solid electrode particles. The intercalation of Lithium-ions from the electrolyte into the particles is represented by a surface reaction rate on the surface of the particles, G^* which gives the flux of lithium ions from the electrode particle into the electrolyte per unit area of the interface.

At the micro-scale, a single representative electrode particle is examined. The micro-scale variables include the microscopic lithium concentration in the anodic and cathodic particles, c_{sa}^* and c_{sc}^*, respectively. The rate of diffusion into the particle and subsequently into the particle depend on the microscopic lithium transfer rate, G^*.

The geometry of the problem is illustrated in Figure 1.1. Here $0 < x^* < L$ is a region occupied by the negative electrode electrode particles, there is then a thin separator on the other side of which the positive electrode occupies the region $L < x^* < 2L$. The

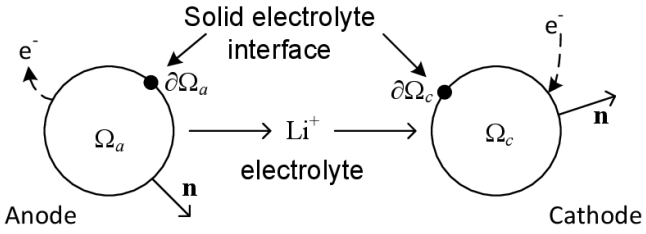

Figure 2.4: Schematic representation of the mathematical domains in particle scale.

particles are bathed in the electrolyte which can freely permeate the porous spacer. Here we denote the region occupied by the anode particles by Ω_a and the cathode particles by Ω_c (as illustrated in Figure 2.4). $\partial\Omega_a$ is the anode solid electrolyte interface and $\partial\Omega_c$ is the cathode solid electrolyte interface. We denote the unit normal vector to the interface $\partial\Omega_a$ and $\partial\Omega_c$ by $\boldsymbol{n}$; this is directed.

The homogenised equations for the diffusion of lithium ions in the electrolyte and for the potential in the electrolyte are derived in [74] from (2.9)-(2.11) accounting for the lithium flux G^* on the surface of the electrode particles. The resulting equations are

$$\epsilon_v \frac{\partial c^*}{\partial t^*} - \frac{\partial}{\partial x^*}\left(D_{eff}\frac{\partial c^*}{\partial x^*}\right) = (1-t_+)b_{et_i}G_i^* \tag{2.19}$$

$$\frac{\partial j^*}{\partial x^*} = F b_{et_i} G_i^* \tag{2.20}$$

$$j^* = -F\frac{D_{eff}}{2t_+(1-t_+)}\left(\frac{F}{RT}c^*\frac{\partial \phi^*}{\partial x^*} - (1-2t_+)\frac{\partial c^*}{\partial x^*}\right) \tag{2.21}$$

where $i = a$ in the anode and $i = c$ in the cathode. Here the effective diffusitivity, $D_{eff} = \frac{B_{11}2D_nD_p}{D_n+D_p}$ (where B_{11} is the 11-component of the permeability tensor which describes the ease with which a substance can diffuse through the tortuous electrolyte paths in the electrode), b_{et} is the BET surface area (i.e. the surface area of particles per unit volume of electrode) and ϵ_v is the volume fraction of the electrolyte and t_+ is the transference number defines by

$$t_+ = \frac{D_p}{D_n + D_p}. \tag{2.22}$$

Notably (2.21) gives the effective electrical conductivity of electrolyte as

$$\kappa(c^*) = \frac{D_{eff} F^2 c^*}{2RTt_+(1-t_+)} \tag{2.23}$$

which in this dilute solution theory is linearly concentration-dependent [90]. It turns out that this dependence of conductivity on concentration is not realistic for many of the electrolytes used in real battery and this motivates us to look at models for moderately concentrated electrolytes in Chapter 3.

The electrode equations (2.18), after the homogenisation process are

$$(1-\epsilon_{v_a})\frac{\partial c^*_{sa}}{\partial t^*} = -b_{et_a} G^*_a, \qquad (1-\epsilon_{v_c})\frac{\partial c^*_{sc}}{\partial t^*} = -b_{et_c} G^*_c \tag{2.24}$$

2.5.1 The current collectors

At the anodic and cathodic current collectors we assume that the fluxes of the ions are both zero

$$\left.\frac{\partial c^*}{\partial x^*}\right|_{x^*=0} = 0, \qquad \left.\frac{\partial c^*}{\partial x^*}\right|_{x^*=2L} = 0 \tag{2.25}$$

and that the current transfers between the current collectors and the electrolyte are

$$j^*|_{x^*=0} = 0, \qquad j^*|_{x^*=2L} = 0 \tag{2.26}$$

2.5.2 The separator

The separator is thin insulating porous spacer that stops direct contact between anode and cathode particles but allow flow of ions through its pores (see Figure 1.1) [44]. Assuming the separator is thin then the ion fluxes, the electrolyte potential and electric field in the electrolyte are all continuous so that

$$[c^*]_{x^*=L} = 0, \quad \left[\frac{\partial c^*}{\partial x^*}\right]_{x^*=L} = 0, \quad [j^*]_{x^*=L} = 0, \quad [\phi^*]_{x^*=L} = 0 \tag{2.27}$$

2.5.3 The initial conditions

We assume that before the discharge process begins the battery is fully charged in an equilibrium state. This corresponds to the initial conditions

$$c^*(0,x^*) = C_0, \qquad c^*_{sa}(0,x^*)|_{0<x^*<L} = C_a^{max}, \qquad c^*_{sc}(0,x^*)|_{L<x^*<2L} = 0 \tag{2.28}$$

that is the anode particles are full of lithium while the cathode particles are empty.

2.5.4 The relation between current and global reaction rate

Let I^* be the total current flowing through cell. The total charge released by the anode particles must equal the charge absorbed by the cathode particles. By taking a representative cylindrical volume through the whole cell of cross-sectional A (where b_{et} is the active surface area per unit volume of electrode particles), due to charge conservation, we can express the integral of the reaction rates of the two electrodes in terms of the current I^* by

$$Ab_{et_a}F\int_0^L G_a^*(\phi^*)dx^* = -Ab_{et_c}F\int_L^{2L} G_c^*(\phi^*)dx^* = I^* \tag{2.29}$$

It follows that $b_{et_a}\int_0^L G_a^*(\phi^*)dx^* + b_{et_c}\int_L^{2L} G_c^*(\phi^*)dx^* = 0$. When posing the problem we can either specify I^* as an input variable and V^* as the output (galvanostatic discharge) or we can specify V^* and determine I^* (potentiostatic discharge).

2.5.5 Summary of the battery model and comparison to other models

To summarise, a homogenised model of a battery based on Poisson-Nernst-Planck (PNP) equations for a dilute electrolyte, and assuming fast diffusion in the electrode particles, has the form

$$\epsilon_{v_i}\frac{\partial c^*}{\partial t^*} - \frac{\partial}{\partial x^*}\left(D_{eff}\frac{\partial c^*}{\partial x^*}\right) = (1-t_+)b_{et_i}G_i^* \tag{2.30}$$

$$\frac{\partial j^*}{\partial x^*} = Fb_{et_i}G_i^* \tag{2.31}$$

$$j^* = -F\frac{D_{eff}}{2t_+(1-t_+)}\left(\frac{F}{RT}c^*\frac{\partial \phi^*}{\partial x^*} - (1-2t_+)\frac{\partial c^*}{\partial x^*}\right) \tag{2.32}$$

$$G_a^* = \frac{i_{0a}}{F}\left(\exp\left[\frac{-F}{2RT}(\phi^* + U_{eqa}^*(c_{sa}^*)\right] - \exp\left[\frac{F}{2RT}(\phi^* + U_{eqa}^*(c_{sa}^*))\right]\right) \quad \text{in } 0 < x^* < L \tag{2.33}$$

$$G_c^* = \frac{i_{0c}}{F}\left(\exp\left[\frac{-F}{2RT}(\phi^* - V^* + U_{eqc}^*(c_{sc}^*))\right] - \exp\left[\frac{F}{2RT}(\phi^* - V^* + U_{eqc}^*(c_{sc}^*))\right]\right) \quad \text{in } L < x^* < 2L \tag{2.34}$$

$$(1-\epsilon_{v_a})\frac{\partial c_{sa}^*}{\partial t^*} = -b_{et_a}G_a^*, \qquad \text{in } 0 < x^* < L \tag{2.35}$$

$$(1-\epsilon_{v_c})\frac{\partial c_{sc}^*}{\partial t^*} = -b_{et_c}G_c^*, \qquad \text{in } L < x^* < 2L \tag{2.36}$$

$$\left.\frac{\partial c^*}{\partial x^*}\right|_{x^*=0} = 0, \ \left.\frac{\partial c^*}{\partial x^*}\right|_{x^*=2L} = 0 \tag{2.37}$$

$$j^*|_{x^*=0} = 0, \ j^*|_{x^*=2L} = 0 \tag{2.38}$$

$$[c^*]_{x^*=L} = 0, \ \left[\frac{\partial c^*}{\partial x^*}\right]_{x^*=L} = 0, \ [j^*]_{x^*=L} = 0, \ [\phi^*]_{x^*=L} = 0 \tag{2.39}$$

$$c^*(0,x^*) = C_0, \tag{2.40}$$

$$c^*_{sa}(0,x^*)|_{0<x^*<L} = C_a^{max}, \quad c^*_{sc}(0,x^*)|_{L<x^*<2L} = 0 \tag{2.41}$$

$$b_{et_a} F \int_0^L G_a^*(\phi^*)dx^* = -b_{et_c} \int_L^{2L} G_c^*(\phi^*)dx^* = \frac{I^*}{A} \tag{2.42}$$

where the suffix $i = a$ denotes the anode ($0 < x^* < L$) and $i = c$ denotes the cathode ($L < x^* < 2L$). Here the transference number t_+ and the effective diffusivity D_{eff} are given by

$$t_+ = \frac{D_p}{D_n + D_p}, \qquad D_{eff} = \frac{2B_{11}(D_n D_p)}{D_n + D_p)}, \tag{2.43}$$

respectively and the conductivity is given by

$$\kappa(c^*) = D_{eff} \frac{F^2 c^*}{2t_+(1-t_+)RT} \tag{2.44}$$

This system of equations is similar to the macroscopic Newman model [29, 28, 23, 25] for which there is no systematic derivation. It is notable that using this technique, the permeability factor B_{11} appears which accounts for the detailed microstructure of the electrode (and can be calculated using the recipe in [74]). The permeability factor appears both in the effective diffusivity and the effective conductivity of the electrolyte. The derivation also illustrates that the factor $(1 - 2t_+)$ appearing in (2.32) differs from the equivalent factor in Newman's model [28] which is $(1 - t_+)$. Richardson *et al.* [74] claim that the difference comes about because [28] uses the concentrated solution theory instead of the dilute solution although we believe that in fact this is due to potential in the Newman model being measured with respect to a Lithium electrode rather than being an absolute potential as here (see Chapter 3 for more details).

2.6 Numerical and analytical solutions for the full cell model

The forward (oxidation) and backward (reduction) for electron transfer at the electrode particles surfaces is describe by Butler Volmer equations (2.33) and (2.34). When the battery operates far from equilibrium these Butler Volmer equations can be approximated by Tafel equations [4] in which either the reduction, or oxidation, transfer is

switched off depending upon whether the cell is charging or discharging. In this section we introduce Tafel reaction kinetics and present some model solutions base on this approximation. The model is solved analytically in quasi steady state with uniform equilibrium potentials. This analytical solution allow us to validate the numerical results and can be used to explain how the electrolyte concentration is depleted when large currents are applied.

Equilibrium solution At equilibrium $I^* = 0$ and $G_a^* = G_c^* = 0$ and the solution to (2.30) - (2.42) is

$$\phi^* = -U_{eqa}^*, \qquad V^* = U_{eqc}^* - U_{eqa}^* \tag{2.45}$$

2.6.1 Nondimensionalization

To nondimensionalize the model we let $\bar{J}$ represents the typical current density, A is the the cross-sectional area, $\bar{J}A$ represents the magnitude of the typical current, and b_{et_a} and b_{et_c} are the typical BET surface area in anode and cathode. Away from equilibrium we write (2.45) in the form

$$\phi^* = -U_{eqa,0} + \widetilde{\Phi}\phi, \qquad V^* = U_{eqc,0} - U_{eqa,0} + \widetilde{\Phi}V \tag{2.46}$$

and

$$U_{eqa}^* = U_{eqa,0} + \widetilde{\Phi}U_a(c_{sa}), \qquad U_{eqc}^* = U_{eqc,0} + \widetilde{\Phi}U_c(c_{sc}) \tag{2.47}$$

where $\widetilde{\Phi} = \frac{RT}{F}$ is the thermal voltage which is, at room temperature, about $25mV$.

We then nondimensionalise of (2.30)-(2.42) as follows

$$\begin{aligned} x^* &= Lx, \quad c^* = C_0 c, \quad c_{sa}^* = C_{sa,max}c_{sa}, \quad c_{sc}^* = C_{sc,max}c_{sc}, \quad t^* = \tau t, \\ j^* &= \bar{J}j, \quad I^* = \bar{J}A(\bar{I}), \quad G_i^* = \frac{\bar{J}}{Lb_{et_i}F}G_i, \quad V^* = \widetilde{\Phi}V \quad \phi^* = \widetilde{\Phi}\phi \end{aligned} \tag{2.48}$$

where L is the thickness of the electrode, $C_{sa,max}$ and $C_{sc,max}$ are the maximum concentration in the anode and cathode electrodes, C_0 is the typical concentration of lithium ions in the electrolyte. Here LA gives an approximation of the electrode volume and the number of moles of intercalated lithium is thus of size $O(C_{s,max}LA)$. Thus where lithium is consumed at a rate of $\overline{J}A/F$, we expect the timescale τ for discharge to be given by

$$\tau = \frac{LFC_{sc,max}}{\bar{J}}. \tag{2.49}$$

On defining the dimensionless parameters

$$\gamma = \frac{D_{eff}FC_0}{\bar{J}L(1-t_+)}, \quad \Omega_a = \frac{Lb_{et_a}i_{0a}}{\bar{J}}, \quad \Omega_c = \frac{Lb_{et_c}i_{0c}}{\bar{J}}, \tag{2.50}$$

$$\Gamma = \frac{\bar{J}L}{FD_{eff}C_{sc,max}}, \qquad \chi = \frac{c_{sc,max}}{c_{sa,max}} \tag{2.51}$$

and nondimensionalising (2.30)-(2.42) using (2.46)-(2.48), we obtain the dimensionless system

$$\Gamma\epsilon_v\frac{\partial c}{\partial t} - \gamma\frac{\partial^2 c}{\partial x^2} = \frac{1}{\gamma}\begin{cases} G_a(c_{sa},\phi), & \text{if } 0<x<1 \\ G_c(c_{sc},\phi), & \text{if } 1<x<2 \end{cases} \tag{2.52}$$

$$\frac{\partial j}{\partial x} = \begin{cases} G_a(c_{sa},\phi), & \text{if } 0<x<1 \\ G_c(c_{sc},\phi), & \text{if } 1<x<2 \end{cases} \tag{2.53}$$

$$j = -\frac{\gamma}{2t_+}c\left(\frac{\partial\phi}{\partial x} - (1-2t_+)\frac{\partial \log c}{\partial x}\right) \tag{2.54}$$

$$(1-\epsilon_v)\frac{\partial c_{sa}}{\partial t} = -\chi G_a(c_{sa},\phi), \quad \text{if } 0<x<1 \tag{2.55}$$

$$(1-\epsilon_v)\frac{\partial c_{sc}}{\partial t} = -G_c(c_{sc},\phi), \quad \text{if } 1<x<2 \tag{2.56}$$

$$\left.\frac{\partial c}{\partial x}\right|_{x=0} = 0, \qquad j|_{x=0} = 0, \tag{2.57}$$

$$\left.\frac{\partial c}{\partial x}\right|_{x=2} = 0, \qquad j|_{x=2} = 0 \tag{2.58}$$

$$[c]_{x=1} = 0, \qquad \left[\frac{\partial c}{\partial x}\right]_{x=1} = 0, \qquad [j]_{x=1} = 0, \qquad [\phi]_{x=1} = 0 \tag{2.59}$$

$$c(0,x) = 1, \tag{2.60}$$

$$c_{sa}(0,x) = 1 \quad \text{if} \quad 0<x<1, \qquad c_{sc}(0,x) = 0 \quad \text{if} \quad 1<x<2 \tag{2.61}$$

$$\int_0^1 G_a(c_{sa},\phi)dx = -\int_1^2 G_c(c_{sc},\phi)dx = \bar{I} \tag{2.62}$$

where the dimensionless reaction rates are given by

$$G_a = \Omega_a\left(\exp\left[-\frac{1}{2}(\phi + U_a(c_{sa}))\right] - \exp\left[\frac{1}{2}(\phi + U_a(c_{sa}))\right]\right) \quad \text{if} \quad 0<x<1 \tag{2.63}$$

$$G_c = \Omega_c\left(\exp\left[-\frac{1}{2}(\phi - V + U_c(c_{sc}))\right] - \exp\left[\frac{1}{2}(\phi - V + U_c(c_{sc}))\right]\right) \quad \text{if} \quad 1<x<2 \tag{2.64}$$

Parameter	Value	
Electrolyte Parameters		
Diffusivity of Lithium ions, D_{eff} (m^2s^{-1})	5.34×10^{-10} [32]	
Volume fraction, ϵ_v	0.4764	
Initial salt concentration, c_0 $(molm^{-3})$	1000 [23]	
Transference number, t_+	0.38 [90]	
Electrode Parameters	LiC_6	$LiFePO_4$
Radius of particle, a (m)	1.1×10^{-5} [85]	5.2×10^{-8} [85]
Exchange current density, i_0 (Am^{-2})	30 [32]	5.4×10^{-5} [23]
BET surface area, b_{et} (m^{-1})	2×10^4	5×10^7
Maximum concentration in the solid, $C_{s,max}$ $(molm^{-3})$	30000 [85]	20950 [23]
Other Parameters		
Electrode thickness, L (m)	6.25×10^{-5} [23]	
Faraday constant, F $(Cmol^{-1})$	96487 [23]	
Universal gas constant, R $(Jmol^{-1}K^{-1})$	8.3144 [23]	
Temperature, T (K)	298 [23]	
Electrode area, A (m^2)	10^{-4} [23]	

Table 2.1: Parameter values used in the model.

2.6.1.1 Size of dimensionless parameters

In the above equations, γ is the maximum sustainable flux of ions in the electrolyte to the actual ion flux. Ω_a and Ω_c are the dimensionless reaction rates on the anode particles and cathode particles respectively. To estimate the size of the typical size of dimensional parameters in the problem we use the data listed in Table 2.1. Note that i_{oa} and i_{oc} values depend upon the electrode material. The BET surface area b_{et_i} (by considering a periodic cube contains one spherical particle of radius a where the particle just touches its neighbours) is the surface area of the spherical particle divided by the volume of the periodic cube such that

$$b_{et} = \frac{\text{Surface are of particle}}{\text{Volume of periodic cube}} = \frac{4\pi a^2}{8a^3} = \frac{\pi}{2a}. \tag{2.65}$$

We now use these dimensional parameters listed in Table 2.1 to estimate the size of the key dimensionless parameters as follows

$$\gamma \approx 25, \qquad \Omega_c \approx 10^{-3}, \qquad \Omega_a \approx 10^{-2}, \qquad \Gamma \approx 10^{-4} \tag{2.66}$$

Here we take $\bar{J} = 26Am^{-2}$. Note that if we discharge the cell at a relatively slow rate, than Γ is estimated to be extremely small (10^{-4}) and that will allow us to solve a quasi-steady state problem for the concentration in the electrolyte.

2.6.2 The Tafel equation approximation for $\Omega_a << 1$ and $\Omega_c << 1$

The Butler-Volmer equation can be approximated by the Tafel equation in the limit that Ω_a and Ω_c are small. During discharge, the current drives the lithium ions from the anode to the cathode ($\bar{I} > 0$), while during charging, the flow of Lithium ions is in reversed $\bar{I} < 0$). If $\bar{I}(t)$ is $O(1)$ and positive it follows that $G_a > 0$ and $G_c < 0$, and both are order $O(1)$ from the integral condition (2.62). Thus, we can rescale the Butler-Volmer relation by writing

$$\phi = -2\log\left(\frac{1}{\Omega_a}\right) + \tilde{\phi}, \qquad V = -2\log\left(\frac{1}{\Omega_a}\right) - 2\log(\frac{1}{\Omega_c}) + \tilde{V} \tag{2.67}$$

The reaction rates of (2.63)-(2.64) can then be approximated by the Tafel equations

$$G_a = \exp\left(-\frac{1}{2}(\tilde{\phi} + U_a(c_{sa})\right) \qquad \text{if} \qquad 0 < x < 1 \tag{2.68}$$

$$G_c = -\exp\left(\frac{1}{2}(\tilde{\phi} - \tilde{V} + U_c(c_{sc}))\right) \quad \text{if} \qquad 1 < x < 2 \tag{2.69}$$

provided $\log(1/\Omega_a) >> 1$ and $\log(1/\Omega_c) >> 1$. Here $\tilde{V}$ is now the unknown parameter we are looking for.

2.6.3 The quasi steady approximations for $\Gamma << 1$

Provided that the rate of discharge is not very fast, we expect that Γ to be small, thus we can neglect the $\dfrac{\partial c}{\partial t}$ term in (2.52) and solve the quasi steady-state problem. Before taking the limit $\Gamma \to 0$, we note first that by integrating (2.52) between $x = 0$ and $x = 2$, applying the boundary conditions (2.57)-(2.58) and the integral conditions (2.62), we find $\dfrac{d}{dt}\left(\displaystyle\int_0^2 c dx\right) = 0$ and hence from the initial condition (2.60), we have

$$\int_0^2 c\, dx = 2 \tag{2.70}$$

Taking the limit $\Gamma \to 0$ in (2.52) gives the quasi-steady equation

$$-\gamma\frac{\partial^2 c}{\partial x^2} = \begin{cases} G_a(x,t), & 0 < x < 1 \\ G_c(x,t), & 1 < x < 2 \end{cases} \tag{2.71}$$

Combination of equations (2.53) and (2.54) gives

$$\frac{\partial j}{\partial x} = -\frac{\gamma}{2t_+}\frac{\partial}{\partial x}\left(c\frac{\partial\tilde{\phi}}{\partial x} - (1-2t_+)\frac{\partial c}{\partial x}\right) = \begin{cases} G_a(x,t) & 0 < x < 1 \\ G_c(x,t) & 1 < x < 2 \end{cases} \tag{2.72}$$

Then by equating equations (2.71) and (2.72) we find

$$-\gamma\frac{\partial^2 c}{\partial x^2} = -\frac{\gamma}{2t_+}\frac{\partial}{\partial x}\left(c\frac{\partial\tilde{\phi}}{\partial x} - (1-2t_+)\frac{\partial c}{\partial x}\right) \tag{2.73}$$

which can be simplified to the integrable equation

$$\frac{\partial}{\partial x}\left(\frac{\partial c}{\partial x} - c\frac{\partial\tilde{\phi}}{\partial x}\right) = 0. \tag{2.74}$$

Integrating (2.74) and applying the boundary conditions (2.57) to (2.74) then gives

$$\frac{\partial c}{\partial x} - c\frac{\partial\tilde{\phi}}{\partial x} = 0 \tag{2.75}$$

Equation (2.75) states that there is zero flux of the negative counterion through the device. Solutions of this equation have the form;

$$c(x,t) = A(t)\exp(\tilde{\phi}(x,t)) \tag{2.76}$$

or alternatively

$$\tilde{\phi}(x,t) = \log\left(\frac{c(x,t)}{A(t)}\right). \tag{2.77}$$

Hence, we can eliminate $\tilde{\phi}$ from (2.68)-(2.69) and (2.71) to give a problem with one fewer dependant variables

$$-\gamma\frac{\partial^2 c}{\partial x^2} = \begin{cases} \exp\left(-\frac{1}{2}\left(\log\left(\frac{c}{A(t)}\right) + U_a(c_{sa}(x,t))\right)\right), & \text{if} \quad 0<x<1 \\ -\exp\left(\frac{1}{2}\left(\log\left(\frac{c}{A(t)}\right) - \tilde{V} + U_c(c_{sc}(x,t))\right)\right), & \text{if} \quad 1<x<2 \end{cases} \tag{2.78}$$

2.6.4 Solution for flat discharge curves

We now look at finding solutions to the model with the above assumptions (quasi-state discharge and Tafel reaction equations) and in addition we will assume that both the anode and cathode materials have flat discharge curves. This last corresponds to the assumption that $U_a(c_{sa})$ and $U_c(c_{sc})$ are only very weakly dependant on c_{sa} and c_{sc} (e.g this would be for a $LiFePO_4$ cathode). This allows us to assume that $U_a(c_{sa})$ and $U_c(c_{sc})$ are constant until fully discharged (i.e. $c_{sa} = 0$ and $c_{sc} = 1$) at which point the

equilibrium potentials become large and effectively shut off the reaction rate; thus

$$U_a(c_{sa}) = \begin{cases} \infty, & \text{if } c_{sa} \le 0 \\ U_{a0}, & \text{if } 0 < c_{sa} \le 1 \end{cases} \tag{2.79}$$

$$U_c(c_{sc}) = \begin{cases} U_{c0}, & \text{if } 0 \le c_{sc} < 1 \\ -\infty, & \text{if } c_{sc} \ge 1 \end{cases} \tag{2.80}$$

Solution before the particles are fully discharged. Before the particles are fully discharged, (2.78) can be rewritten as

$$-\gamma \frac{\partial^2 c}{\partial x^2} = \begin{cases} \exp\left(-\frac{1}{2}\left(\log\left(\frac{c}{A}\right) + U_{a0}\right)\right), & \text{if} \quad 0 < x < 1,\ 0 < c_{sa} \le 1 \\ -\exp\left(\frac{1}{2}\left(\log\left(\frac{c}{A}\right) - \tilde{V} + U_{c0}\right)\right), & \text{if} \quad 1 < x < 2,\ 0 \le c_{sc} < 1 \end{cases} \tag{2.81}$$

By expressing the parameters in (2.81) as follows,

$$\begin{aligned} A = \exp(-W), \qquad & \tilde{V} = W + U_{a0} + U_{c0} - \log(A), \\ \beta \;\; = \;\; & \exp\left(-\frac{W}{2} - \frac{U_{a0}}{2}\right), \end{aligned} \tag{2.82}$$

we can write the model (2.81) with boundary conditions (2.57(a)), (2.58(a)), and (2.59(a),(b)), (2.62) and (2.70) as follows

$$\frac{\partial^2 c}{\partial x^2} = \begin{cases} -\frac{\beta}{\gamma} c^{-1/2}, & \text{if} \quad 0 < x < 1 \\ \frac{\beta}{\gamma} c^{1/2}, & \text{if} \quad 1 < x < 2 \end{cases} \tag{2.83}$$

subject to the conditions

$$\left.\frac{\partial c}{\partial x}\right|_{x=0} = 0, \quad \left.\frac{\partial c}{\partial x}\right|_{x=2} = 0, \tag{2.84}$$

$$\left[\frac{\partial c}{\partial x}\right]_{x=1} = 0, \quad [c]_{x=1} = 0 \tag{2.85}$$

$$\int_0^2 c\, dx = 2 \tag{2.86}$$

$$\beta \int_0^1 c^{-1/2}\, dx = \beta \int_1^2 c^{1/2}\, dx = \bar{I}. \tag{2.87}$$

With the same rescaling, the concentration in the solid equations (2.55) and (2.56) with Tafel kinetics (2.68)-(2.69) can be rewritten as

$$(1-\epsilon_v)\frac{\partial c_{sa}}{\partial t} = \chi\beta c^{-1/2}, \qquad 0<x<1 \tag{2.88}$$

$$(1-\epsilon_v)\frac{\partial c_{sc}}{\partial t} = -\beta c^{1/2} \qquad 1<x<2 \tag{2.89}$$

$$c_{sa}(0,x) = 1, \qquad c_{sc}(0,x)=1. \tag{2.90}$$

Here $\bar{I}$ is an unknown constant that we shall determine as part of the solution and β is a specified parameter (alternatively we could specify $\bar{I}$ and determine β). We note that β is specify so that it satisfies the integral condition (2.86). Once we have solved (2.83)-(2.86) to determine $c(x)$ for a given value of β we can use (2.87) to determine the corresponding current, $\bar{I}$. When we solve the second order differential system (2.83)-(2.85) analytically, we obtain the implicit solution

$$x = \begin{cases} \frac{2}{3}\sqrt{\frac{\gamma}{\beta}}\sqrt{c(0)^{1/2}-c(x)^{1/2}}(2c(0)^{1/2}+c(x)^{1/2}), & 0<x<1 \\ 2+i\sqrt{\frac{3\gamma}{\beta}}c(2)^{1/4}\left(\frac{c(x)}{c(2)}\text{Hypergeometric}_2F_1\left(\frac{2}{3},\frac{1}{2},\frac{5}{3},\left[\frac{c(x)}{c(2)}\right]^{3/2}\right)-\sqrt{\pi}\frac{\Gamma(5/3)}{\Gamma(7/6)}\right), & 1<x<2 \end{cases} \tag{2.91}$$

This analytical result will be compared to the numerical solution. The result is coupled to (2.88)-(2.90) for the time dependant concentration in the electrode particles.

Numerical procedure Equations (2.83)-(2.85) has been solved for c and $\tilde{\phi}$ using Matlab 'bvp4c' (boundary value problem solver). The current, $\bar{I}$ is determined by the Newton method which satisfies the integral conditions (2.87). The concentration in the solid in (2.88)-(2.90) are numerically solved using Forward Euler method.

2.6.5 Results and Discussion

Figure 2.5 shows the comparison of steady state analytic solution (2.91) against numerical simulation for the equation (2.83)-(2.87). The graph shows that the analytical solution compares well with the numerical simulation. The dimensionless parameters values (refer Table 2.1 for the values of dimensional parameters) used to obtain the results are listed in Table 2.2.

The results for lithium concentration, electric potential in electrolyte and concentration of lithium in solid will be presented as a function of position (x) where the anode and cathode current collectors are at $x=0$ and $x=2$, respectively, and the separator at $x=1$. Figure 2.6 shows the concentration profile of Lithium ions in the electrolyte phase for different discharge currents $\bar{I}$. The concentration profile has a negative gradient, which decreases, with increases in $\bar{I}$, until full discharge is no longer possible. Increasing $\bar{I}$ further will drive the Lithium ion concentration to zero in the region adjacent to the

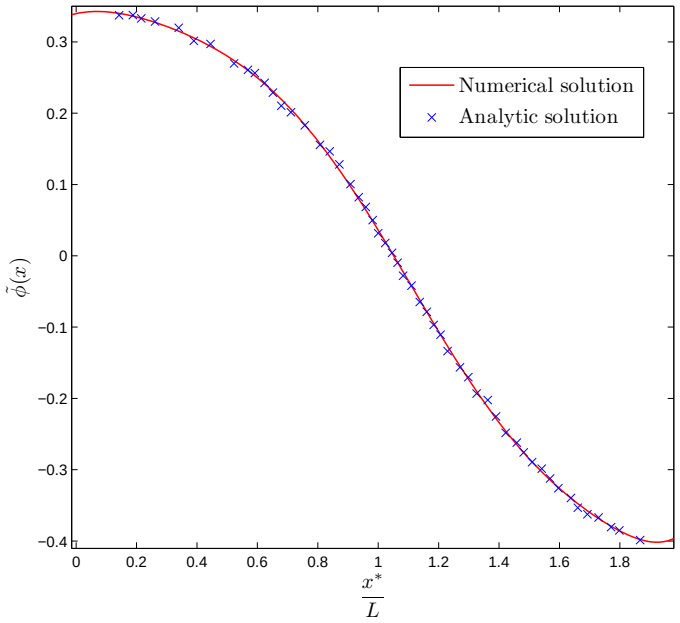

Figure 2.5: The solution of dimensionless electrolyte potential, $\tilde{\phi}(x)$ from (symbols) analytical expression (2.91) compared to (line) numerical simulation using MATLAB 'bvp4c' at discharge current $\bar{I} = 1.32$.

Parameter	Value	Figure(s)
γ	25	
ϵ_v	0.13643	2.5, 2.7, 2.6, 2.8
t_+	0.38	
$\bar{I}$	1.32	2.5
	1.0, 1.2, 1.4, 1.7	2.7, 2.6
	1.0	2.8(a)
	1.5	2.8(b)

Table 2.2: The values of dimensionless parameters for Figure 2.5, Figure 2.7, Figure 2.6 and Figure 2.8.

current collector at $x = 2$. This is thus leads to dead regions of the cathode that are unable to discharge properly. Once this happens the particles in this region can no longer be used because there are no Lithium ions in the solution to insert. The lack of Lithium ions is called a limiting-current phenomenon and has been discussed in [36] and will be investigated further here in §2.7 for a half cell cathode.

The plots of $\tilde{\phi}(x)$, (see Figure (2.7)) shows that potential, $\tilde{\phi}(x)$ is high in the region furthest from the separator in the anode and dropped to a small value near the separator, and goes negative in the cathode.

The lithium concentration c_s in the solid electrode particles in the anode and the cathode

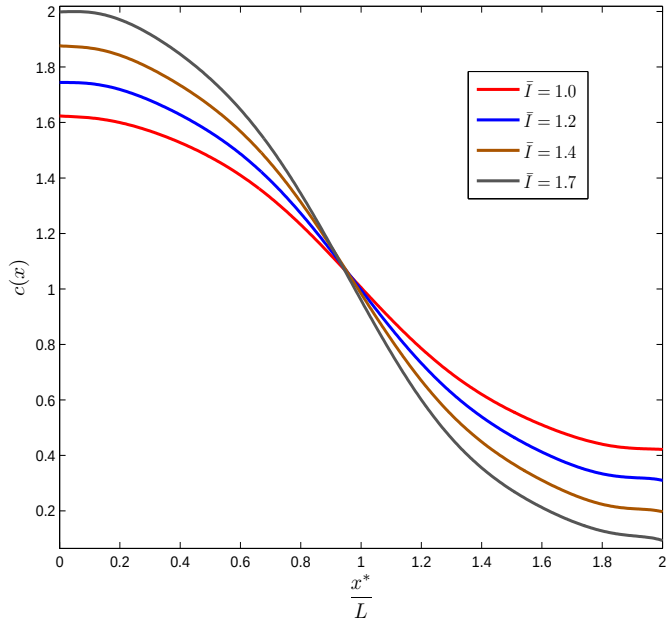

Figure 2.6: Graph of dimensionless electrolyte concentration $c(x)$ at different discharge currents $\bar{I} = 1.0, 1.2, 1.4, 1.7$ as a function of position. This analytical solutions are obtained by equation (2.91).

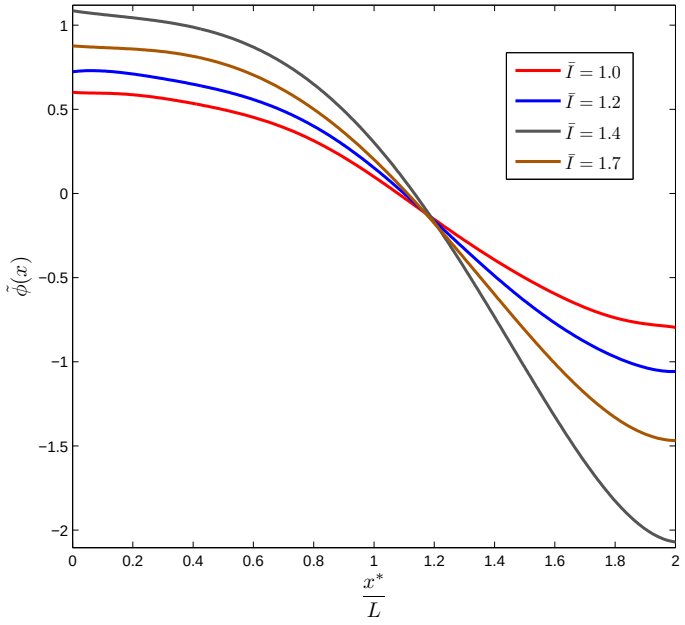

Figure 2.7: Graph of dimensionless electrolyte potential $\tilde{\phi}(x)$ at different discharge currents $\bar{I} = 1.0, 1.2, 1.4, 1.7$ as a function of position. This figure is obtained by relation to the electrolyte concentration as stated in (2.77).

are determined by solving (2.88)-(2.90) numerically. The profiles of lithium concentration in the solid particles in the anode and the cathode are shown in Figure 2.8 at

different discharge currents. Lithium ions are released into the electrolyte from the anode particles, after which they diffuse through the electrolyte to the cathode, where they insert into the particles. The figure shows that the rate of release/insertion are quicker in the region closest to the separator than those in the region furthest from the separator. Figure 2.8(b) depicts scenario in which cell that is discharged at a higher current ($\bar{I} = 1.5$) than in Figure 2.8(a) ($\bar{I} = 1$).

2.7 The half cell cathode model

A schematic of a half cell cathode is shown in Figure 1.4. We use the same model equations (2.30)-(2.32), (2.34) and (2.36) with the following boundary conditions at the separator ($x^* = 0$) and the cathode current collector ($x^* = L$)

$$\phi^*|_{x^*=0} = 0, \qquad c^*|_{x=0} = C_0, \qquad j^*|_{x=0} = -\frac{I}{A}, \tag{2.92}$$

$$\left.\frac{\partial c^*}{\partial x^*}\right|_{x=L} = 0, \qquad j^*|_{x=L} = 0 \tag{2.93}$$

and initial conditions

$$c^*(x^*, 0) = C_0, \qquad c^*_{sc}(x^*, 0) = 0. \tag{2.94}$$

We nondimensionalise the half-cell model using the scaling in (2.48). The dimensionless model for the half cell cathode is similar to that for the full cell, except the cathode now occupies $0 < x < 1$ (rather than $1 < x < 2$), and is given by

$$\Gamma\epsilon_v \frac{\partial c}{\partial t} - \frac{\partial^2 c}{\partial x^2} = \frac{1}{\gamma} G_c(c_s, \phi), \tag{2.95}$$

$$\frac{\partial j}{\partial x} = G_c(c_s, \phi), \tag{2.96}$$

$$j = -\frac{\gamma}{2t_+} c \left(\frac{\partial \phi}{\partial x} - (1 - 2t_+) \frac{\partial \log c}{\partial x} \right) \tag{2.97}$$

$$\phi|_{x=0} = 0, \quad c|_{x=0} = 1, \quad j|_{x=0} = -\bar{I}, \tag{2.98}$$

$$\left.\frac{\partial c}{\partial x}\right|_{x=1} = 0, \quad j|_{x=1} = 0 \tag{2.99}$$

$$(1 - \epsilon_v) \frac{\partial c_{sc}}{\partial t} = -G_c(c_s, \phi), \quad \text{if } 1 < x < 2 \tag{2.100}$$

$$c(0, x) = 1, \qquad c_{sc}(0, x) = 0. \tag{2.101}$$

During discharge, $\bar{I}(t) > 0$ and $G_c < 0$ and of $O(1)$. If we discharge the cell at a slow discharge rate, Ω_c is small and we can once again approximate the Butler Volmer

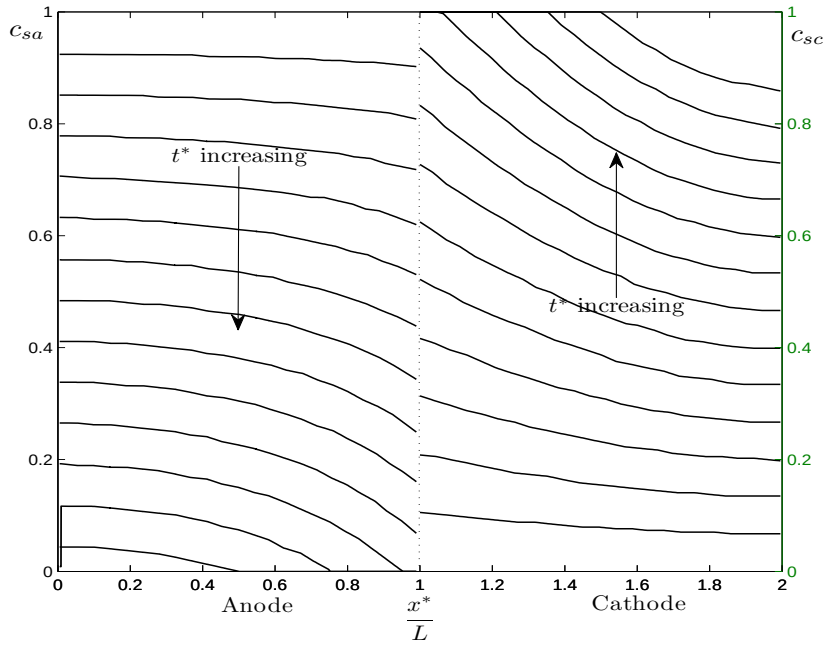

(a) $\bar{I} = 1$

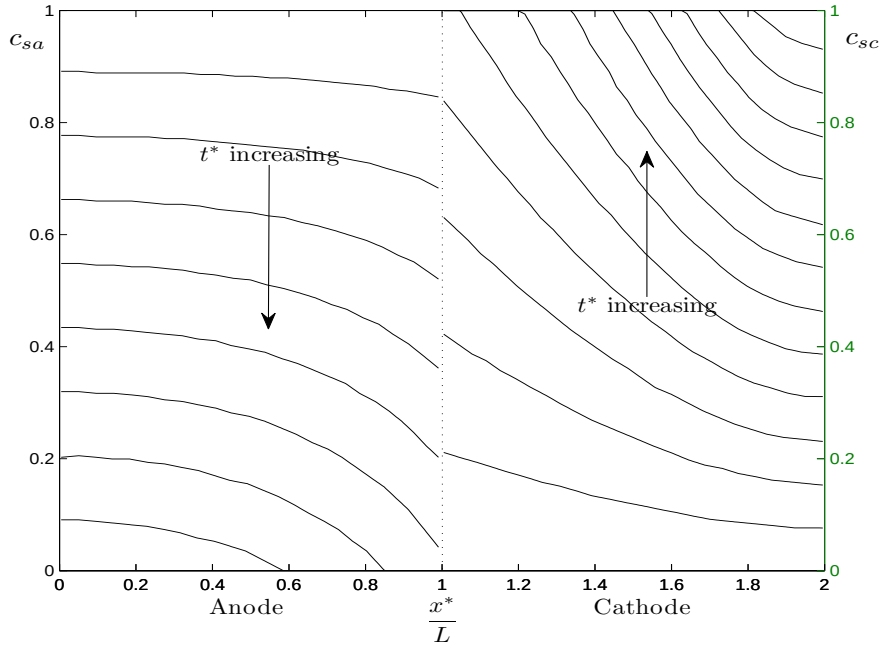

(b) $\bar{I} = 1.5$

Figure 2.8: Dimensionless intercalated Lithium concentration distribution in the particle for anode ($0 < x < 1$) and cathode ($1 < x < 2$), c_{sa} and c_{sc}, respectively (by solving (2.88)-(2.90) numerically) for discharge current (a) $\bar{I} = 1$ and (b) $\bar{I} = 1.5$. Here $0 < x < 1$ is the anode and $1 < x < 2$ is the cathode. The profiles are measured at $t^* = 100s, 200s, 300s, 400s, ...$

equations by the Tafel

$$G_c = -\exp\left(\frac{1}{2}(\phi - \tilde{V} + \tilde{U}_c(c_{sc}))\right) \tag{2.102}$$

by rescaling

$$V = -2\log\left(\frac{1}{\Omega_c}\right) + \tilde{V} \tag{2.103}$$

provided $\log(1/\Omega_c) >> 1$. In the case of a cathode material (such as $LiFePO_4$) with a flat discharge curve, $\tilde{U}_c(c_{sc})$ is constant until the material is almost entirely discharge. The reaction shuts off because of a lack of vacancies in the solid as c_{sc} approaches 1.

2.7.1 Quasi-steady state limit $\Gamma \to 0$

In the limit $\Gamma \to 0$, (2.95)-(2.97) can once again be approximated by the quasi-steady equation

$$-\gamma\frac{\partial^2 c}{\partial x^2} = G_c(x,t) \tag{2.104}$$

$$-\frac{\gamma}{2t_+}\frac{\partial}{\partial x}\left(c\frac{\partial\tilde{\phi}}{\partial x} - (1-2t_+)\frac{\partial c}{\partial x}\right) = G_c(x,t) \tag{2.105}$$

By equating these two equations, integrating in x and applying the appropriate boundary conditions we find

$$c = \exp(\phi) \tag{2.106}$$

or alternatively

$$\phi = \log(c). \tag{2.107}$$

By substituting this relation into (2.104) and (2.102), we obtain an ODE for concentration of electrolyte

$$\frac{\partial^2 c}{\partial x^2} = -\frac{1}{\gamma}G_c(c), \qquad \text{where } G_c(c) = -\sqrt{c}\exp\left(-\frac{1}{2}(V - \tilde{U}_c(c_{sc}(x,t)))\right). \tag{2.108}$$

The boundary conditions for the above system (see (2.98)-(2.99)) are

$$c|_{x=0} = 1, \quad \left.\frac{\partial c}{\partial x}\right|_{x=0} = -\frac{\bar{I}}{\gamma}, \quad \left.\frac{\partial c}{\partial x}\right|_{x=1} = 0 \tag{2.109}$$

Transport of Lithium in the solid particles (as previously stated which is assumed to be fast) is given by

$$(1-\epsilon_v)\frac{\partial c_{sc}}{\partial t} = \sqrt{c}\exp\left(-\frac{1}{2}(V-\tilde{U}_c(c_{sc}(x,t)))\right) \tag{2.110}$$

$$c_{sc}(x,0) = 0. \tag{2.111}$$

2.7.2 Flat discharge curve approximation for $LiFePO_4$ cathode

Once again we assume that the cathode material has a flat discharge curve so that, as previously,

$$\tilde{U}_c(c_{sc}) = \begin{cases} -\infty, & \text{when } c_{sc} \geq 1 \\ U_0, & \text{when } c_{sc} < 1 \end{cases} \tag{2.112}$$

This approximation allows the model to be simulated numerically and semi analytically. The Tafel kinetic from equation (2.102) leads to a free boundary problem, where the free boundary $x = s(t)$ is the front between a region of fully discharged particles ($c_{sc} = 1$) and partially discharge particles ($c_{sc} < 1$) (as illustrated in Figure 2.9). Thus, the free boundary reaction equation (2.102)

$$\begin{aligned} c_{sc} &= 1, \quad G_c = 0 && \text{in } x < s(t) \\ c_{sc} &< 1, \quad G_c = -\sqrt{c}\exp\left[-\frac{1}{2}(V-U_0)\right] && \text{in } x > s(t) \end{aligned} \tag{2.113}$$

Here we specify $\bar{I}$ and seek to determine V.

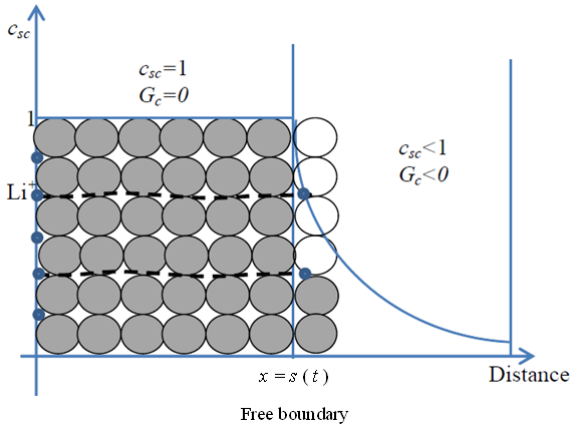

Figure 2.9: The free boundary problem; (a) $x < s(t)$ - Cathode particles are full with Lithium ($c_{sc} = 1$) and (b) $x > s(t)$ - Cathode particles are partially filled ($c_{sc} < 1$)

2.7.3 Analytic solutions

The analytic solutions of the ODE system (2.108)-(2.109) are divided into two regimes; before and after the development of free boundary.

2.7.3.1 Before the development of a free boundary

Since U_0 is constant then the voltage V is also constant. Hence, the ODE system (2.108)-(2.109) can be written as

$$\frac{\partial^2 c}{\partial x^2} = \frac{K}{\gamma}\sqrt{c}. \tag{2.114}$$

$$K = \exp\left(-\frac{1}{2}(V - U_0)\right). \tag{2.115}$$

The boundary conditions in this regimes are as follows

$$c|_{x=0} = 1, \qquad \left.\frac{\partial c}{\partial x}\right|_{x=1} = 0 \tag{2.116}$$

$$\left.\frac{\partial c}{\partial x}\right|_{x=0} = -\frac{\bar{I}}{\gamma}. \tag{2.117}$$

Solving (2.114) with the boundary condition (2.116(b)) we obtain

$$\frac{\partial c}{\partial x} = -\sqrt{\frac{K}{\gamma}}\sqrt{\frac{4}{3}}\sqrt{c(x)^{3/2} - c(1)^{3/2}}. \tag{2.118}$$

Integrating this and applying the boundary condition (2.116(a)), we get

$$-\frac{2}{\sqrt{3}}\sqrt{\frac{K}{\gamma}}x = ic(1)^{-3/4}\left[c(x)\text{Hypergeometric}_2F_1\left(\frac{2}{3},\frac{1}{2},\frac{5}{3},\left[\frac{c(x)}{c(1)}\right]^{3/2}\right)\right.$$
$$\left.-\text{Hypergeometric}_2F_1\left(\frac{2}{3},\frac{1}{2},\frac{5}{3},\left[\frac{1}{c(1)}\right]^{3/2}\right)\right]. \tag{2.119}$$

Applying the boundary condition (2.117) to the solution (2.118) we obtain an equation for constant K which is

$$K = \frac{3}{4}\frac{\bar{I}^2}{\gamma}\frac{1}{1 - c(1)^{3/2}}. \tag{2.120}$$

We determine the half cell voltage, V from (2.120) by recalling (2.115); thus

$$V = -2\log\left(\frac{3}{4}\frac{\bar{I}^2}{\gamma}\frac{1}{1 - c(1)^{3/2}}\right) + U_0 \tag{2.121}$$

Thus at zero current ($\bar{I} = 0$), $V = U_0$, but as the current increases so V decreases.

The concentration in the solid, c_{sc} is obtained by solving (2.110) numerically. Alternatively, we can solve (2.110) analytically since $G_c(c)$ is x-dependent only which gives

$$c_{sc}(x,t) = \frac{t\sqrt{c}}{(1-\epsilon_v)} \exp\left(-\frac{1}{2}(V - U_0)\right). \tag{2.122}$$

Numerical solution procedure We solve the half-cell model (2.114)-(2.116) in x for c, using Matlab 'bvp4c'. The current, $\bar{I}$ is specified by equation (2.117) and the Newton method is used for the accuracy of the approximations . The concentration in the solid problem (2.110)-(2.111) is solved using Forward Euler method.

2.7.3.2 After development of free boundary

When the free boundary develops the ODE system (2.108)-(2.109) can be written as

$$\frac{\partial^2 c}{\partial x^2} = \begin{cases} 0, & \text{if} \quad x \le s(t) \\ \frac{K\sqrt{c}}{\gamma}, & \text{if} \quad x > s(t) \end{cases} \tag{2.123}$$

where

$$K = \exp\left(-\frac{1}{2}(V - U_0)\right). \tag{2.124}$$

The boundary conditions for the region $x \le s(t)$ are as follows

$$c|_{x=0} = 1, \qquad \left.\frac{\partial c}{\partial x}\right|_{x=0} = -\frac{\bar{I}}{\gamma}. \tag{2.125}$$

The lithium concentration in the solid equation (2.110) can be written as

$$(1-\epsilon_v)\frac{\partial c_{sc}}{\partial t} = \begin{cases} 0, & \text{if} \quad x \le s(t) \\ \frac{K\sqrt{c}}{\gamma}, & \text{if} \quad x > s(t) \end{cases} \tag{2.126}$$

$$c_{sc}(x,0) = 0. \tag{2.127}$$

The analytical solution of (2.123) for $x \le s(t)$ (where $G_c = 0$) with boundary conditions (2.125) is given by

$$c = -\frac{\bar{I}}{\gamma}x + 1 \qquad \text{for} \qquad x \le s(t). \tag{2.128}$$

Evaluating (2.128) at $x = s(t)$ gives the boundary conditions for ODE system (2.123) for $x > s(t)$ which are

$$c|_{x=s(t)} = -\frac{\bar{I}}{\gamma}s(t) + 1, \quad \left.\frac{\partial c}{\partial x}\right|_{x=1} = 0 \tag{2.129}$$

$$\left.\frac{\partial c}{\partial x}\right|_{x=s(t)} = -\frac{\bar{I}}{\gamma} \tag{2.130}$$

The analytic solution of the second order differential equation (2.123) with the boundary condition (2.129(b)) is

$$\frac{\partial c}{\partial x} = -\sqrt{\frac{K}{\gamma}}\sqrt{\frac{4}{3}}\sqrt{c(x)^{3/2} - c(1)^{3/2}}. \tag{2.131}$$

Integrating this and once again applying the boundary condition (2.129(a)), we get

$$\begin{aligned} -\frac{2}{\sqrt{3}}\sqrt{\frac{K}{\gamma}}x = {} & -ic(1)^{-3/4}\sqrt{c(s(t))^{3/2} - c(1)^{3/2}}\left[c(x)\text{Hypergeometric}_2F_1\left(\frac{2}{3}, \frac{1}{2}, \frac{5}{3}, \left[\frac{c(x)}{c(1)}\right]^{3/2}\right)\right. \\ & \left. -c(s(t))\text{Hypergeometric}_2F_1\left(\frac{2}{3}, \frac{1}{2}, \frac{5}{3}, \left[\frac{c(s(t))}{c(1)}\right]^{3/2}\right)\right] \end{aligned} \tag{2.132}$$

Applying the boundary condition (2.130) to the solution (2.131), we obtain an equation for constant K which is

$$K = \frac{3}{4}\frac{\bar{I}^2}{\gamma}\frac{1}{c(s(t))^{3/2} - c(1)^{3/2}}. \tag{2.133}$$

The half cell voltage, V is calculated by applying the boundary condition (2.130) to the solution (2.131) and recalling that K is given by (2.124).

$$V(t) = -2\log\left(\frac{3}{4}\frac{\bar{I}^2}{\gamma}\frac{1}{c(s(t),t)^{3/2} - c(1,t)^{3/2}}\right) + U_0. \tag{2.134}$$

Hence for fixed $\bar{I}$ as the free boundary $s(t)$ increases with time, and $c(x,t)$ decreases with x, the half cell voltage V decreases with time.

Note that although the analytical solutions (2.119) and (2.132) for $c(x)$ contain complex constant, $i = \sqrt{-1}$, they are in fact real.

Numerical solution procedure We solve the half-cell model (2.123)-(2.125) in x for c, using Matlab 'bvp4c'. The current, $\bar{I}$ is specified by equation (2.130) and the Newton method is used for the accuracy of the approximations . The concentration in the solid problem (2.126)-(2.127) is solved using Forward Euler method.

2.7.3.3 Results and discussion

Parameter	Value	Figure
γ	20	
ϵ_v	0.4764	2.10, 2.11, 2.12, 2.13
t_+	0.38	
$\bar{I}$	0.5	2.10, 2.11, 2.12
	1	2.13

Table 2.3: The values of dimensionless parameters for Figure 2.10, Figure 2.11, Figure 2.12 and Figure 2.13.

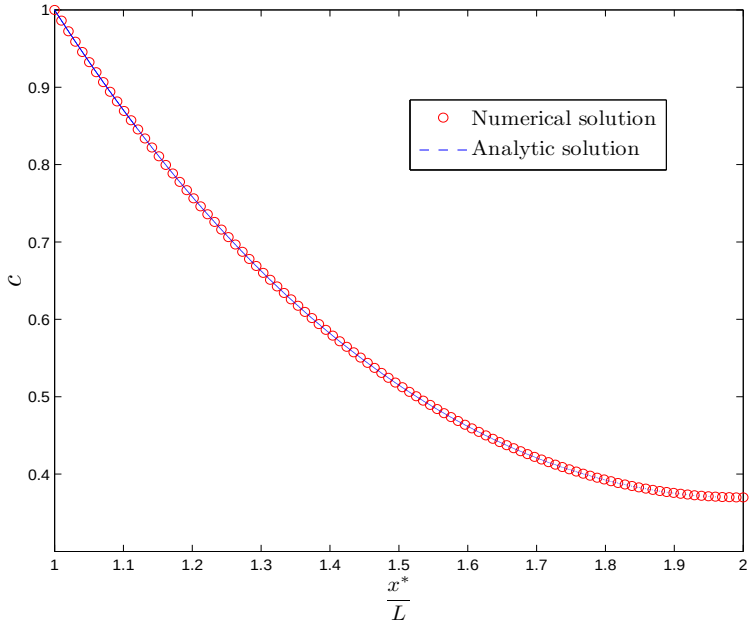

Figure 2.10: Dimensionless concentration profiles of the model before the free boundary develops by (symbol) analytical solution (2.119) and (solid line) numerical simulation for $\bar{I} = 1$.

The dimensionless parameter values used to obtain the solution are listed in Table 2.3. The analytical solution (2.119) has been validated against the numerical simulation in Figure 2.10. It is observed that the numerical procedure predicts the concentration profiles accurately. Initially, the concentration of electrolyte is uniform, until the discharge reaches certain time, $t = \hat{t} \approx 0.55$ at which a free boundary develops.

Figure 2.11 shows the analytical solutions (2.122) of concentration in the solid c_{sc} before the development of free boundary. The figure shows that lithium intercalates into particles near the separator faster than in other parts of the electrode.

Figure 2.12 shows that for $t > \hat{t}$ free boundary propagates in from the separator. Figure 2.12(b) shows the profiles of the lithium ion concentration, c, in the electrolyte for times

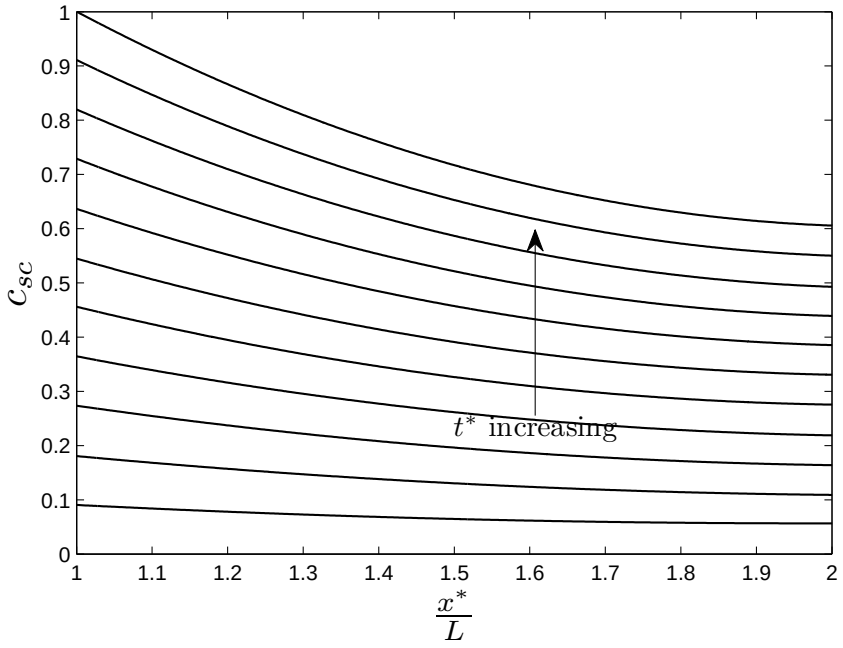

Figure 2.11: Lithium ion concentration distribution in the solid particles by equation (2.122) at $\bar{I} = 1$. The profiles are measured at $t = 0.05, 0.1, 0.15, 0.2, ...$ At certain time ($t = \hat{t}$), the concentration in the solid reaches maximum ($c_{sc} = 1$) in region near separator and at later time ($t > \hat{t}$), free boundary develops. Here $\hat{t} = 0.55$

$t > \hat{t}$. In the region $x < s(t)$, c has a linear profile. While for $x > s(t)$ the particles are still absorbing lithium ions. As the discharge proceeds, the movement of the free boundary across the electrode is clearly seen in this figure. At higher discharge rate, the intercalation rate near the separator is much faster than elsewhere (see Figure 2.13). After time $t = \hat{t}$, the c_{sc} reaches 1 in region near the separator and the surface reactions cease (i.e. $G_c = 0$).

At large discharge rates, a further boundary develops close to the current collector ($x = 1$) where the electrolyte becomes depleted as shown in Figure 2.13. The concentration in the electrolyte is driven to zero, (this is called the *limiting-current phenomenon*) [36]), this prevents from discharging further and so the intercalation reaction will cease here too. However, we do not investigate this further here.

2.8 Summary

A detailed model for a lithium ion battery based on dilute electrolyte theory and accounting for intercalation reactions on the surface of the electrode particles has been developed. Following [74], the homogenisation technique was used to derive macroscopic equations from a microscopic mocel. These macroscopic equations was then solved in a

whole cell and in a half cell cathode material. An asymptotic approximation was used to approximate the Butler Volmer equations with Tafel equations. Analytic solutions for the electrolyte concentration, c and electrolyte potential, $\tilde{\phi}$ were derived for whole cell system in a quasistatic regime for electrode materials with flat discharge curves.

In the half cell cathode, the system develops a free boundary problem dividing regions that have fully discharged from those which are only partially discharged. Analytic solutions for the electrolyte concentration, c and electrolyte potential ($\tilde{\phi}(x)$) were calculated; before and after the development of free boundary. At high discharge currents, the electrolyte concentration was also found to zero near the current collector, thereby preventing the solid particles to facilitate discharge. Hence, another free boundary develops in this region. However, we do not investigate this further here.

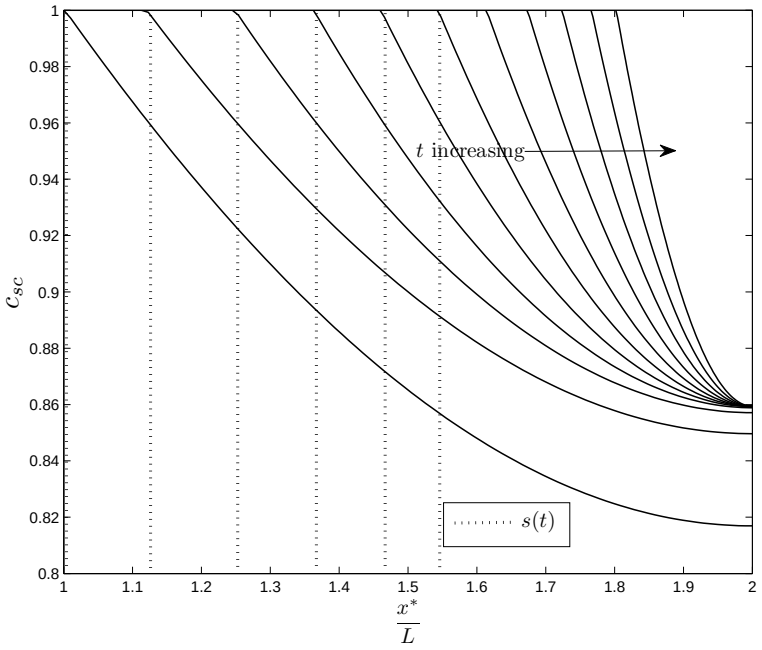

(a) Concentration of Lithium in the solid

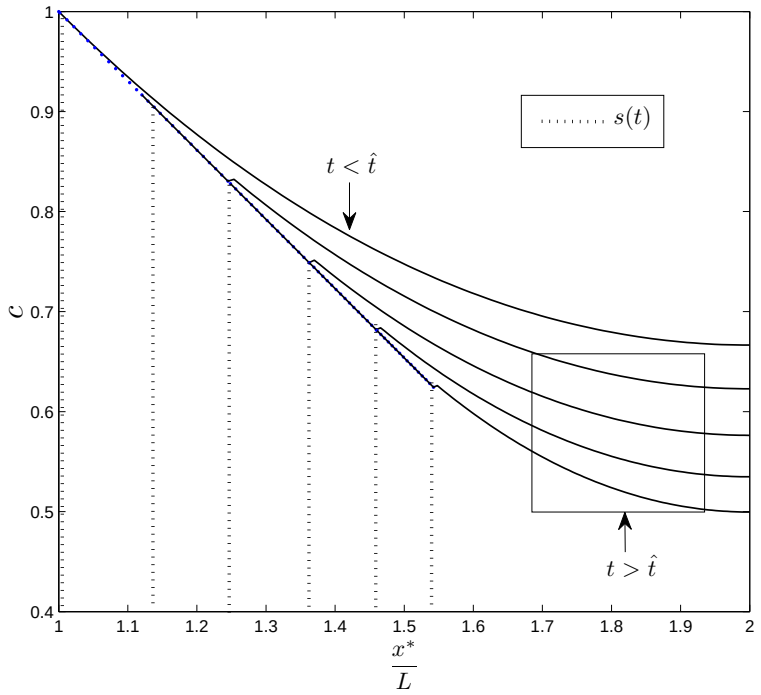

(b) Concentration of Lithium ions in the electrolyte

Figure 2.12: (a) Upper figure: the concentration of lithium in solid particles that reaches the maximum capacity at $x = s(t)$. The solubility rate of lithium no longer at the same rate at this point forward because of the concentration profiles of electrolyte. (b) Lower figure: The concentration profiles across the cell in comparison to the time before ($t < \hat{t}$) (by equation (2.119)) and after ($t > \hat{t}$) (by equation (2.132)) formation of free boundary. The profiles are discharged at $\bar{I} = 0.5$. The arrow shows the direction of increasing time and $\hat{t} = 0.64$.

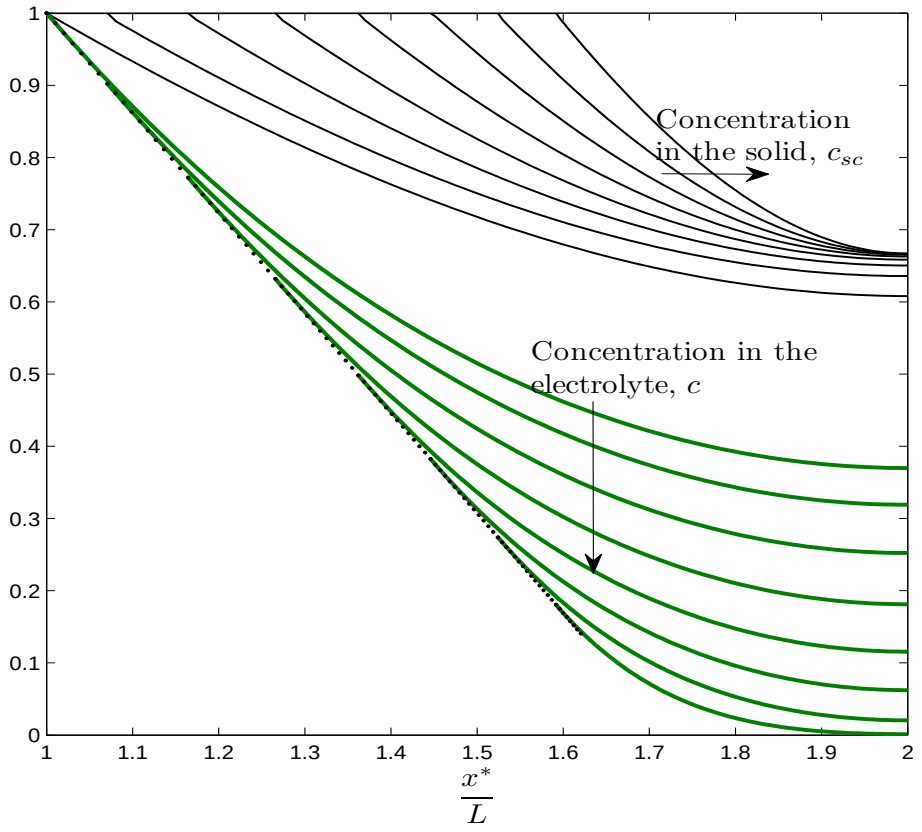

Figure 2.13: The concentration of Lithium in solid particles and Lithium ions electrolyte at $\bar{I} = 1$ discharge rate. The arrow shows the direction of time increases ($t = 0.55, 0.6, 0.65, ...$) and $\hat{t} = 0.55$.

Chapter 3

Modelling moderately concentrated electrolytes

3.1 Introduction

In this chapter we discuss a description of the transport equations in moderately concentrated electrolytes. This is the regime in which although the ionic concentration is low in comparison to that of the solvent, it is high enough so that significant interacting occur between the charged ions, this, in turn, lead to non-ideal behaviour of the electrolyte and in particular the conductivity. Newman has been the pioneer in developing mathematical models of batteries in concentrated electrolyte [59]. Models based on his approaches have been applied to a variety of systems by Newman and his co-workers with a degree of success. However, his approach has not been widely adopted outside his group [51] with the notable exceptions of; see [28, 30, 84, 23]. In order to rectify this we set out here to explain his approach while also highlighting theoretical difficulties.

In most battery systems, the electrolyte solutions are at sufficiently high concentration that they behave non-ideally as demonstrated primarily by the concentration dependence of the conductivity [90] but also from activity coefficient measurements [78] and studies of ion-pairing and aggregation process [103]. It is necessary to look at the behaviour of solutions in which not only ion/solvent interactions are significant but also ion/ion interactions. As they move in solution, ions tend to attract to oppositely charged ions and this reduces the ionic mobility since paired ions have zero net charge and consequently do not move in response to an electric field [78].

Typically the phenomenological moderately concentrated electrolyte theory presented here is appropriate for most electrolyte solutions but would not be appropriated for molten salts and ionic liquids. The theory is based on the three most readily measured experimental characterizations of an electrolyte as its concentration changes, namely

ionic diffusivity, transference number and ionic conductivity. We parametrize the model against experimental data for the most common lithium ion electrolyte $LiPF_6$ in 1:1 EC:DMC [90].

3.2 Stefan-Maxwell equations

The Stefan-Maxwell multicomponent diffusion equation has been used by Newman as the foundation of concentrated solution theory. The basic idea of this approach is that mass transfer is driven by the gradient of electrochemical potential of a species and limited by the friction with its surroundings. The balance of these two forces determines the speed with which a species moves. The mutual friction force between species i and j is assumed to be proportional to the friction forces arising from velocity differences between the species and is proportional to the mole fractions of the two species [8]. Let

$$\chi_i = \frac{c_i}{c_T}, \qquad \chi_j = \frac{c_j}{c_T} \tag{3.1}$$

be the mole fractions of ion species i and j, where c_T is the total molar concentration of all species in the electrolyte and c_i and c_j are the molar concentration of species i and j. The Stefan-Maxwell equation give a relation between $\mathbf{d}_i$, the drag force exerted on a mole of species i by all the other species, and the velocities of the various species. In light of the above discussions the drag force acting per mole of species i is (see [8])

$$\mathbf{d}_i = RT \sum_{j \neq i} k_{ij} \chi_i \chi_j (\mathbf{v}_j - \mathbf{v}_i). \tag{3.2}$$

Here $\mathbf{v}_i$ and $\mathbf{v}_j$ are the velocities of species i, j and $RTk_{ij}\chi_i\chi_j$ is the drag coefficient between species i and j. Note that by the Einsten relation the diffusivity, $D_{ij} = 1/k_{ij}$ where D_{ij} describes the pairwise frictional interactions of inter-species i and j. This drag force $\mathbf{d}_i$, is equal and opposite to the force (per unit mole) arising from the gradient of the electrochemical potential of the i'th species, μ_i, so that

$$\mathbf{d}_i = \chi_i \nabla \mu_i. \tag{3.3}$$

3.2.1 Chemical potential ($\bar{\mu}$) and electrochemical potential (μ) of the electrolyte at constant pressure and temperature

Chemical potential The chemical potential $\bar{\mu}_i$ is defined in terms of the Gibbs free energy G such that at constant pressure and temperature, the chemical potential of the i'th species is given by

$$\bar{\mu}_i = \frac{\partial G}{\partial c_i} \tag{3.4}$$

For an ideal solution [4], this takes the form

$$\bar{\mu}_i = \mu_i^0 + RT\log(\chi_i) \tag{3.5}$$

where μ_i^0 is standard state potential of species i and the second term gives the entropy of mixing with the other components in a mixture. However this relation is usually insufficient because of chemical interactions with other species (including the solvent) and so is usually replaced by

$$\bar{\mu}_i = \mu_i^0 + RT\log(a_i(\chi_i)) \tag{3.6}$$

where $a_i(\chi_i)$ is the activity coefficient; a quantity that contains the deviation from ideality. In order to generalise this concept to charged species in an electric field we need to introduce the idea of an electrochemical potential.

Electrochemical potential If the species is an ion of valency z_i the work per mole of ions is $z_i F\tilde{\phi}$ where F is Faraday's constant and $\tilde{\phi}$ is the local electric potential. The electrochemical potential includes contribution from electric potential and is related to the chemical potential (3.6) by

$$\mu_i = \bar{\mu}_i + z_i F\tilde{\phi} = \mu_i^0 + RT\log(a_i(\chi_i)) + z_i F\tilde{\phi} \tag{3.7}$$

(see [4]). However, this form is only true if $\tilde{\phi}$ is the true electric potential calculated from taking account of each ion individually. It is common to replace $\tilde{\phi}$, the true potential, by ϕ, the potential calculated from the average charge distribution of the ions. Whilst this is often a good approximation in dilute electrolytes it is not so good in more concentrated solutions where short range interionic forces can cause ion pairing for significant periods of time.

At phase equilibrium the total sum of the electrochemical potentials of all species is zero, as the free energy is at a minimum

$$\sum \mu_i = 0 \tag{3.8}$$

3.3 The Stefan Maxwell equations for the binary 1:1 electrolyte

Insertion of (3.3) and the Maxwell-Stefan diffusivity $D_{ij} = 1/k_{ij}$ into the Maxwell-Stefan equation (3.2) yields the multicomponent diffusion system [60]

$$-c_i\nabla\mu_i = \sum_i \mathcal{K}_{ij}(\mathbf{v}_i - \mathbf{v}_j) \tag{3.9}$$

where

$$\mathcal{K}_{ij} = RT\frac{c_i c_j}{c_T D_{ij}} \tag{3.10}$$

and D_{ij} is the diffusivity of species i in species j. For the sake of clarity we will only consider a binary 1:1 electrolyte (*i.e.* $z_+ = 1$ and $z_- = -1$). We denote the three species involved as the solvent, cation (P^+) and anion (N^-) by the subscript $i = w, p, n$; respectively. The expansion of (3.9) can then be written as

$$-p\nabla\mu_p = \mathcal{K}_{pn}(\mathbf{v}_p - \mathbf{v}_n) + \mathcal{K}_{pw}(\mathbf{v}_p - \mathbf{v}_w) \tag{3.11}$$

$$-n\nabla\mu_n = \mathcal{K}_{np}(\mathbf{v}_n - \mathbf{v}_p) + \mathcal{K}_{nw}(\mathbf{v}_n - \mathbf{v}_w) \tag{3.12}$$

$$-w\nabla\mu_w = \mathcal{K}_{wp}(\mathbf{v}_w - \mathbf{v}_p) + \mathcal{K}_{wn}(\mathbf{v}_w - \mathbf{v}_n) \tag{3.13}$$

where $c_1 = p, c_2 = n$ and $c_3 = w$ are the concentration of P^+, N^- and the solvent; respectively. By Newton's third law of motion, $\mathcal{K}_{ij} = \mathcal{K}_{ji}$. Addition of (3.11)-(3.13) then leads to the Gibbs-Duhem relation

$$\sum_i c_i \nabla\mu_i = 0 \tag{3.14}$$

$$w\nabla\mu_w + p\nabla\mu_p + n\nabla\mu_n = 0 \tag{3.15}$$

This relation tells us that the chemical potentials of a mixture cannot change independently. In a binary system, if the potential of one species increases than the potential of the other species must decrease.

Averaged approximation to Poisson's equation The electric potential $\tilde{\phi}$ for a given distribution of point charges q_i at position $\boldsymbol{X}_i$ obeys Poisson's equation

$$\nabla\cdot(\varepsilon\nabla\tilde{\phi}) = -\sum q_i\delta(\boldsymbol{X} - \boldsymbol{X}_i) \tag{3.16}$$

where δ is the Dirac delta function. In an electrolyte with molar concentrations p positive $+1$ ions and n negative -1 ions; an averaged approximation to the electric potential is given by

$$\nabla\cdot(\varepsilon\nabla\phi) = F(n - p) \tag{3.17}$$

Here, ϕ is the averaged potential and ε is the permittivity. A major concern in treating electrolytes properties using the electrochemical potential is to what extent is it reasonable to replace $\tilde{\phi}$ in (3.7) by ϕ as defined by (3.17). By doing so, we neglect the effects of short range 'pairing' interactions between ions.

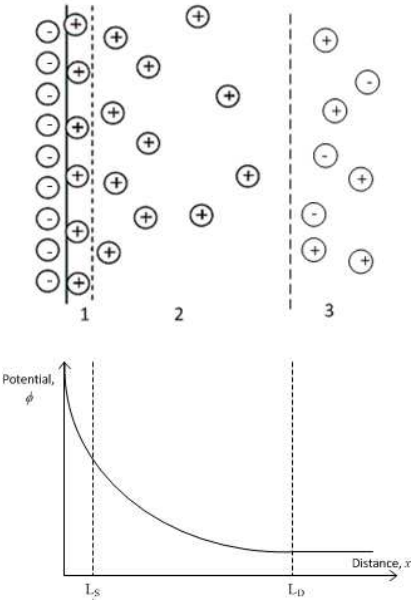

Figure 3.1: Structure of the electric double layer near a solid/electrolyte interface. When external electric field is applied, bulk motion of an electrolyte caused by Coulombic forces acting on ions in the electric double layer. The electric double layer, composed of a Stern layer(layer 1), Debye layer(layer 2) and bulk solution(layer 3). The bottom graph shows the difference of potential energy in each layer before the mobile ions extending into the bulk solution.

Non-dimensionalising Poisson's equation Non-dimensionalizing equation (3.17) by

$$\phi = \frac{RT}{F}\phi^*, \qquad p = C_0 p^*, \qquad n = C_0 n^*, \qquad x = Lx^* \tag{3.18}$$

we get

$$\nabla^2 \phi^* = \frac{1}{\lambda_D^2}(n^* - p^*) \tag{3.19}$$

where

$$\lambda_D = \frac{L_D}{L}, \qquad \text{and} \tag{3.20}$$

Here L_D describes the thickness of the double layer and is called the Debye length, L is the geometrical length scale and L_D is given by

$$L_D = \sqrt{\frac{\varepsilon RT}{F^2 C_0}}. \tag{3.21}$$

Debye region is the distance over which significant charge separation can occur. From Figure 3.1, we can see that the jump of potential drop in the Debye layer where the concentration of ions in which neutrality is not even approximately satisfied. In general

we don't see charge separation over a spatial distance more than a few Debye lengths. In typical electrolytes, the Debye length L_D is much smaller, at the nanoscale, so that double layers are typically thin compared to most geometrical length scales. For instance, for a solution with typical concentration of $1000 mol m^{-3}$, $L_D \approx 10^{-10} m$ and width $L = 10^{-3} m$, we find $\lambda_D \approx 5 \times 10^{-7}$ [6]. We shall thus consider in the limit $\lambda_D^2 \to 0$, (3.19) gives $p \approx n$ in the bulk of the cell. Hence, we can say that the electrode charge neutrality is almost satisfied, and this motivates us to write $p \approx c$ and $n \approx c$.

Charge neutrality For the above reasons it is usual to assume electroneutrality $n = p$ in the bulk of the electrolyte. Debye layers on the electrode are treated by the phenomenological Butler-Volmer conditions.

Equations for the current density j In what follows we broadly follow [60] but make their argument (which is often very hard to follow) more transparent. The total current density, $\mathbf{j}$ is the sum of the anodic and cathodic partial current density ($\mathbf{J}_n = -Fn\mathbf{v}_n, \mathbf{J}_p = Fp\mathbf{v}_p$), namely

$$\mathbf{j} = \mathbf{J}_p + \mathbf{J}_n = F(p\mathbf{v}_p - n\mathbf{v}_n) \tag{3.22}$$

By electroneutrality, and on denoting $c = p = n$, this can be written as

$$\mathbf{j} = Fc(\mathbf{v}_p - \mathbf{v}_n) \tag{3.23}$$

Substitution of (3.23) into (3.11) and (3.12) yields the system for cation and anion species

$$-c\nabla\mu_p = \mathcal{K}_{pw}(\mathbf{v}_p - \mathbf{v}_w) + \frac{\mathcal{K}_{pn}}{Fc}\mathbf{j} \tag{3.24}$$

$$-c\nabla\mu_n = \mathcal{K}_{nw}(\mathbf{v}_n - \mathbf{v}_w) - \frac{\mathcal{K}_{np}}{Fc}\mathbf{j} \tag{3.25}$$

where $\mathcal{K}_{ij}$ can be obtained from (3.10) as follows

$$\mathcal{K}_{pn} = \mathcal{K}_{np} = \frac{RTc^2}{c_T D_{pn}}; \qquad \mathcal{K}_{pw} = \frac{RTcw}{c_T D_{pw}}; \qquad \mathcal{K}_{nw} = \frac{RTcw}{c_T D_{nw}} \tag{3.26}$$

Rearranging (3.24) and (3.25), the ion velocities are found to be

$$\mathbf{v}_p = \mathbf{v}_w - \frac{c_T}{RT}\frac{D_{pw}}{w}\nabla\mu_p - \frac{D_{pw}}{D_{pn}wF}\mathbf{j} \tag{3.27}$$

$$\mathbf{v}_n = \mathbf{v}_w - \frac{c_T}{RT}\frac{D_{nw}}{w}\nabla\mu_n + \frac{D_{nw}}{D_{pn}wF}\mathbf{j} \tag{3.28}$$

Subtraction of (3.28) from (3.27) we obtain

$$\mathbf{v}_p - \mathbf{v}_n = \frac{c_T}{RTw}(D_{nw}\nabla\mu_n - D_{pw}\nabla\mu_p) - \frac{D_{pw}+D_{nw}}{FwD_{pn}}\mathbf{j} \tag{3.29}$$

Substituting for $\mathbf{v}_p - \mathbf{v}_n$ from (3.23) into (3.29) and rearranging yields an equation for current density in terms of electrochemical potentials

$$\mathbf{j} = \frac{Fc_T D_{pn} c}{RT(c(D_{pw}+D_{nw})+D_{pn}w)}\left(D_{nw}\nabla\mu_n - D_{pw}\nabla\mu_p\right) \tag{3.30}$$

where the electrochemical potential for the charged species μ_n and μ_p are defined by (3.7) such that

$$\mu_n = \mu_n^0 + RT\log(a_n) - F\tilde{\phi}, \qquad \mu_p = \mu_p^0 + RT\log(a_p) + F\tilde{\phi} \tag{3.31}$$

where a_n and a_p are (the concentration dependant) activity coefficients of the species N^- and P^+ in electrolyte. Notice that the definitions are in terms of the real electrostatic potential $\tilde{\phi}$ and not the averaged potential ϕ.

It is usual to define the transference numbers of cations (t_+^0) and anions (t_-^0) with respect to solvent velocity [4] by

$$t_+^0 = \frac{D_{pw}}{D_{pw}+D_{nw}}, \qquad t_-^0 = 1 - t_+^0 = \frac{D_{nw}}{D_{pw}+D_{nw}} \tag{3.32}$$

In an electrolyte, at a constant concentration different ions carry different fractions of the current because different ions move at different speeds under the same potential gradient. Here t_+^0 is the fraction of current carried by positive ions and t_-^0 is the fraction of current carried by negative ions.

Rearranging equation (3.30) to include the transference number (3.32), we obtain

$$\boldsymbol{j} = \frac{Fc_T D_{pn} c(D_{pw}+D_{nw})}{RT(c(D_{pw}+D_{nw})+D_{pn}w)}\left((1-t_+^0)\nabla\mu_n - t_+^0\nabla\mu_p\right) \tag{3.33}$$

Substituting (3.31) into (3.33) yields the equation of current density

$$\boldsymbol{j} = -\frac{F^2 c_T D_{pn} c(D_{pw}+D_{nw})}{RT(c(D_{pw}+D_{nw})+D_{pn}w)}\left(\nabla\tilde{\phi} + \frac{RT}{F}(t_+^0\nabla\log(a_p) - (1-t_+^0)\nabla\log(a_n))\right) \tag{3.34}$$

At constant concentration (c and w constant)

$$\boldsymbol{j} = -\frac{F^2 c_T D_{pn} c(D_{pw}+D_{nw})}{RT(c(D_{pw}+D_{nw})+D_{pn}w)}\nabla\tilde{\phi} = -\kappa(c)\nabla\tilde{\phi} \tag{3.35}$$

This version of Ohm's Law motivates the definition of the electrolyte conductivity $\kappa(c)$ by

$$\kappa(c) = \frac{c_T F^2 D_{pn}}{RT}\left(\frac{(D_{pw}+D_{nw})c}{D_{pn}w + (D_{pw}+D_{nw})c}\right) \tag{3.36}$$

Derivation of the ion velocities in terms of the electrolyte chemical potential μ_e and $\boldsymbol{j}$. Motivated by the final terms in (3.27) and (3.28) we seek an expression for $\frac{\boldsymbol{j}}{FD_{pn}w}$ writing it as

$$\frac{\boldsymbol{j}}{FD_{pn}w} = \frac{c(D_{pw}+D_{nw}) + wD_{pn}}{FD_{pn}wc(D_{pw}+D_{nw})}\boldsymbol{j} - \frac{\boldsymbol{j}}{Fc(D_{pw}+D_{nw})}. \tag{3.37}$$

If we now substitute for $\boldsymbol{j}$ from (3.30) in the first term on the right hand side of this expression we find

$$\frac{\boldsymbol{j}}{FD_{pn}w} = \frac{c_T}{RTw}\frac{(D_{nw}\nabla\mu_n - D_{pw}\nabla\mu_p)}{(D_{pw}+D_{nw})} - \frac{\boldsymbol{j}}{Fc(D_{pw}+D_{nw})} \tag{3.38}$$

Substituting this into (3.27) - (3.28), we obtain

$$\mathbf{v}_p = \mathbf{v}_w - \frac{c_T}{wRT}\frac{D_{nw}D_{pw}}{D_{pw}+D_{nw}}(\nabla\mu_p + \nabla\mu_n) + \frac{t_+^0}{Fc}\mathbf{j} \tag{3.39}$$

$$\mathbf{v}_n = \mathbf{v}_w - \frac{c_T}{wRT}\frac{D_{nw}D_{pw}}{D_{pw}+D_{nw}}(\nabla\mu_p + \nabla\mu_n) - \frac{(1-t_+^0)}{Fc}\mathbf{j} \tag{3.40}$$

These expressions can be simplified further on substituting for the chemical potential of the electrolyte μ_e and the chemical diffusion coefficient $\mathcal{D}$ which are defined by

$$\mu_e = \frac{\mu_n + \mu_p}{2}, \qquad \mathcal{D} = \frac{2D_{nw}D_{pw}}{D_{nw}+D_{pw}}; \tag{3.41}$$

this gives

$$\mathbf{v}_p = \mathbf{v}_w - \frac{c_T}{wRT}\mathcal{D}\nabla\mu_e + \frac{t_+^0}{Fc}\mathbf{j} \tag{3.42}$$

$$\mathbf{v}_n = \mathbf{v}_w - \frac{c_T}{wRT}\mathcal{D}\nabla\mu_e - \frac{(1-t_+^0)}{Fc}\mathbf{j} \tag{3.43}$$

Notably D_{nw} and D_{pw} can vary independently with concentration without affecting the proceeding analysis. It follows that $\mathcal{D}$ and t_+^0 may also be functions of concentration.

Diffusion equation for the electrolyte concentration By electroneutrality, the mass conservation of the ions in the electrolyte are written as

$$\frac{\partial c}{\partial t} + \nabla \cdot (c\mathbf{v}_p) = 0 \qquad \text{for the cations} \tag{3.44}$$

$$\frac{\partial c}{\partial t} + \nabla \cdot (c\mathbf{v}_n) = 0 \qquad \text{for the anions} \tag{3.45}$$

Taking the differences of these two equations gives

$$\nabla \cdot (c(\mathbf{v}_p - \mathbf{v}_n)) = 0 \tag{3.46}$$

which gives the current conservation equation. On substitution for $\boldsymbol{v}_p$ and $\boldsymbol{v}_n$ from (3.42)-(3.43) into (3.46) we obtain the current conservation condition

$$\nabla \cdot \mathbf{j} = 0. \tag{3.47}$$

Substitution for either $\boldsymbol{v}_p$, from (3.42), in (3.44) (or for $\boldsymbol{v}_n$, from (3.43), in (3.45)) yields

$$\frac{\partial c}{\partial t} + \nabla \cdot (c\mathbf{v}_w) = \nabla \cdot \left(\frac{c_T}{wRT} c\mathcal{D} \nabla \mu_e \right) - \frac{\nabla t_+^0 \cdot \boldsymbol{j}}{F}. \tag{3.48}$$

The resulting model of the electrolyte is closed by constitutive equations for the current density $\boldsymbol{j}$, namely (3.34), and one for the electrochemical potential μ_e, namely (3.41 a).

3.3.1 Summary of model for moderately concentrated electrolyte

The model has the form

$$\frac{\partial c}{\partial t} + \nabla \cdot (c\mathbf{v}_w) = \nabla \cdot (D(c)\nabla c) - \frac{\nabla t_+^0 \cdot \boldsymbol{j}}{F} \tag{3.49}$$

$$\nabla \cdot \boldsymbol{j} = 0 \tag{3.50}$$

where

$$\boldsymbol{j} = -\kappa(c) \left(\nabla \tilde{\phi} + \frac{RT}{F} \left((t_+^0 \nabla \log(a_p)) - (1 - t_+^0) \nabla \log(a_n) \right) \right) \tag{3.51}$$

The electrochemical potential for the electrolyte, μ_e, the transference number, t_+^0, the conductivity, $\kappa(c)$ and the effective diffusivity $D(c)$ are given by

$$\mu_e = \frac{\mu_n^0 + \mu_p^0}{2} + RT \log\left((a_n a_p)^{1/2}\right) \tag{3.52}$$

$$t_+^0 = \frac{D_{pw}}{D_{pw} + D_{nw}} \tag{3.53}$$

$$\kappa(c) = \frac{c_T F^2}{RT}(D_{pw} + D_{nw}) \left(\frac{c}{w + c\left(\frac{D_{pw}+D_{nw}}{D_{pn}}\right)} \right) \tag{3.54}$$

$$D(c) = \frac{2c_T c\mathcal{D}}{w}\left(\frac{a_n'}{a_n} + \frac{a_p'}{a_p}\right). \tag{3.55}$$

The conductivity, $\kappa(c)$ in (3.54) can also be written in terms of the transference number (3.53), the diffusion coefficient (3.41)

$$\kappa(c) = \left(\frac{F^2 c_T}{2RT}\right) \frac{\mathcal{D}}{(1-t_+^0)t_+^0} \left(\frac{c}{w + \left(\frac{D_{pw}+D_{nw}}{D_{pn}}\right) c} \right). \tag{3.56}$$

Note that we retrieve the dilute solution conductivity for $D_{pn} >> (D_{pw} + D_{nw})$ that is

$$\kappa(c) = \frac{c_T F^2 D_{pn}}{RT}(D_{pw} + D_{nw})c. \tag{3.57}$$

3.3.2 An ideal solution

The solution is said to be ideal if the activities are directly proportional to the concentrations so that

$$a_p(c) = \frac{c}{c_T}, \qquad a_n(c) = \frac{c}{c_T} \tag{3.58}$$

where c_T is the total molar concentration of all species including the solvent. Hence, the diffusion equation (3.49) and the current density equation (3.51) become

$$\frac{\partial c}{\partial t} + \nabla \cdot (c\mathbf{v}_w) = \nabla \cdot \left(\mathcal{D}\frac{c_T}{w}\nabla c\right) - \frac{\nabla t_+^0 \cdot \boldsymbol{j}}{F} \tag{3.59}$$

$$\nabla \cdot \boldsymbol{j} = 0 \qquad \text{where} \qquad \mathbf{j} = -\kappa(c)\left(\nabla\tilde{\phi} - \frac{RT}{F}(1-2t_+^0)\nabla\log(c)\right) \tag{3.60}$$

3.3.3 How might we deal with the electric potential

One possible way to relate the true electric potential, $\tilde{\phi}$ (that appears in the electrochemical potentials) to the averaged electric potential ϕ, which appears in the averaged

version of Poisson's equation

$$\nabla \cdot (\varepsilon \nabla \phi) = F(n - p) \tag{3.61}$$

is to write

$$\tilde{\phi} = g(c)\phi \tag{3.62}$$

where $g(c)$ gives the fraction of unpaired ions. It is important to realise that this is a phenomenological relationship. The reason for doing this is that it is only the unpaired ions that are affected by the electric field and thus contribute to electrical part of potentials of the negative ions (μ_n) and of the positive ions (μ_p). Thus from (3.31), μ_n and μ_p take the form

$$\mu_n = \mu_n^0 + RT\log(a_n) - Fg_n(c)\phi \tag{3.63}$$

$$\mu_p = \mu_p^0 + RT\log(a_p) + Fg_p(c)\phi \tag{3.64}$$

However, as we shall see, it is not necessary to do this in order to understand electrolytes. This is partly because the result of solving Poisson's equations (3.61) is the same whichever potential we use namely charge neutrality $n \approx p$ and partly because electric potentials in electrolytes are measured using reference electrodes.

3.3.4 The potential measured with respect to Lithium electrode

Note that the factor $(1 - 2t_+^0)$ appearing in (3.60) differs from that given in [59] which $(1 - t_+^0)$. This difference comes about because Newman defines the potential $\hat{\phi}$ with respect to a reference lithium electrode rather than using the true electrolyte potential, $\tilde{\phi}$. The calculation here is based on the work by Richardson [75]. Based on the reaction at the lithium electrode/electrolyte interface the chemical reaction has the form

$$Li^+ + e^- \rightleftharpoons Li(s) \tag{3.65}$$

where e^- is the electron and $Li(s)$ is the Lithium solid. Assuming the reference electrode draws very little current, it is in approximate thermodynamic equilibrium with the electrolyte, so that from (3.65) we have

$$\mu_p + \mu_{e^-} = \mu_{Li(s)} \tag{3.66}$$

where the electric potential of the electron is given by $\mu_{e^-} = -F\hat{\phi}$ and the potential of the solid Lithium $\mu_{Li(s)}$ is constant. By substituting this and μ_p from (3.31) into (3.66), we obtain a relation between the lithium electrode potential, $\hat{\phi}$ and the true electric

potential, $\tilde{\phi}$

$$\tilde{\phi} = \hat{\phi} - \frac{RT}{F}\log(a_p) + \frac{1}{F}(\mu_{Li(s)} - \mu_p^0). \tag{3.67}$$

On substitution for $\tilde{\phi}$ in (3.60), the current density equation in terms of lithium electrode potential can be written as

$$\boldsymbol{j} = -\kappa(c)\left(\nabla\hat{\phi} - \frac{RT}{F}(1-t_+^0)(\nabla\log(a_p) + \nabla\log(a_n))\right) \tag{3.68}$$

and hence

$$\boldsymbol{j} = -\kappa(c)\left(\nabla\hat{\phi} - \frac{2}{F}(1-t_+^0)\nabla\log(\mu_e)\right) \tag{3.69}$$

so that for an ideal solution

$$\boldsymbol{j} = -\kappa(c)\left(\nabla\hat{\phi} - \frac{2RT}{F}(1-t_+^0)\nabla\log(c)\right) \tag{3.70}$$

We remark that the current density equation in [59, 23, 50] is identical to the equation (3.70). However, we found out that some authors such as [28, 36] used an incorrect current density equation by neglecting the factor 2 in front of $(1 - t_+^0)$. Note that, in this particular electrolyte, we use (3.70) for the current density equation provided that the treatment for this electrolyte has been taken into account in the conductivity equation $\kappa(c)$ (see (3.54)).

Remarks We note that equations written in terms of the lithium electrode potential $\hat{\phi}$ are unaffected by ion pairing (since we write $\tilde{\phi} = g(c)\phi$ but then eliminate $\tilde{\phi}$ in favour of $\hat{\phi}$). We note that all experimental data are measured in terms of lithium electrode potentials. In particular the Butler-Volmer equations are calibrated using lithium electrode (and hence in term of the lithium potential $\hat{\phi}$).

3.4 Thermodynamic fitting to data

A lithium ion electrolyte can be fully characterized, in terms of the moderately concentrated solution model (3.49)-(3.54), by experimental measurements of transference number t_+^0 and ionic diffusivity $D(c)$ and conductivity $\kappa(c)$ as functions of concentration. These have been measured by Riemers *et al.* [90] for $LiPF_6$ in 1:1 E:DMC at $T = 293K$ for which it is found that transference number is constant $t_+^0 = 0.38$, and that the ionic diffusivity and conductivity can be accurately fitted to the following functions of the

concentration c (measured in $\mathrm{mol\,m^{-3}}$):

$$D(c) = 5.253 \times 10^{-10} \exp\left(-0.0003071c\right) m^2 s^{-1} \quad (3.71)$$

$$\kappa(c) = 10^{-4} c(5.2069096 - 0.002143628c + 2.34402 \times 10^{-7} c^2)^2 A V^{-1} m^{-1} \quad (3.72)$$

as shown in Figure 3.2 and Figure 3.3.

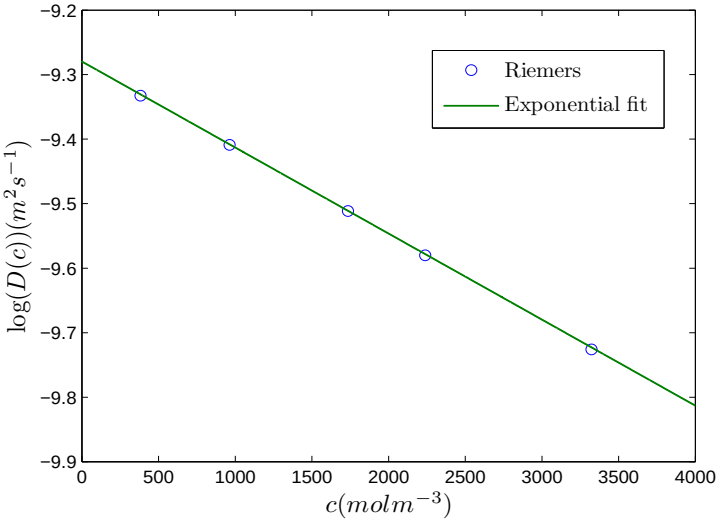

Figure 3.2: Diffusion coefficient as a function of concentration; line represents the fit to (3.71) and circles are the experimental data from Riemers [90].

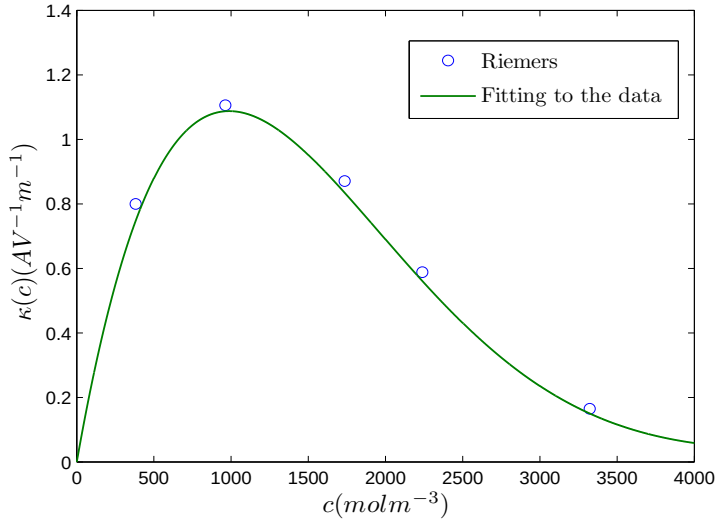

Figure 3.3: Concentration-dependent of electrolyte conductivity; line represents the fit to (3.72) and circles are the experimental data from Riemers [90].

It has been stated in the literature [59] that the maximum of electrolyte conductivity for electrolytes such as shown in Figure 3.2 is caused by the increasing viscosity as the

concentration increases. The thermodynamics fitting parameters present here are valid for $LiPF_6$ 1:1 EC:DMC liquid electrolyte at room temperature for which the transference number t_+^0 is found to be constant ($t_+^0 = 0.38$) . However, for some polymer electrolytes, the cationic transference number of this system has proved to be concentration-dependant, for instance, the dry polymer electrolyte studied by Doeff *et al.* [27] and the PEO-based electrolyte studied by Fauteux *et al.* [34], both have t_+^0 that varies with concentration. In spite of that, the three transport properties can be fitted to the resulting model by the relation (3.56).

3.5 Summary

Our approach consists in studying the transport of charged species in a moderately dilute electrolyte using drift diffusion models under the assumption of electroneutrality. The model discussed here is essentially the same as that given in [60]. We note the importance of the choice of potential. In particular if we choose to measure potential with respect to a lithium electrode this changes the factor appearing in front of the $\nabla \log(c)$ term in the equation for $\boldsymbol{j}$. The relation between these two potential definitions has been discussed. The crucial parameters such as the transference number, $t_+^0(c)$, the diffusion coefficient, $D(c)$ and ionic conductivity, $\kappa(c)$ are calculated from the experimental data and can be related to the three drag coefficient in the Stefan-Maxwell equations D_{pw}, D_{nw} and D_{pn} as functions of concentrations.

Chapter 4

Review of homogenisation technique for moderately concentrated electrolyte model

4.1 Introduction

Recent work has shown that performance of Lithium ion battery technology can be improved through emphasis on engineering the architecture of the electrode microstructure [41]. However, it is such a complex system to account for the exact micro-geometry at a scale of a full cell [93]. An approach based upon physical intuition has been adopted by Newman and co-workers [28, 36] to write the macroscopic model which the parameters in their macroscopic model are phenomenologically related to microstructure. The technique of averaging has been used by Wang *et al.* [92], however their resulting macroscopic model only restricted to constant transport parameters. A more successful approach is a multiple scales method, see for example, [19, 23, 74]. This method systematically relates a microscale electrolyte model with the microscopic geometry of the electrodes and the parameters in the macroscopic model are determined by the properties of microstructure.

Gully *et al.* [42] determined the effective transport coefficients for multiscale porous materials used in various electrochemical system by homogenisation approach. While homogenisation methods have resulted in the systematic derivation of macroscopic whole cell battery models (e.g. [23, 74, 19]), a systematic study to understand the relationship between the electrode microstructures and electrode performance has yet to be undertaken. David *et al.* use an ad-hoc approach by imaging sections of commercially porous electrode ($LiCoO_2$) using focused ion beam-scanning electron microscopy (FIB/SEM) and directly measure ionic pathways (permeability) and ion transport (conductivity) experimentally [86]. Similar work by Wilson et.al [96] has provided the three dimensional

microstructural data for the particles that have a highly irregular shape such as internal cracking.

We note that the length of the cell between current collectors is much smaller then the length of the other dimensions. The observation will, eventually, enable us to write down an approximate one dimensional averaged model for the battery. However, the microscale model of the battery, that we consider, must be genuinely three-dimensional.

4.2 The cell scale electrolyte equations by homogenisation technique

In this chapter we highlight the works by Richardson *et al.* [74] who derived the macroscale equations for dilute electrolyte using homogenisation technique and apply their results to the moderately concentrated electrolyte. The technique derives the macroscale electrolyte equations from a microscopic model. We have written down the moderately concentrated electrolyte equations in previous chapter which can then be applied directly to the microscale problem. The microscale problem is characterized by the Lithium ion concentration in the electrolyte, c, and the electric potential of the electrolyte, $\hat{\phi}$. The intercalation of Lithium ions from the electrolyte into the particles is represented by a surface reaction rate (per unit area) on the surface of the particles, G. At the microscale, a single representative electrode particle is examined. The microscale variables include the microscopic lithium concentration in the particle, c_s. The rate of diffusion in the particle and subsequent particle depends on the microscopic lithium transfer rate, G.

Here we briefly explain how the homogenisation is being considered. However, the details of derivation and calculation can be referred to the work by Richardson *et al.* [74]. The homogenisation is tackled using the asymptotic method of multiple scales and so should really non-dimensionalise the problem as a first step. In dimensionless units in which length has been scaled with cell width, the lengthscale of the microstructure is $\mathrm{O}(\delta)$ where $\delta << 1$ and that of the cell is $O(1)$. The homogenisation is accomplished by taking the limit $\delta \to 0$ (see e.g. [20]). Here Ω_{per} is the region occupied by the electrode particles and V_{per} is the region occupied by the electrolyte. We assume that the microstructure is locally periodic inside a completely periodic array of boxes, $V_{per} \cup \Omega_{per}$, thus allowing the microstructure to vary slowly, over the O(1) lengthscale. Figure 4.1 shows one of the periodic units that comprise the microstructure. A surface reaction occurs on the solid electrolyte interface, $\partial\Omega_{per}$ with rate (per unit area), G.

Boundary conditions on the surface of the electrode particles Concentration of lithium ions c^* and current density $\boldsymbol{j}^*$ equations, within the electrolyte, are described by (3.49) and (3.70), respectively. On the electrode particles surface, reactions taking

place give rise to a flux of Li^+ ions (but none of the N^- ions). Hence the boundary conditions on the surface of the electrode particles (on $\partial\Omega_{per}$) are given by

$$\begin{aligned} \boldsymbol{q}_p^* \cdot \boldsymbol{n}|_{\partial\Omega_{per}} &= G^*, \qquad \boldsymbol{q}_p^* = -D_p\left(\nabla p + \frac{Fp}{RT}\nabla\hat{\phi}^*\right) && (4.1)\\ \boldsymbol{q}_n^* \cdot \boldsymbol{n}|_{\partial\Omega_{per}} &= 0, \qquad \boldsymbol{q}_n^* = -D_n\left(\nabla n - \frac{Fn}{RT}\nabla\hat{\phi}^*\right) && (4.2)\\ \boldsymbol{j}^* \cdot \boldsymbol{n}|_{\partial\Omega_{per}} &= FG^*. && (4.3) \end{aligned}$$

where $\boldsymbol{n}$ is unit vector normal to the surface, p, n are the concentration of Li^+ and N^-, respectively, $\boldsymbol{q}_p^*, \boldsymbol{q}_n^*$ are the ion fluxes of the two ion species. The parameters D_p, D_n are the diffusion coefficients of species p and n, respectively. Here G^* is the reaction rate of the Lithium at the surface and is so-called Butler Volmer condition.

We note further that the total ionic flux may be written in terms of the ionic transference number as follows:

$$\boldsymbol{q}^* = \frac{D_n\boldsymbol{q}_p^* + D_p\boldsymbol{q}_n^*}{(D_n + D_p)} = (1 - t_+^0)\boldsymbol{q}_p^* - t_+^0\boldsymbol{q}_n^*. \tag{4.4}$$

where t_+^0 is given by (3.53).

General set of microscale electrolyte equations. The electrolyte model (Newman's type of battery model) with constant transference number and constant concentration of solvent has the form (see (3.49) and (3.70))

$$\begin{aligned} \frac{\partial c^*}{\partial t^*} + \nabla\cdot\boldsymbol{q}^* &= 0, \qquad \boldsymbol{q}^* = -D^*(c^*)\nabla c^* && (4.5)\\ \nabla\cdot\boldsymbol{j}^* &= 0 \qquad \mathbf{j}^* = -\kappa^*(c^*)\left(\nabla\hat{\phi}^* - 2\frac{RT}{F}(1 - t_+^0)\nabla\log(c^*)\right) && (4.6) \end{aligned}$$

On reference to (4.4), the boundary conditions (4.1)-(4.3) can be rewritten in terms of Lithium ion flux $\boldsymbol{q}$ as boundary conditions on (4.5) - (4.6) [75]

$$\boldsymbol{n}\cdot\boldsymbol{q}^* = (1 - t_+^0)G^*, \quad \boldsymbol{n}\cdot\boldsymbol{j}^* = FG^* \qquad \text{on} \quad \partial\Omega_{per} \tag{4.7}$$

For conservation of intercalated Lithium (c_s^*) at the particle surface is given by

$$\boldsymbol{n}\cdot\boldsymbol{q}_s^* = G^* \qquad \text{on} \quad \partial\Omega_{per} \tag{4.8}$$

Note that the asterisk is appended into the equations to denote that it is dimensional.

We now non-dimensionalise (4.5) - (4.6) as follows:

$$\begin{aligned} \boldsymbol{x}^* = L\boldsymbol{x}, \qquad t^* = \tau t, \qquad c^* = c_0 c, \quad \boldsymbol{j}^* = J\boldsymbol{j}, \quad D^* = D_0 D, \\ G^* = \frac{J}{b_{et}LF}G, \quad \boldsymbol{q}^* = \frac{J}{b_{et}LF}\boldsymbol{q}, \quad \boldsymbol{q}_s^* = \frac{J}{F}\boldsymbol{q}_s, \quad \kappa^* = K\kappa \quad \hat{\phi}^* = \Phi\hat{\phi}. \end{aligned} \tag{4.9}$$

Here, c_0 is the typical concentration of lithium ions in the electrolyte, Φ is the typical potential drop across the cell, D_0 is a typical diffusivity in the electrolyte and b_{et} is the typical active surface area density (surface area per unit volume) of electrode particles. τ is the typical timescale for discharge of the cell and is given by

$$\tau = \frac{Fc_0L}{J} \tag{4.10}$$

The non-dimensionalisation leads to a general set of electrolyte equations for an electrolyte with constant transference number [75], namely

$$\frac{\partial c}{\partial t} + \nabla \cdot \boldsymbol{q} = 0 \quad \text{where} \quad \boldsymbol{q} = -D(c)\nabla c \quad \text{in} \quad \mathrm{V}_{per}, \tag{4.11}$$

$$\boldsymbol{q} \cdot \boldsymbol{n}|_{\partial\Omega_{per}} = g_1(1 - t_+^0)G(c, \hat{\phi}), \tag{4.12}$$

$$\nabla \cdot \boldsymbol{j} = 0 \qquad \text{where} \quad \boldsymbol{j} = -\kappa(c)(\lambda\nabla\hat{\phi} - 2(1 - t_+^0)\nabla\log(c)) \quad \text{in} \quad \mathrm{V}_{per}, \tag{4.13}$$

$$\boldsymbol{j} \cdot \boldsymbol{n}|_{\partial\Omega_{per}} = g_2 G(c, \hat{\phi}), \tag{4.14}$$

where the parameters are defined as follows

$$\delta = \frac{1}{b_{et}L}, \qquad g_1 = \frac{JL\delta}{FD_0c_0}, \qquad g_2 = \frac{JLF\delta}{KRT}, \qquad \lambda = \frac{F\Phi}{RT}. \tag{4.15}$$

Here the size of δ is about 10^{-2} by considering the electrode particles are all spheres of radius a [74]. In Figure 4.1, δ measures the size of the periodic domain $V_{per} \cup \Omega_{per}$ and the microscale variable is defined by

$$\boldsymbol{x} = \delta\hat{\boldsymbol{x}} \tag{4.16}$$

where $\hat{\boldsymbol{x}}$ is the lengthscale of an electrode particle and $\boldsymbol{x}$ is the lengthscale of the thickness of the electrode.

The asymptotic expansions. In order to look at the behaviour of each variable we shall write the asymptotic expansions of the variables in [74, 75]. The expansions of

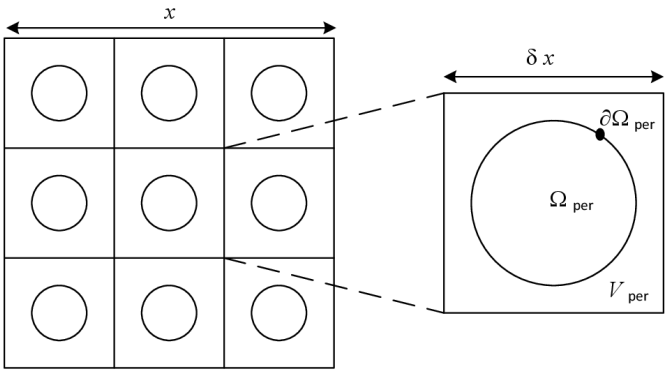

Figure 4.1: Illustration of the microstructured boundary

c, $\hat{\phi}$, $\boldsymbol{q}$ and $\boldsymbol{j}$ in powers of δ are as follows:

$$\begin{aligned} c &= c_0(\boldsymbol{x},t) + \delta c_1(\hat{\boldsymbol{x}},\boldsymbol{x},t) + \delta^2 c_2(\hat{\boldsymbol{x}},\boldsymbol{x},t) + \cdots, \\ \hat{\phi} &= \hat{\phi}_0(\boldsymbol{x},t) + \delta\hat{\phi}_1(\hat{\boldsymbol{x}},\boldsymbol{x},t) + \delta^2\hat{\phi}_2(\hat{\boldsymbol{x}},\boldsymbol{x},t) + \cdots, \\ \boldsymbol{q} &= \boldsymbol{q}_0(\hat{\boldsymbol{x}},\boldsymbol{x},t) + \delta\boldsymbol{q}_1(\hat{\boldsymbol{x}},\boldsymbol{x},t) + \delta^2\boldsymbol{q}_2(\hat{\boldsymbol{x}},\boldsymbol{x},t) + \cdots, \\ \boldsymbol{j} &= \boldsymbol{j}_0(\hat{\boldsymbol{x}},\boldsymbol{x},t) + \delta\boldsymbol{j}_1(\hat{\boldsymbol{x}},\boldsymbol{x},t) + \delta^2\boldsymbol{j}_2(\hat{\boldsymbol{x}},\boldsymbol{x},t) + \cdots. \end{aligned}$$

We note that the lithium ion concentration and the electrolyte potential are largely controlled by changes on the cell lengthscale with small changes on the particle lengthscale. The current density $\boldsymbol{j}$ and ion flux $\boldsymbol{q}$ shows significant changes on the particle lengthscale, i.e. are functions of $\hat{\boldsymbol{x}}$ at leading order. However the leading order for the lithium ion concentration and the electrolyte potential are $c_0(\boldsymbol{x},t)$ and $\hat{\phi}_0(\boldsymbol{x},t)$, respectively, depend only on the cell lengthscale $\boldsymbol{x}$ and time, and thus give a good approximation to the averaged quantities. This allows us to use the results of the homogenisation equations in [74] for the moderately concentrated electrolyte model. Such calculations using this technique for the model have been done by Richardson [75]. The resulting dimensionless equations are

$$\frac{|V_{\text{per}}|}{|V_{\text{per}}|+|\Omega_{\text{per}}|}\frac{\partial c_0}{\partial t} = \frac{\partial}{\partial x}\left(D(c_0)\mathcal{B}\frac{\partial c_0}{\partial x}\right) + g_1(1-t_+^0)G(c_0,\phi_0)\frac{\int_{\Omega_{\text{per}}} dS}{|V_{\text{per}}|+|\Omega_{\text{per}}|} \tag{4.17}$$

$$\frac{\partial j_0}{\partial x} = g_2 G(c_0,\phi_0)\frac{\int_{\Omega_{\text{per}}} dS}{|V_{\text{per}}|+|\Omega_{\text{per}}|}, \quad \text{where } j_0 = -\mathcal{B}\kappa(c_0)(\lambda\frac{\partial\hat{\phi}_0}{\partial x} - 2(1-t_+^0)\frac{\partial\log(c_0)}{\partial x}) \tag{4.18}$$

where $\mathcal{B}$ is the permeability tensor.

The solution to the moderately concentrated electrolyte model. The redimensionalisation (4.17) - (4.18) using (4.9) gives the macroscale electrolyte model (see [74, 75]) which is in the form

$$\epsilon_v \frac{\partial c^*}{\partial t^*} = \frac{\partial}{\partial x^*}\left(D(c^*)\mathcal{B}\frac{\partial c^*}{\partial x^*}\right) + (1-t_+^0) b_{et} G^*, \tag{4.19}$$

$$\frac{\partial j^*}{\partial x^*} = F b_{et} G^*, \quad \text{where} \quad j^* = -\mathcal{B}\kappa(c^*)\left(\frac{\partial \hat{\phi}^*}{\partial x^*} - \frac{2RT}{F}(1-t_+^0)\frac{\partial \log(c^*)}{\partial x^*}\right) \tag{4.20}$$

where ϵ_v is the volume fraction of the electrolyte as defined by

$$\epsilon_v = \frac{|V_{\text{per}}|}{|V_{\text{per}}| + |\Omega_{\text{per}}|}, \tag{4.21}$$

b_{et} is the B.E.T. surface area (*i.e.* the surface area of particles per unit volume of electrode) defined by

$$b_{et} = \frac{\int_{\Omega_{\text{per}}} dS}{|V_{\text{per}}| + |\Omega_{\text{per}}|}, \tag{4.22}$$

G^* is the reaction rate per unit surface area of electrode particle (typically given in terms of a Butler-Volmer equation) and $\mathcal{B}$ is the permeability tensor in x direction. The permeability tensor is found by solving a boundary value problem over a period of the microstructure (see equation (7.19) in [74]). Such a calculation has been done for various packing of spheres by Bruna [12].

4.3 Butler-Volmer reaction equations

4.3.1 The general version of Butler-Volmer equations for insertion material

The charge transfer at particle electrolyte interface depends upon the physical conditions, the intercalated lithium concentration on the electrode surface and the concentration of ions in the electrolyte is modelled by the phenomenological Butler-Volmer equation, which can apply to an elementary or a global reaction. The reaction at the solid/electrolyte interface has the form

$$Li^+ + e^- \rightleftharpoons Li_{(s)} \tag{4.23}$$

which represents the (de)intercalation of a Lithium ion in the electrolyte which combines with an electron form the electrode (left-hand side of equation) to give a an electrically neutral atom in the electrode particle (right-hand side of equation). Let k_a and k_c denote the forward and backward reaction rate constants, respectively, then corresponding

current fluxes are given by

$$\overrightarrow{i} = Fk_a c(c_{s,max} - c_s)^{\beta} \exp\left(-\alpha_a \frac{(F \triangle \phi + \triangle G_{chem}(c_s))}{RT}\right) \quad \text{forward reaction} \tag{4.24}$$

$$\overleftarrow{i} = Fk_c c_s \exp\left(\alpha_c \frac{(F \triangle \phi + \triangle G_{chem}(c_s))}{RT}\right) \quad \text{backward reaction} \tag{4.25}$$

respectively. Here c_s and c are the surface concentration of $Li_{(s)}$ on the electrode and the concentration of Li^+ in the electrolyte respectively; $c_{s,max}$ is the maximum concentration of lithium in the solid; $(c_{s,max} - c_s)$ is proportional to the surface density of available sites on the electrode surface for lithium intercalation; β is the vacancy factor of the electrode and depends upon the electrode material and $\triangle G_{chem}(c_s)$ is the chemical potential difference between a mole of lithium in the electrolyte and in the electrode. Here $\triangle \phi$ is the potential difference between the solid particle and the electrolyte (across the Debye layer) which is defined by

$$\triangle\phi = \hat{\phi}_s - \hat{\phi} \tag{4.26}$$

where $\hat{\phi}_s$ is potential of the electrode particle and $\hat{\phi}$ is that of the electrolyte. The symmetry factors α_a and α_c represent the fraction of the applied potential promoting the forward and backward reactions, respectively [7]. In the case of a simple one-electron transfer, $\alpha_c + \alpha_a = 1$. Hence, we can write $\alpha_a = \alpha$ and $\alpha_c = 1 - \alpha$. Usually $\alpha \approx 0.5$, as the anodic and cathodic current-voltage curves are nearly symmetrical [7]. At equilibrium, the two partial current densities (4.24)-(4.25) are equal in magnitude so that

$$\overrightarrow{i} = \overleftarrow{i} \tag{4.27}$$

It follows from this and (4.24)-(4.25) that the equilibrium potential difference $\triangle\hat{\phi}_{eq}$ satisfies

$$\begin{aligned} &Fk_a c(c_{s,max} - c_s)^{\beta} \exp\left(-\alpha \frac{(F \triangle \hat{\phi}_{eq} + \triangle G_{chem}(c_s))}{RT}\right) \\ &= Fk_c c_s \exp\left((1-\alpha) \frac{(F \triangle \hat{\phi}_{eq} + \triangle G_{chem}(c_s))}{RT}\right). \end{aligned} \tag{4.28}$$

which gives

$$\triangle\hat{\phi}_{eq} = \frac{RT}{F} \log\left(\frac{k_a c(c_{s,max} - c_s)^{\beta}}{k_c c_s}\right) - \frac{\triangle G_{chem}(c_s)}{F}. \tag{4.29}$$

The net current density (for the backward reaction) at the electrode particle surface is defined by $i = \overleftarrow{i} - \overrightarrow{i}$ and is hence given by the relation

$$\begin{aligned} i &= Fk_c c_s \exp\left((1-\alpha)\frac{(F\triangle\phi + \triangle G_{chem}(c_s))}{RT}\right) \\ &\quad -Fk_a c(c_{s,max}-c_s)^{\beta}\exp\left(-\alpha\frac{(F\triangle\phi + \triangle G_{chem}(c_s))}{RT}\right). \end{aligned} \tag{4.30}$$

The overpotential, η is the departure of the potential difference (between electrode particle and electrolyte) from its equilibrium value and is thus defined by

$$\eta = \hat{\phi} - \hat{\phi}_s + \triangle\hat{\phi}_{eq} \tag{4.31}$$

We note that $\triangle\hat{\phi}_{eq}(c, c_s)$ is an easily measured experimental quantity.

It follows that (4.30) can be written in the form

$$\begin{aligned} i &= Fk_c c_s \exp\left(-(1-\alpha)\frac{F(\eta - \triangle\hat{\phi}_{eq}) - \triangle G_{chem}(c_s)}{RT}\right) \\ &\quad -Fk_a c(c_{s,max}-c_s)^{\beta}\exp\left(\alpha\frac{F(\eta - \triangle\hat{\phi}_{eq}) - \triangle G_{chem}(c_s)}{RT}\right). \end{aligned} \tag{4.32}$$

Substituting for $\triangle\hat{\phi}_{eq}$ from (4.29) into (4.32) gives

$$\begin{aligned} i &= [F(k_c)^{\alpha}(k_a)^{(1-\alpha)}]c_s^{\alpha}c^{(1-\alpha)}(c_{s,max}-c_s)^{\beta(1-\alpha)} \\ &\quad \left(\exp\left(-(1-\alpha)\frac{F\eta}{RT}\right) - \exp\left(\alpha\frac{F\eta}{RT}\right)\right) \end{aligned} \tag{4.33}$$

or equivalently by

$$i = i_0(c, c_s)\left(\exp\left(-(1-\alpha)\frac{F\eta}{RT}\right) - \exp\left(\alpha\frac{F\eta}{RT}\right)\right) \tag{4.34}$$

where the exchange current density, $i_0(c, c_s)$ has the form

$$i_0(c, c_s) = [Fk_0](c_s)^{\alpha}(c)^{(1-\alpha)}(c_{s,max}-c_s)^{\beta(1-\alpha)}. \tag{4.35}$$

and k_0 is given by

$$k_0 = (k_c)^{\alpha}(k_a)^{(1-\alpha)}. \tag{4.36}$$

Equation (4.33) relates the rate of an electrochemical reaction on the surface of the particle in terms of the concentration of the reacting species and the potential difference between the electrolyte and the electrode [7]. If $\eta > 0$ (forward reaction), i is positive and electrons from the electrode bond to ions from the electrolyte to form lithium atoms in the electrode. If $\eta < 0$ (backward reaction), i is negative and lithium atoms

in the electrode dissociate into an electron and a lithium ion which is released into the electrolyte. The Butler-Volmer equation (4.33) describes the general electrochemical reaction that occurs when a solid metal is in contact with an ionic solution and the dependence of exchange current density on concentration is given by (4.35)-(4.36).

4.3.2 The Butler-Volmer equations of electrode materials for lithium battery

The (de)intercalation at the particle surface in the battery system depends upon the number of sites on the particle surface available for intercalation. Hence, it is necessary to take into account the dependence of the current density on the concentration of lithium on the surface of the electrode. In particular the reaction stops when there are no vacant sites on the surface for intercalation or when there are no lithium atom on the surface for deintercalation. Here we give some examples of Butler-Volmer equations for different electrode materials such as LiC_6, $LiFePO_4$ and $LiCoO_2$.

LiC_6 anode material The reaction of LiC_6 anode materials is given by

$$6\mathrm{C} + yLi^+ + ye^- \rightleftharpoons \mathrm{Li}_y\mathrm{C}_6. \tag{4.37}$$

Here x is proportional to the density of surface vacant sites. Depending on the level of intercalation of lithium ions in the graphite structure (4.37), y goes from 0 to 1 (which forward reactions limit up to $x = 1$). Thus, the Butler Volmer equations (4.33), can be rewritten (in which $\beta = 1$) in the form

$$i = F(k_c)^{\alpha}(k_a)^{(1-\alpha)}(c_s)^{\alpha}(c)^{(1-\alpha)}(c_{max} - c_s)^{(1-\alpha)}\left(\exp\left(-\alpha\frac{F\eta}{RT}\right) - \exp\left((1-\alpha)\frac{F\eta}{RT}\right)\right) \tag{4.38}$$

It can be rewritten as

$$i = i_0\left(\exp\left(-\alpha\frac{F\eta}{RT}\right) - \exp\left((1-\alpha)\frac{F\eta}{RT}\right)\right) \tag{4.39}$$

where the exchange current density, i_0 has the form

$$i_0 = Fk_0(c_s)^{\alpha}(c)^{(1-\alpha)}(c_{max} - c_s)^{(1-\alpha)}. \tag{4.40}$$

$LiFePO_4$ and $LiCoO_2$ cathode materials The reaction for $LiFePO_4$ and $LiCoO_2$ cathode materials is given by

$$\mathrm{Li}_{1-x}\mathrm{FePO}_4 + xLi^+ + xe^- \rightleftharpoons \mathrm{LiFePO}_4 \tag{4.41}$$

$$\mathrm{Li}_{1-x}\mathrm{CoO}_2 + xLi^+ + xe^- \rightleftharpoons \mathrm{LiCoO}_2 \tag{4.42}$$

respectively. Here the maximum level of reversible of the (de)intercalation of lithium in cathode electrodes (4.41)-(4.42) is limited by structural restrictions and corresponds to less than $x = 1$. Thus, the Butler Volmer equations (4.33), can be rewritten (in which $\beta = 1$) in the form

$$\begin{aligned} i &= F(k_c)^{\alpha}(k_a)^{(1-\alpha)}(c_s)^{\alpha}(c)^{1-\alpha)}(c_{max}-c_s)^{(1-\alpha)} \\ &\left(\exp\left(-\alpha\frac{F\eta}{RT}\right) - \exp\left((1-\alpha)\frac{F\eta}{RT}\right)\right) \end{aligned} \tag{4.43}$$

or equivalently

$$i = i_0\left(\exp\left(-\alpha\frac{F\eta}{RT}\right) - \exp\left((1-\alpha)\frac{F\eta}{RT}\right)\right) \tag{4.44}$$

where the exchange current density, i_0 has the form

$$i_0 = Fk_0(c_s)^{\alpha}(c)^{(1-\alpha)}(c_{max}-c_s)^{(1-\alpha)}. \tag{4.45}$$

In (4.43), the reaction rate approaches zero (switches off); when (i) the concentration of Lithium in the solid c_s approaches c_{max} for lithium insertion, (ii) c_s reaches zero for lithium extraction and (iii) the concentration in the electrolyte c is zero.

We denote the overpotential as

$$\eta = \hat{\phi} - \hat{\phi}_s - \hat{U}_{eq}(c_s|_{r=a_0}) \tag{4.46}$$

where $\hat{\phi}$ and $\hat{\phi}_s$ are the potential of electrolyte and solid particle with respect to Lithium electrode; respectively. $\hat{U}_{eq}(c_s|_{r=a_0})$ is the equilibrium potential of the electrode material as a function of the amount of lithium intercalated at the particle surface $(c_s|_{r=a_0})$ where a_0 is the radius of particle. The detail equations for the concentration and potential in the solid system is discussed in the Chapter 5.

4.4 Summary of the resulting model

The equations presented below constitute the general mathematical model of moderately concentrated solution (with the potential $\hat{\phi}$ is measured with respect to Lithium electrode). The numerical results obtain in the next chapter are based upon these equations with boundary conditions that change depending on the regime of battery that we are solving. The asterisk is appended into the equations to denote that it is dimensional.

The equations in the electrolyte (see (4.19)-(4.20)) are

$$\epsilon_v \frac{\partial c^*}{\partial t^*} = \frac{\partial}{\partial x^*}\left(D(c^*)\mathcal{B}\frac{\partial c^*}{\partial x^*}\right) - \frac{j^*}{F}\frac{\partial t_+^0}{\partial x^*} + (1-t_+^0)b_{et}G^*, \tag{4.47}$$

$$\frac{\partial j^*}{\partial x^*} = Fb_{et}^*G^*, \quad \text{where} \quad j^* = -\mathcal{B}\kappa(c^*)\left(\frac{\partial \hat{\phi}^*}{\partial x^*} - \frac{2RT}{F}(1-t_+^0)\frac{\partial \log(c^*)}{\partial x^*}\right). \tag{4.48}$$

In this study, the anode and cathode materials are chosen to be graphite (LiC_6) and Lithium iron phosphate ($LiFePO_4$), respectively. By taking $\alpha = 0.5$, the reaction rate equation for both material (see (4.38) and (4.43)) is

$$G^* = k_0(c^*)^{\frac{1}{2}}(c_s^*)^{\frac{1}{2}}(c_{max}^* - c_s^*)^{\frac{1}{2}}\left(\exp\left(-\frac{F\eta^*}{2RT}\right) - \exp\left(\frac{F\eta^*}{2RT}\right)\right) \tag{4.49}$$

where the overpotential, $\eta^* = \hat{\phi}^* - \hat{\phi}_s^* - U_{eq}^*(c_s^*|_{r^*=a_0})$.

Here G is a function of electrolyte concentration, solid concentration and the overpotential ($G^*(c^*, c_s^*|_{r^*=a_0}, \hat{\phi}^* - \hat{\phi}_s^*)$). Hence, these equations couple to transport equations for Lithium within the solid electrode particle. These will be discussed in Chapter 5.

4.4.1 Boundary conditions for the full cell battery

The full cell consists of the anode, separator (which is thin) and cathode which are sandwiched between two current collectors. Here $x^* = 0, L_a, L_c$ are the positions of the anode current collector, the separator and the cathode current collector, respectively. On the current collectors, there is no flux of Lithium ions, so that

$$\left.\frac{\partial c^*}{\partial x^*}\right|_{x^*=0} = 0, \qquad \left.\frac{\partial c^*}{\partial x^*}\right|_{x^*=L_c} = 0 \tag{4.50}$$

and in addition no current flows directly from the electrolyte into the current collectors, thus

$$j^*|_{x^*=0} = 0, \qquad j^*|_{x^*=L_c} = 0. \tag{4.51}$$

Assuming that the separator is extremely thin, the appropriate continuity conditions on $x^* = L_a$ are

$$[c^*]_{x^*=L_a} = 0, \qquad \left[\frac{\partial c^*}{\partial x^*}\right]_{x^*=L_a} = 0, \qquad [j^*]_{x^*=L_a} = 0, \qquad [\phi^*]_{x^*=L_a} = 0. \tag{4.52}$$

Lastly, the total surface reaction on all the anode particles is proportional to the applied current while that on the cathode particles is proportional to minus the applied current

$$Ab_{et_a}F\int_0^{L_a} G_a^*(\phi^*)dx^* = -Ab_{et_c}F\int_{L_a}^{L_c} G_c^*(\phi^*)dx^* = I^*. \tag{4.53}$$

where A is the area of the electrode, $b_{et,a}$ and $b_{et,c}$ are the BET surface area of anode and cathode , respectively and I^* is the total current flowing through cell.

4.5 Summary

This chapter reviews the derivation of the type of macroscopic model used by Newman and co-workers to investigate battery performance [29, 28, 23, 25]. The homogenisation technique has been successfully used in deriving the macroscale dilute electrolyte model [74]. Here, it is extended to moderately concentrated electrolyte model. It started from a model on the scale of the electrode particles used homogenisation technique to derive the macroscopic model [74, 19]. Such calculations using this technique for the model have been done by Richardson [75]. It is notable that using this technique, the permeability factor $\mathcal{B}$ can be calculated from the underlying microstructure. This enables us to derive the effective conductivity and an effective diffusion equation for the Lithium ion concentration within the electrolyte in terms of the properties of the microstructure.

The advantage of the homogenisation discussed here lies in the fact that the effective parameters in the Newman modelling framework can be derived directly from analysis of the microstructure. In addition we described Butler Volmer reaction kinetics for the intercalation reaction at the solid electrolyte interface. In what follows we will use the Butler Volmer equations (4.49) for the model simulation in Chapter 7 and Chapter 8.

Chapter 5

Models for electrode particles

5.1 Introduction

Lithium diffusion within electrode particles plays a crucial part in the behaviour of Lithium ion batteries. Phase transitions occur during intercalation of Lithium in the solid electrode. Typically, phase separation occurs between regions with different Lithium content (e.g. for olivine phosphate, regions between $FePO_4$ and $LiFePO_4$). Many electrode materials exhibit multiple phases with varying composition [35]. A popular cathode material, the olivine phosphates, exhibit two phases as reported by Goodenough [65, 18, 66], while the standard graphite (anode material), exhibits three or more phases [35]. However, the treatment of phase transformations pose a major modelling challenge. Furthermore, the dynamics of phase separation driven by electrochemical reaction is poorly understood. In this chapter, we present theories and summarize the experimental work on such phase transformations in some electrode materials.

5.2 Two phase Lithium insertion/extraction

Electrode material which perform a two phase transition during charge and discharge commonly exhibit flat discharge curve characteristic. Examples of such materials include lithium iron phosphate ($LiFePO_4$) and lithium titanate ($Li_4Ti_5O_{12}$) [76]; they are characterised by a wide potential plateau between the intercalated and deintercalated states.

The study of the two-phase system ($FePO_4$ to $LiFePO_4$) based on three dimensional shrinking core model was initially suggested by Padhi [65]. Subsequently the mathematical model was developed by Srinivasan and Newman [84]. The shrinking core model assumes a three-dimensional growth mechanism. Intercalated Lithium from the

outer surface of the spherical particle, causes phase separation into a core-shell structure. Recently, Farrell et. all [23] incorporated a shrinking core model into a battery model and used it to simulate the discharge of a $LiFePO_4$ cathodic material. Interesting result from the particle scale of the simulation is discussed in [23] and the model shows good agreement with the experimental data taken from Srinivasan and Newman [84]. The performance of $LiFePO_4$ can be increased by shrinking the sizes of the individual particles through which the diffusion of lithium takes place.

The second approach, the phase field modelling method, employs a phase field variable to describe a smooth transition from one phase to another. Phase field models are widely used to describe phase transformations in material science but are relatively new to electrochemistry [40]. This method has recently received growing attention particularly in the context of $LiFePO_4$ materials. Ferguson and Bazant [40] have developed a general phase field theory of ion intercalation kinetics. This theory is based on the Cahn-Hilliard model, and incorporates a heterogeneous charge-transfer reaction rate via a generalized Butler-Volmer equation [100]. The study has led to a better quantitative understanding of phase separation dynamics in $LiFePO_4$ nanoparticles.

Recent experimental evidence has pointed out that the lithium diffusion in $LiFePO_4$ is one-dimensional [2, 17, 3] occurring primarily along the b-axis of the crystal. Chen [17] has demonstrated that the $LiFePO_4/FePO_4$ interface moves perpendicular to the b-axis, consistent with rapid Lithium diffusion along that direction. The resulting evolution gives rise either to fully intercalated, or fully empty, $1D$ Lithium channels. This finding shows that the shrinking core model is not an accurate representation of the phase-change process.

Owen *et al.* [46] have observed that the solid state and interfacial processes can be neglected during fast discharge of $LiFePO_4$ composite electrode composed of very fine electrode particles (particle size $< 1\mu m$). They suggested that for thin electrodes containing large particles of active material the effect of particle size, i.e. solid state diffusion, becomes increasingly significant. Furthermore, Bazant *et al.* [40] have developed a general continuum theory for ion intercalation dynamics in a single crystal based on an existing phase field formulation of the bulk free energy and they found that the phase boundary extends from surface to surface along planes of fast ionic diffusion, consistent with recent experiments on $LiFePO_4$ [2]. It remains an open question what happens in real electrode particles composed of multiple crystals of $LiFePO_4$

5.2.1 "Shrinking-core" model

Newman and Srinivasan demonstrated the "shrinking core" path dependence phenomenon [84], and results from the mathematical model is compare reasonably well to their experimental discharge curve. In a spherical particle, "shrinking core" diffusion is modelled as a central sphere outside of which intercalated Lithium undergoes isotropic linear diffusion. This model assumes a growing shell of one phase surrounding a shrinking core of the other phase, with the shell and core phases determined by the direction of the net lithium flux.

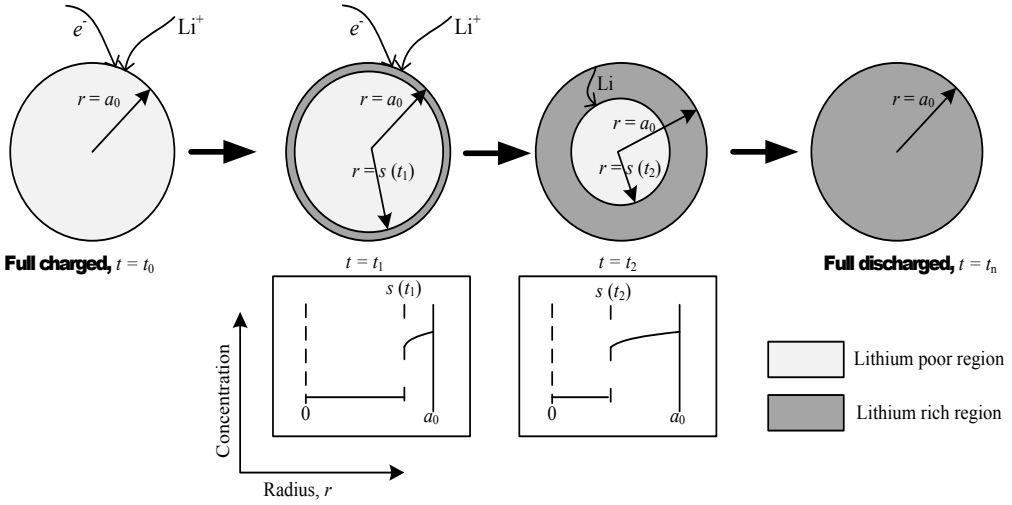

Figure 5.1: Illustration of the shrinking-core model with the side by side of the two phases and the movement of the phase boundary. The processes during discharge are illustrated and the pictures below showing concentration of Lithium as a function of r for different times. The dark region represents the Lithium-rich region and the bright region represents the Lithium-poor region.

As current is passed during discharge, an electrochemical reaction occurs at the surface of the particle in which lithium is intercalated and is then transported to the interior. Further insertion of Lithium forms a new phase that results in a shell of a Lithium-rich phase enclosing the Lithium-poor phase. As the electrode is discharged further, more Lithium is inserted and transported towards the particle centre which leads to a shrinking core phenomenon as depicted by Figure 5.1.

Fick's second law is use to describe the diffusion in the lithium-rich shell as

$$\frac{\partial c_s^*}{\partial t^*} = D_{Li}\frac{\partial^2 c_s^*}{\partial r^{*2}} + \frac{2D_{Li}}{r^*}\frac{\partial c_s^*}{\partial r^*}, \qquad s^*(t) < r^* < r_0 \tag{5.1}$$

where c_s^* is the concentration of the intercalated Lithium in the solid, D_{Li} is the diffusion coefficient of Lithium in the solid, t^* is time and r^* is the radial coordinate. Boundary

and initial conditions on the above problem are as follows

$$c_s^*|_{(t^*=0)} = c_{eq} \tag{5.2}$$

$$-D_{Li}\left.\frac{\partial c_s^*}{\partial r}\right|_{r^*=a_0} = G^* \tag{5.3}$$

where a_0 is the radius of the particle. The reaction current, G^* at the surface is given by a Butler Volmer equation. We note that, for the Lithium to be inserted into the particles, G^* has to be negative and $G^* = 0$ when c_s reaches c_{max} (c_{max} is the maximum lithium concentration in the electrode material). The position of the unknown interface $r^* = s^*(t^*)$ is evaluated from a mass balance condition at the interface, written as

$$c_s^*|_{r^*=s^*(t^*)} = c_{eq} \tag{5.4}$$

$$(c_{eq} - c_0)\frac{ds^*(t^*)}{dt^*} = -D_{Li}\left.\frac{\partial c_s^*}{\partial r^*}\right|_{r^*=s^*(t^*)}. \tag{5.5}$$

Here c_{eq} is the concentration at the interface in the Lithium-rich phase, while c_0 is the concentration throughout the lithium poor phase so that

$$c_s^* = c_0, \qquad \text{for} \qquad r^* < s^*(t^*) \tag{5.6}$$

where $c_0 = 0.02c_{max}$ is the concentration of the Lithium-poor phase [84].

When the core is consumed, then the whole electrode is uniformly in one phase, thus the boundary condition (5.5) is replaced by

$$D_{Li}\left.\frac{\partial c_s^*}{\partial r^*}\right|_{r^*=0} = 0 \tag{5.7}$$

We note that the problem described above is for battery discharge. As the battery is charged we might expect a similar free boundary problem, however it is not clear whether the free boundary will be stable.

Nondimensionalisation We non-dimensionalize the above system as follows:

$$r^* = a_0 r, \quad c_s^* = c_{eq} + (c_{max} - c_{eq})c_s, \quad s^* = a_0 s, \quad t^* = \tau t, \quad G^* = G_0 G \tag{5.8}$$

and choosing the time scale for the problem to be

$$\tau = \frac{c_{eq} - c_0}{c_{max} - c_{eq}}\frac{a_0^2}{D_{Li}}, \tag{5.9}$$

Thus the dimensionless problem of "shrinking core" diffusion model (5.1)-(5.7) is as follows

$$\frac{\partial c_s}{\partial t} = \Upsilon \frac{1}{r^2}\frac{\partial}{\partial r}\left(r^2 \frac{\partial c_s}{\partial r}\right), \tag{5.10}$$

$$\left.\frac{\partial c_s}{\partial r}\right|_{r=1} = \mathcal{Q}G, \qquad \left.\frac{\partial c_s}{\partial r}\right|_{r=0} = 0, \tag{5.11}$$

$$c_s|_{r=s(t)} = 0, \tag{5.12}$$

$$\frac{ds}{dt} = -\left.\frac{\partial c_s}{\partial r}\right|_{r=s(t)} \tag{5.13}$$

$$c_s|_{t=0} = 0. \tag{5.14}$$

with

$$c_s = -\Upsilon, \qquad \text{if} \qquad r < s(t). \tag{5.15}$$

The dimensionless parameters $\mathcal{Q}$ and Υ are defined by

$$\mathcal{Q} = \frac{a_0 G_0}{(c_{max} - c_{eq})D_{Li}} \quad \Upsilon = \frac{c_{eq} - c_0}{c_{max} - c_{eq}}. \tag{5.16}$$

The parameters used in the model are listed in Table 5.1. The reaction rate switches off when c_s reaches 1 which motivates us to write

$$G = \begin{cases} G_1, & \text{if} \quad c_s < 1 \\ 0, & \text{if} \quad c_s = 1. \end{cases} \tag{5.17}$$

where G_1 is constant. The electrode variables for $LiFePO_4$ electrode are listed in Table 5.1. Based on those values, the size dimensionless parameter Υ is $\Upsilon \approx 20$. We note that, Q depends upon the typical reaction rate G_0 which varies at different discharge currents. For example, if the cell is discharged at $1C$ discharge current ($I = 13Am^{-2}$), the typical reaction rate is $G_0 \approx 3 \times 10^{-7}$ which gives $Q \approx 0.4$, and at $5C$ discharge rate, $Q \approx 2$. Thus, the size of Q can be fairly approximated to be $O(1)$.

Parameter	Value	Units	Reference
Radius of particle, a_0	5×10^{-7}	m	[84]
Maximum concentration in $LiFePO_4$, c_{max}	20950	$molm^{-3}$	[23]
Concentration of the Lithium-rich phase, c_{eq}	$0.9525c_{max}$	$molm^{-3}$	[23]
Concentration of the Lithium-poor phase, c_0	$0.02c_{max}$	$molm^{-3}$	[23]
Lithium diffusivity, D_{Li}	8×10^{-18}	m^2s^{-1}	[84]

Table 5.1: Parameter values used in the model.

5.2.1.1 Solution Procedure

The moving boundary problem is solved using the Landau transformation [84] to make the coordinates fixed by substituting

$$\chi = \frac{r - s(t)}{1 - s(t)} \tag{5.18}$$

into (5.10)-(5.13). Therefore, we obtain the conservative form of c_s across a fixed domain $(0 \leq s(t) \leq 1)$ as the following

$$\begin{aligned}[\chi(1-s(t))+s(t)](\chi-1)(1-s(t))\frac{\partial c_s}{\partial \chi}\frac{ds}{dt} + [\chi(1-s(t))+s(t)](1-s(t))^2\frac{\partial c_s}{\partial t} \\ = 2\Upsilon(1-s(t))\frac{\partial c_s}{\partial \chi} + [\chi(1-s(t))+s(t)]\frac{\partial^2 c_s}{\partial \chi^2}\end{aligned} \tag{5.19}$$

$$c_s = 0 \text{ at } t = 0 \tag{5.20}$$

$$c_s|_{\chi=0} = 0 \tag{5.21}$$

$$-\left.\frac{\partial c_s}{\partial \chi}\right|_{\chi=0} = (1-s(t))\frac{ds(t)}{dt} \tag{5.22}$$

$$\left.\frac{\partial c_s}{\partial \chi}\right|_{\chi=1} = (1-s(t))\mathcal{Q}G. \tag{5.23}$$

The porous electrode model is solved with spatial discretization along the r coordinate with finite difference technique. Note that the solution for (5.19)-(5.23) is for the region $s(t) < r < 1$. In order to plot the result within the r-coordinate (in which $0 < r < 1$) and to see the moving phase boundary, we rescale the solution as follows

$$\hat{c}_s = \left(\frac{c_{max} - c_{eq}}{c_{max}}c_s + \frac{c_{eq}}{c_{max}}\right) \tag{5.24}$$

which gives

$$\hat{c}_s = \begin{cases} 0.02, & \text{if} \quad 0 < r < s(t) \\ 0.9525, & \text{if} \quad r = s(t) \\ 0.9525 < \hat{c}_s \leq 1, & \text{if} \quad s(t) < r \leq s(t) \end{cases} \tag{5.25}$$

Here, $\hat{c}_s = 0.02$ is the dimensionless concentration in the Lithium-poor region ($r < s(t)$, $\hat{c}_s = 0.9525$ is the dimensionless concentration at the free boundary ($r = s(t)$) and $\hat{c}_s = 1$ is the dimensionless maximum concentration.

Figure 5.2 presents a sketch of the lithium ion concentration profiles inside a $LiFePO_4$ particle during discharge. The phase between Lithium rich $\hat{c}_s = 0.9525$ and Lithium poor $\hat{c}_s = 0.02$ are separated by a phase boundary which moves toward the center of a particle as the intercalation process proceeds which $r = s(t)$ is where the position of the

phase boundary and $s(t)$ is a function of the discharge time. Note that $s(0) = 1$ is the initial position of the phase boundary.

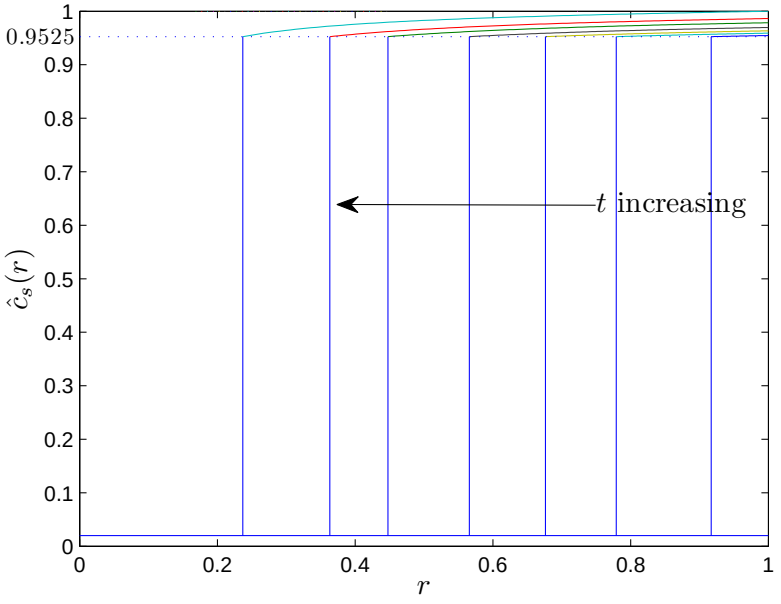

Figure 5.2: The lithium concentration profiles in solid particle during discharge where $\mathcal{Q} = 1$ and $\Upsilon = 20$. The vertical lines indicate the position of the phase boundary. When the surface concentration reaches 1, the reaction rate ceases hence stop the discharge. The times plotted are $t = 0.01, 0.02, 0.03, 0.04, 0.05, \cdots$.

5.2.1.2 Asymptotic solution of shrinking core diffusion

Here we look for an asymptotic solution to (5.10)-(5.13) with $\mathcal{Q} = O(1)$ and in the physically relevant limit $\Upsilon \gg 1$. Expanding in power of $1/\Upsilon$ as follows

$$c_s = c_{s0} + \frac{1}{\Upsilon} c_{s1} + ..., \qquad s(t) = s_0 + \frac{1}{\Upsilon} s_1 + ... \tag{5.26}$$

we obtain the following leading order problem

$$\frac{1}{r^2}\frac{\partial}{\partial r}\left(r^2 \frac{\partial c_{s0}}{\partial r}\right) = 0, \tag{5.27}$$

$$c_{s0}|_{r=s_0} = 0, \tag{5.28}$$

$$\left.\frac{\partial c_{s0}}{\partial r}\right|_{r=1} = \mathcal{Q}G, \tag{5.29}$$

$$\frac{ds_0}{dt} = -\left.\frac{\partial c_{s0}}{\partial r}\right|_{r=s_0}. \tag{5.30}$$

Solving the system (5.27) to (5.29) yields the solution

$$c_{s0} = \mathcal{Q}G\left(\frac{1}{s_0} - \frac{1}{r}\right) \tag{5.31}$$

Now we make use of the solution to solve (5.30) with initial condition $s_0(0) = 1$ gives us the free boundary behaviour which is

$$s_0 = (-3\mathcal{Q}Gt + 1)^{1/3} \tag{5.32}$$

At the next order $O(1/\Upsilon)$, the system is

$$\frac{\partial c_{s0}}{\partial t} = \frac{1}{r^2}\frac{\partial}{\partial r}\left(r^2\frac{\partial c_{s1}}{\partial r}\right), \tag{5.33}$$

$$c_{s1}|_{r=s_1} + s_1 \left.\frac{\partial c_{s0}}{\partial r}\right|_{r=s_0} = 0, \qquad \left.\frac{\partial c_{s1}}{\partial r}\right|_{r=1} = 0, \tag{5.34}$$

$$\frac{ds_1}{dt} = \left.\frac{\partial c_{s1}}{\partial r}\right|_{r=s_0} + s_1 \left.\frac{\partial^2 c_{s0}}{\partial r^2}\right|_{r=s_0}. \tag{5.35}$$

Substituting (5.31) into (5.33) with boundary conditions (5.34), we obtain the next order solution

$$c_{s1} = \frac{1}{3}\left(\frac{r^2}{2} + \frac{1}{r} - \frac{s_0^2}{2} - \frac{1}{s_0}\right)\frac{\mathcal{Q}^2G^2}{s_0^4} - s_1\frac{\mathcal{Q}G}{s_0^2} \tag{5.36}$$

The solution (5.36) leads us to find the next order solution of the free boundary interface (5.35) with $s_1(0) = 1$ which is

$$s_1 = \frac{s_0^2}{10}\left(\frac{(-1 + 5\mathcal{Q}Gt)\mathcal{Q}G}{s0^5} + \mathcal{Q}G\right) \tag{5.37}$$

Summary. In summary the solid concentration and the free boundary interface take the form

$$c_s = \mathcal{Q}G\left(\frac{1}{s_0} - \frac{1}{r}\right) + \frac{1}{\Upsilon}\frac{1}{3}\left(\frac{r^2}{2} + \frac{1}{r} - \frac{s_0^2}{2} - \frac{1}{s_0}\right)\frac{\mathcal{Q}^2G^2}{s_0^4} - s_1\frac{\mathcal{Q}G}{s_0^2} + O\left(\frac{1}{\Upsilon^2}\right), \tag{5.38}$$

$$s_0 = (-3\mathcal{Q}Gt + 1)^{1/3}, \qquad s_1 = \frac{s_0^2}{10}\left(\frac{(-1 + 5\mathcal{Q}Gt)\mathcal{Q}G}{s_0^5} + \mathcal{Q}G\right). \tag{5.39}$$

Figure 5.3 shows that the asymptotic with two term demonstrates a good agreement with the numerics except at later time, it underestimates the solution. From the equation above, we highlight that as the interface approaches zero then $1/s_0$ becomes a large number and the asymptotic solution breaks down.

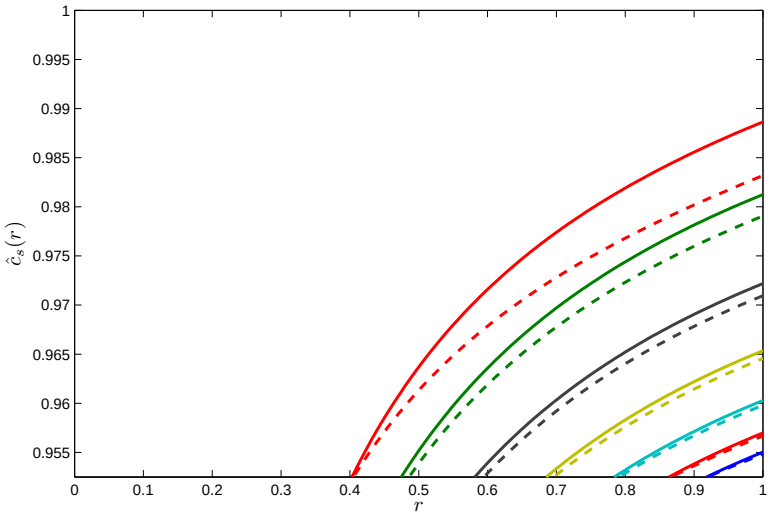

Figure 5.3: The comparison of lithium concentration profiles in solid particle during discharge ($\mathcal{Q} = 1$, $\Upsilon = 20$) between the numerics and asymptotic solutions (see (5.38)-(5.39)). The solid lines represent numerics, and dash lines represent asymptotic solutions.

5.2.2 Phase-field model

In recent years, other phase behaviour has been demonstrated experimentally [2, 26, 17] hence the "shrinking core" theory remains questionable. For example, Bazant *et al.* [40, 101] has predicted the phase behaviour theoretically using a Cahn-Hilliard phase-field model in isotropic nanoparticles with boundary condition for reaction kinetics based on local chemical potential differences and concentration gradient contributions [40]. They found that intercalation phase boundaries move along planes of fast ionic diffusion which agrees with the "domino cascade" model by Delmas *et al.* [26].

In 2011, Bai *et al.* [5] have extended the model for reaction limited intercalation in anisotropic nanoparticles. The phase separation is neglected in the y-direction ([010] direction) due to fast diffusion along this axis that causes the bulk concentration equilibrates quickly. Bai [5] proposed that phase separation could occur at low currents while at large currents, the particle fills homogeneously, hence suppress phase separation. Thus, the theory suggests that phase separation does not occur during normal battery operation which can be explained the high-rate capability of $LiFePO_4$. The transition from fully phase separation to no phase separation is captured in the simulation for filling at different currents are shown in Figure 5.4 . At low current, the phase separation is clearly appear and at slightly above the critical current, phase separation is hardly visible.

Further analysis has been done by Bazant *et al.* [63] in investigating the dynamics of interparticle mosaic instability in phase separating electrodes during discharge and charge. At low currents, the model assumes the nanoparticles (which have large surface area per volume ratios) fill preferentially, hence no phase separations occur within the individual nanoparticles. While at high current, the current density is more homogeneous throughout the electrode hence the phase separation is suppressed in individual particles. Furthermore, the diffusion time of lithium in the particles is much faster than the transport time of Lithium ions in the electrolyte. Hence, they used Fick's diffusion model for the transport of lithium in the particles.

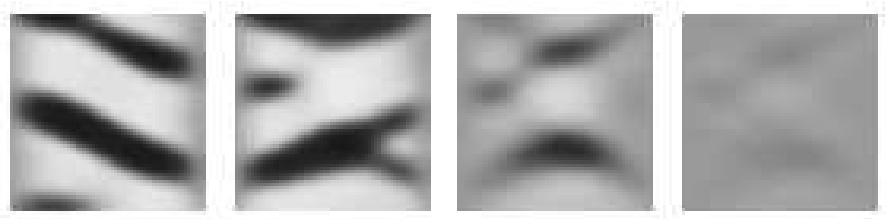

Figure 5.4: Phase boundary morphology that occurs between $FePO_4$ (black regions) and $LiFePO_4$ (grey regions) as discharge rate is increased. From left to right; (a) $\frac{I}{I_0}$=0.001, (b) $\frac{I}{I_0}$=0.01, (c) $\frac{I}{I_0}$=0.033, (d) $\frac{I}{I_0}$=0.05. Reprinted from [63].

Based on the above works, we came to the conclusion that when the particles of the electrode materials are sufficiently large, the particles tend to phase separate into their different stable phases generating interfaces, and that the "shrinking core" model may still provide an appropriate description. But for nanosized particles, phase separation is suppressed . In Chapter 8, we consider cathode composed of nanosized $LiFePO_4$ particles and note that since the diffusion timescales within the particles are small in comparison o those in the electrolyte the actual behaviour in the particles is unimportant. This motivates us to use a simple model for lithium transport in the electrode particles and incorporate this into a battery model in order to simulate the discharge curves in a $LiFePO_4$ half-cell.

5.3 More than two phases

Certain material exhibit multiple phases a common example being graphite [76, 35]. However, the diffusion of lithium in graphite (Li_xC_6) is not well understood and still under investigation, but some work has been done to model the diffusion and intercalation of lithium into the electrode material. Roscher has reported that graphite exhibits three or more phases (probably five) that can be inferred from several potential plateaus in the equilibrium potential curve of graphite [76]. Recently, Ferguson and Bazant [35] developed a predictive theory i.e a free energy model for three phases graphite. They

have approximated only the three phases at $x \approx 0$, $x \approx 1/2$, and $x \approx 1$, as x in $\mathrm{Li}_x\mathrm{C}_6$ varies from 0 to 1. The comparison between simulation and experiment shows a good agreement. To date, this is the only model that has demonstrated the diffusion in the solid material for more than two phase transformations. However when there are many phases a nonlinear diffusion model may actually provide a very good phenomenological description of the behaviour. This is demonstrated in Chapter 7 where we show good agreement to experimental discharge curves in a graphite half-cell using a lithium concentration dependent diffusivity.

5.4 Diffusion equation in the spherical coordinate

In this section the solid phase is assumed to comprise of identical spherical particles of a predetermined size and diffusion in the radial direction is assumed to be the predominant mode of transport. In $\mathrm{Li}_x\mathrm{C}_6$, we are motivated to neglect the phase transformations since no phase field model is able to adequately describe these phase transformations. Furthermore, it is common to model lithium transport in the electrode particles by diffusion equations (in fact typically linear diffusion) [37, 28, 72] especially for graphite. A generic diffusion model for lithium transport in a spherical electrode particles is

$$\frac{\partial c_s^*}{\partial t^*} = \frac{1}{r^{*2}} \frac{\partial}{\partial r^*} \left(r^{*2} D_s^*(c_s^*) \frac{\partial c_s^*}{\partial r^*} \right) \tag{5.40}$$

subject to the

$$\left. \frac{\partial c_s^*}{\partial r^*} \right|_{r^*=0} = 0, \qquad \left. -D_s^*(c_s^*) \frac{\partial c_s^*}{\partial r^*} \right|_{r^*=a} = G^*. \tag{5.41}$$

where the last condition specifies the lithium flux on the particle surface $r = a$ in terms of the reaction rate G.

Current density in the electrode We highlight that, in dilute electrolyte model, the potential in the electrode particles is taken to be constant (see Section 2.3) in assumption that the electronic conductivity in the electrode particles is large. However, in true battery behaviour this potential may varies across the length of the cell. In this section, we discuss the addition of this parameter into the model.

The total current density, j_{tot}^* is conserved in the two phases (electrolyte and electrode matrix phase) so that

$$j_{tot}^* = j^* + j_s^* \tag{5.42}$$

where j^* is the current density in the electrolyte and j_s^* is current density in the electrode matrix. The current flowing in the solid phase is usually modelled by Ohm's Law

$$j_s^* = -\sigma_s \frac{\partial \hat{\phi}_s^*}{\partial x^*} \tag{5.43}$$

where current conservation in the matrix is given by

$$\frac{\partial j_s^*}{\partial x^*} = -F b_{et} G^*. \tag{5.44}$$

Here σ_s is the conductivity of intercalated Lithium in the solid phase and $\hat{\phi}_s^*$ is the solid potential. These couple to particle equations that describe the concentration of lithium within single electrode particles at position x^* and the electrolyte equations (4.47)-(4.48). Note that (5.44) is to ensure that total current conservation $\frac{\partial \hat{j}_{tot}}{\partial x^*} = 0$ since $\frac{\partial j^*}{\partial x^*} = F b_{et} G^*$.

5.5 Summary

Electrode materials such as Li_yFePO_4 and Li_xC_6 exhibit phase transformations during the intercalation reactions at the solid phase. Phase transitions usually appear as plateaus in the open circuit potential of the materials as a function of lithium concentration in the material. The "shrinking core" model was initially considered the phase-separating mechanism in $LiFePO_4$ material. However, recently it has been demonstrated experimentally that the behaviour is not an accurate representation of the phase change in electrode nanoparticles. From experimental observation, the orientation of the moving phase boundary in $LiFePO_4$ crystal is one dimensional and the particle is most likely to be either fully intercalated or fully deintercalated. Furthermore, in nano-structured electrodes the intercalation reaction occurs predominantly at the particle surface, and can be approximated by fast diffusion in the solid where the particles are sufficiently small (refer to Chapter 8). Analysis of phase separation models leads to the conclusion that the phase transformation is extinguished [63] at the high reaction rates which occur in normal battery operation. Only at very small currents in large particles should phase separation play a major role.

For the Li_xC_6, up until now, there is no phase transition model that can adequately describe its multiple phase transitions. Therefore, it is usual to describe (de)intercalation of Lithium in the solid by a nonlinear diffusion equation (see Chapter 7). Previous works [see [37], [85],[72]] have been fitted to the experimental data assuming only linear diffusion in the electrode particle (although as we shall show this leads to disparities between the experimental data and the model).

Chapter 6

Numerical Procedure

6.1 Introduction

Modelling of battery systems involves the solution of complicated systems of equations that incorporate the electrochemical kinetics and the transport phenomena in the electrolyte and within the electrode particle. Analytical solutions in such system are available for several limiting cases. Doyle and Newman [31] obtained analytical solutions in the following cases: (i) when transport in the electrolyte phase is limiting (assumes constant diffusion coefficient in the electrolyte and fast diffusion in the solid phase); (ii) when diffusion in the solid phase is limiting (assumes the electrolyte concentration is uniform and the reaction occurs uniformly throughout the electrodes), and; (iii) when ohmic losses in the reaction zone dominate (assumes fast diffusion in the electrolyte and electrode particles). Darling and Newman [25] used Laplace transforms to obtain analytical solutions for the short time behaviour of a one-dimensional lithium ion cell. Doyle's [28] approach to describing the transport of lithium in the solid phase is to assume linear diffusion and to use the Duhamel's superposition integral [45] to obtain the solution.

Numerical methods are more flexible. The simplest, and most common, numerical approaches are based on finite difference approximations. For example, Newman's BAND subroutine which is written in FORTRAN [60] has been used for simulating batteries. It is a routine for solving a set of n coupled, linear, second order differential equations and is suitable for solving initial boundary value problems which are formulated as matrix equation using finite difference method [56]. White [94] provides an extension of the BAND subroutine for solving nonlinear finite difference equations. The inefficiencies of this subroutine is that the coefficient matrices have to be supplied to the subroutine every time BAND is called [9]. The battery model simulations in ([31], [25]) incorporate a single particle size with the same surface area across the electrode. However, these works by Newman and his co-workers ([31], [25]) use a finite number of particles which is not

self-consistent with the homogenisation averaging procedure used to derive electrolyte equations. In [85], Newman and Srinivasan use a two particle size distributions in order to achieve good comparison between their model and experiment. Recently, Farrell *et al.* [23] incorporate two particle sizes with constant diffusion in the solid in their three scales battery model simulation and discretised the system of equations using a finite volume method. They solved the resulting nonlinear system of differential-algebraic equations using an implicit differential-algebraic solver.

The system of partial differential equations, describing the evolution of: (i) concentration gradients of lithium ions in the electrolyte (c^*) ; (ii) the electrolyte potential (ϕ^*) (see (4.47)-(4.48)); (iii) the concentration of lithium ions in the solid (c_s^*) (see (5.40)-(5.41)), and; (iv) the solid potential ($\hat{\phi}_s^*$) (see (5.43)-(5.44)) in time and space are certainly not trivial to deal with even using numerical techniques. The main source of this difficulty is the coupling of the solid and electrolyte phases via the (de-)intercalation reaction rate equation, $G^*(c^*, \hat{\phi}^*\hat{\phi}_s^*, c_s^*)$, (see (4.49)). This reaction rate is applied on a continuum basis across each electrode, i.e. at each and every station in x (distance through the electrode) we assume that there is a representative particle in which lithium is transported by diffusion. This, combined with our assumption that the transport in each particle is radially symmetric, means that c_s^* has a $2D$ spatial dependency (i.e $c_s^* = c_s^*(x^*, r^*, t^*)$) where r^* is the radial position within a given particle. Thus, the complexity of the system increases when the number of stations in x (and hence the number of representative particles) increases.

Here, we elect to find approximate numerical solutions to the dimensionless systems (7.16)-(7.25), using the method of lines (MOL). In order to help the discussion of the method we shall assume here that the diffusion coefficient in the electrolyte $D(c)$, the conductivity $\kappa(c)$, and the diffusion of Lithium in the solid $D_s(c_s)$ are all constant. However, the same procedures can be applied to the more general model (7.16)-(7.25) with some relatively minor modification. The MOL methodology essentially converts a system of PDEs into a (large) coupled system of (in some sense equivalent) ODEs by approximating spatial derivatives using finite difference approximations. The resulting system of ODEs can then be evolved forward in time using standard ODE solvers. Note that the numerical techniques discussed in this chapter will be applied later in the thesis to the dimensionless half cell model of an anode (see Chapter 7) and a cathode (see Chapter 8). However, we stress that they can readily be adapted for use in other scenarios.

The resulting scheme provides a fast and numerically efficient of solving the model. The complete discharge simulation with $n = 100$ spatial points in x and r, is able to deal with internal boundary layers and runs in less than one minute. This scheme could for example fairly easily be generalised to ellipsoidal shaped particles or to particles whose size distribution depends upon x.

In §6.2, we demonstrate the MOL approach using the simple example of linear diffusion within a spherical particles. Then, in §6.3, we discuss some of the subtleties of applying the technique to our half cell model of an anode.

6.2 Method of Lines

The MOL is the central approach used in the numerical methods developed in this work. The power of this technique is that it allows one to decouple the spatial and temporal discretisation processes. It enables us to convert partial differential equations (PDEs) into a large set of ordinary differential equations (ODEs) that are approximate the PDEs. To demonstrate the MOL technique we consider the following example of the linear diffusion equation in a 'slab' geometry with an insulating boundary condition at $x = 0$ and a specified outward flux of u at $x = 1$. Initially the concentration of u is taken to be unity. We write

$$\frac{\partial u}{\partial t} = \frac{\partial^2 u}{\partial x^2} \tag{6.1}$$

with boundary conditions and initial condition

$$u|_{x=0} = 1, \qquad \left.\frac{\partial u}{\partial x}\right|_{x=1} = -1; \tag{6.2}$$

$$u|_{t=0} = 1. \tag{6.3}$$

First, we introduce a set of points in space, x_i for $i = 0, ..., n$, at which the spatial derivatives in equation (6.1) will be approximated using finite differences. For ease, we take this spatial grid to be uniform, i.e. we take $x_i = i \times \delta x$ where $\delta x = 1/n$. However, one could easily generalise to a non-uniform spatial grid if, for example, a higher spatial resolution is required in given parts of the spatial domain. We also introduce the following notation for the values of u at each of the points on the spatial grid: $u|_{x=x_i} = u_i$. The second order spatial derivative, at each points x_i, can then be approximated by the central difference

$$\left.\frac{\partial^2 u}{\partial x^2}\right|_{x=x_i} \approx \frac{u_{i+1} - 2u_i + u_{i-1}}{\delta x^2} \tag{6.4}$$

Employing this approximation at each of the points x_i converts the PDE (6.1) into the following set of n coupled ODEs

$$\frac{du_i}{dt} \approx \frac{u_{i+1} - 2u_i + u_{i-1}}{\delta x^2}, \qquad i = 1, 2, \cdots, n. \tag{6.5}$$

At both ends, we discretise the boundary conditions (6.2) as follows

$$\begin{aligned} u_1 &= 1, \qquad \text{at} \quad x = 0 \ (i = 1), \\ u_{n+1} &= u_{n-1} - 2\delta x, \qquad \text{at} \quad x = 1 \ (i = n). \end{aligned} \tag{6.6}$$

so that when we substitute the last into (6.5), with $i = n$, we can eliminate the fictitious point $n + 1$ to obtain

$$\frac{du_n}{dt} = \frac{2(u_{n-1} - u_n)}{\delta x^2} - \frac{2}{\delta x}. \tag{6.7}$$

The system of equation (6.5) can then be written in form

$$\frac{d}{dt}\begin{bmatrix} u_1 \\ u_2 \\ \vdots \\ u_{n-1} \\ u_n \end{bmatrix} = \frac{1}{\delta x^2}\begin{bmatrix} 1 & 0 & 0 & \cdots & \cdots \\ 1 & -2 & 1 & \cdots & \cdots \\ \vdots & \vdots & \ddots & \ddots & \vdots \\ \cdots & \cdots & 1 & -2 & 1 \\ \cdots & \cdots & \cdots & 2 & -2 \end{bmatrix}\begin{bmatrix} u_1 \\ u_2 \\ \vdots \\ u_{n-1} \\ u_n \end{bmatrix} + \frac{1}{\delta x}\begin{bmatrix} 0 \\ 0 \\ \vdots \\ 0 \\ -2 \end{bmatrix} \tag{6.8}$$

or more concisely as

$$\frac{\partial \boldsymbol{u}}{\partial t} = \boldsymbol{B}\boldsymbol{u} + \boldsymbol{g} \tag{6.9}$$

where $\boldsymbol{B}$ is the differentiation matrix and $\boldsymbol{g}$ is the source vector. This system can then be solved with an appropriate time integration method. In this work, the systems of ODEs arising from the MOL will be solved using an existing adaptive initial value problem solver, namely the Matlab routine ode15s.

6.3 Development of sparse matrix for the system

The dimensionless system (7.16)-(7.25) which we give in the next chapter is a coupled system of non-linear reaction-diffusion equations describing the discharge of a half cell anode. Note that in order to easily illustrate the method, we take the concentration dependant variables, $D(c), \kappa(c)$ and $D_s(c_s)$ in the system to be constant and equal to 1 and all the dimensionless parameters to be 1 but that a similar procedure can be applied to the real system with some minor modifications. The full system involves PDEs for diffusion in the solid (7.23)-(7.24) which has a 2D spatial dependacy; i.e. it is dependant on both x and r, where $0 \leq x \leq 1$ is the position through the electrode and $0 \leq r \leq 1$ is the radial position within a particle.

We begin by setting up n equally spaced grid points across the spatial variable x. At each of these stations in x we also consider a representative spherically symmetric solid particle which is discretised using m grid points in the radial position within the particle,

r. We introduce $\delta x = 1/n$ and $\delta r = 1/m$ so that our discretisation points are located at $x_i = i \times \delta x$ and $r_j = j \times \delta r$. At each of the $(n \times n)$ discretisation points spatial derivatives in the system (7.16)-(7.18) (or $(m \times m)$ in the system (7.23)) are approximated using the central finite difference method. For example, spatial derivatives in x of a generic dependant variables u are approximated using equation (6.4). Carrying out this process on the system (7.16)-(7.21) will lead, as we shall show, to

$$\boldsymbol{M}\frac{d\boldsymbol{u}}{dt} = \boldsymbol{A}\boldsymbol{u} + \boldsymbol{f}(x,t). \tag{6.10}$$

Here, $\boldsymbol{u}_{(3+m)n\times 1}$ is the solution vector, $\boldsymbol{M}_{((3+m)n\times(3+m)n)}$ is the time-dependent mass matrix, $\boldsymbol{A}_{((3+m)n\times(3+m)n)}$ is the differentiation matrix and $\boldsymbol{f}_{((3+m)n\times 1)}$ is the source vector account for the reaction terms and the subscripts give the size of the matrices. The diagonal entries of the mass matrix are such that $M_{i,i} = 1$ if the i-th equation is a PDE and $M_{i,i} = 0$ if the i-th equation is an ODE. Note that each of it's elements are constant. We now discuss construction of the matrices $\boldsymbol{M}$, $\boldsymbol{u}$, $\boldsymbol{A}$, and $\boldsymbol{f}$ for our system of PDEs (7.16)-(7.25) if we discretised with n grid points.

6.3.1 The development of the solution vector $\boldsymbol{u}$

The equation system consists of electrolyte concentration, c, electrolyte potential, $\hat{\phi}$, electrode potential, $\hat{\phi}_s$ (which are functions of x and t) and concentration of Lithium in the electrode particles, $\hat{c}_s$ (which is a function of r, x and t). The solution vector $\boldsymbol{u}$ of $c_i, \hat{\phi}_i, \hat{\phi}_{si}$ and $\hat{c}^j_{si}$ (where the subscript i denotes the solution for the particle at $x = i\delta x$

and the superscript j gives the radial position such that $r = j\delta r$) is formed as follows

$$\boldsymbol{u} = \begin{bmatrix} c_1 \\ \vdots \\ c_n \\ \hat{\phi}_1 \\ \vdots \\ \hat{\phi}_n \\ \hat{\phi}_{s1} \\ \vdots \\ \hat{\phi}_{sn} \\ \hat{c}^1_{s1} \\ \vdots \\ \hat{c}^n_{s1} \\ \vdots \\ \vdots \\ \vdots \\ \hat{c}^1_{sn} \\ \vdots \\ \hat{c}^n_{sn} \end{bmatrix}_{((3+m)n\times 1)} \begin{matrix} \left.\begin{matrix} \\ \\ \end{matrix}\right\} \text{Solution for } c_i \\ \left.\begin{matrix} \\ \\ \end{matrix}\right\} \text{Solution for } \phi_i \\ \left.\begin{matrix} \\ \\ \end{matrix}\right\} \text{Solution for } \hat{\phi}_{si} \\ \left.\begin{matrix} \\ \\ \end{matrix}\right\} \text{Solution for particle 1 } \hat{c}^j_{s1} \ (j = 1, \cdots, m) \\ \left.\begin{matrix} \\ \\ \\ \end{matrix}\right\} \text{Solution for particles } 2, \cdots, n-1, \ \hat{c}^j_{si} \ (i = 2, \cdots, n-1, j = 1, \cdots, m) \\ \left.\begin{matrix} \\ \\ \end{matrix}\right\} \text{Solution for particle } n, \ \hat{c}^j_{sn} \ (j = 1, \cdots, m) \end{matrix} \tag{6.11}$$

In order to make the assembles of the matrix ODE system more transparent we shall split the system into its constituent parts (equations for (I) electrolyte concentration, (II) electrolyte potential, (III) solid potential and (IV) lithium concentration in the electrode particles) in §6.3.2 - §6.3.5 before showing how to assemble the equations in the form (6.10) in §6.3.6.

6.3.2 The development of matrices for electrolyte concentration, c

The equation for the electrolyte concentration, c in (7.16) is a time dependent PDE, and hence the mass matrix for this particular equation is

$$\boldsymbol{M}_c = \begin{pmatrix} 1 & 0 & 0 & \cdots & \cdots \\ 0 & 1 & 0 & \cdots & \cdots \\ \vdots & \vdots & \ddots & \ddots & \vdots \\ \cdots & \cdots & \cdots & 1 & 0 \\ \cdots & \cdots & \cdots & 0 & 1 \end{pmatrix}_{n\times n} \tag{6.12}$$

The discretisation of c (7.16), with boundary conditions (7.19 (a))-(7.20 (b)), by central difference (6.4) gives the following differentiation matrix

$$\boldsymbol{A}_c = \frac{1}{\delta x^2} \begin{pmatrix} 1 & 0 & 0 & \cdots & \cdots \\ 1 & -2 & 1 & \cdots & \cdots \\ \ddots & \ddots & \ddots & \ddots & \vdots \\ \cdots & \cdots & 1 & -2 & 1 \\ \cdots & \cdots & \cdots & 2 & -2 \end{pmatrix}_{(n\times n)} . \tag{6.13}$$

The reaction terms in the equation is written in matrix form as

$$\boldsymbol{f}_c = \begin{pmatrix} G(c_1, \hat{c}_{s1}^m, \hat{\phi}_1 - \hat{\phi}_{s1}) \\ G(c_2, \hat{c}_{s2}^m, \hat{\phi}_2 - \hat{\phi}_{s2}) \\ \vdots \\ G(c_{n-1}, \hat{c}_{s(n-1)}^m, \hat{\phi}_{n-1} - \hat{\phi}_{s(n-1)}) \\ G(c_n, \hat{c}_{sn}^m, \hat{\phi}_n - \hat{\phi}_{sn}) \end{pmatrix}_{(n\times 1)} \tag{6.14}$$

Summary The discretisation of (7.16) can thus be represented by the matrix system

$$\boldsymbol{M}_c \frac{d\boldsymbol{u}_c}{dt} = \boldsymbol{A}_c \boldsymbol{u}_c + \boldsymbol{f}_c \tag{6.15}$$

where

$$\boldsymbol{u}_c = \begin{pmatrix} c_1 \\ c_2 \\ \vdots \\ c_{n-1} \\ c_n \end{pmatrix}_{(n\times 1)} \tag{6.16}$$

6.3.3 The development of matrices for electrolyte potential, $\hat{\phi}$

The electrolyte potential equation, $\hat{\phi}$ in (7.17) is an ODE in x, hence the mass matrix is zero matrix

$$[\mathbf{0}]_{n\times n}. \tag{6.17}$$

The discretisation of $\hat{\phi}$ (7.17) with boundary conditions (7.19(b))-(7.20(a)) by central difference (6.4), gives a differentiation matrix that is identical to $\boldsymbol{A}_c$. The matrix for the reaction terms in the equation follows the matrix that identical to $\boldsymbol{f}_c$.

It follows that subsystem of ODEs approximating the electrolyte potential equation (7.17) is given by

$$[\mathbf{0}]\frac{d\boldsymbol{u}_{\hat{\phi}}}{dt} = \boldsymbol{A}_c\boldsymbol{u}_{\hat{\phi}} + \boldsymbol{f}_c \tag{6.18}$$

where

$$\boldsymbol{u}_{\hat{\phi}} = \begin{pmatrix} \hat{\phi}_1 \\ \hat{\phi}_2 \\ \vdots \\ \hat{\phi}_{n-1} \\ \hat{\phi}_n \end{pmatrix}_{(n\times 1)} \tag{6.19}$$

6.3.4 The development of matrices for the electrode potential, $\hat{\phi}_s$

The solid potential equation, $\hat{\phi}_s$ in (7.18) is an ODE in x, and hence the mass matrix is zero matrix

$$[\mathbf{0}]_{n\times n}. \tag{6.20}$$

The discretisation of $\hat{\phi}_s$ (7.18) with boundary conditions (7.21(a)-(b)) by central difference (6.4) gives

$$\boldsymbol{A}_{\hat{\phi}_s} = \frac{1}{\delta x^2}\begin{pmatrix} -2 & 2 & 0 & \cdots & \cdots \\ 1 & -2 & 1 & \cdots & \cdots \\ \ddots & \ddots & \ddots & \ddots & \vdots \\ \cdots & \cdots & 1 & -2 & 1 \\ \cdots & \cdots & \cdots & 2 & -2 \end{pmatrix}_{(n\times n)} . \tag{6.21}$$

The reaction terms matrix in the equation is also identical to that $\boldsymbol{f}_c$ matrix (6.14).

It follows that the subsystem of ODEs approximating the electrode potential equation (7.18) is

$$[\mathbf{0}]\frac{d\boldsymbol{u}_{\hat{\phi}_s}}{dt} = \boldsymbol{A}_{\hat{\phi}_s}\boldsymbol{u}_{\hat{\phi}_s} + \boldsymbol{f}_c \tag{6.22}$$

where

$$\boldsymbol{u}_{\hat{\phi}_s} = \begin{pmatrix} \hat{\phi}_{s1} \\ \hat{\phi}_{s2} \\ \vdots \\ \hat{\phi}_{s(n-1)} \\ \hat{\phi}_{sn} \end{pmatrix}_{(n\times 1)} \tag{6.23}$$

6.3.5 The development of matrices for concentration in the electrode particles, c_s

As noted earlier, the concentration in the solid has 2D spatial dependacy (that is c_s is a function of both r and x), hence the construction of the matrix of equations approximating this variable is more complex than for the other variables. We define c_{si}^{j} where the superscript j denotes radial position in the particle, and the subscript i denotes the position of the particle in the electrode (that is $r_j = j\delta r$, $x_i = i\delta x$). This discretisation is such that at each grid point i in x there is one representative particle, which means if we take n grid points in x, there are n particles.

In order to make the discretisation of c_s much simpler, we introduce the new variables $\hat{c}_s$ defined rescale by $\hat{c}_s = c_s r$, so that (7.23)-(7.24) can now be rewritten (on setting $\mathcal{Q} = 1$ and $D_s(\hat{c}_s) = 1$ as discussed previously)

$$\frac{\partial \hat{c}_s}{\partial t} = \frac{\partial}{\partial r}\left(\frac{\partial \hat{c}_s}{\partial r}\right), \tag{6.24}$$

$$\hat{c}_s|_r = 0 = 0, \qquad \left(\frac{\partial \hat{c}_s}{\partial_r} - \hat{c}_s\right)\bigg|_{r=1} = -G. \tag{6.25}$$

Let consider a particle at position $x = i\delta x$. The equation above is a PDE, in which $\hat{c}_s$ depends on t and hence the mass matrix is similar to $\boldsymbol{M}_c$ (6.12) but of different dimensions

$$\boldsymbol{M}_{cs} = \begin{pmatrix} 1 & 0 & 0 & \cdots & \cdots \\ 0 & 1 & 0 & \cdots & \cdots \\ \vdots & \vdots & \ddots & \ddots & \vdots \\ \cdots & \cdots & \cdots & 1 & 0 \\ \cdots & \cdots & \cdots & 0 & 1 \end{pmatrix}_{m\times m} \tag{6.26}$$

The discretisation of (6.24)-(6.25) using the central difference (6.4) gives

$$\boldsymbol{A}_{cs} = \frac{1}{\delta x^2}\begin{pmatrix} -2 & 2 & 0 & \cdots & \cdots \\ 1 & -2 & 1 & \cdots & \cdots \\ \ddots & \ddots & \ddots & \ddots & \vdots \\ \cdots & \cdots & 1 & -2 & 1 \\ \cdots & \cdots & \cdots & 2 & -2(1-\delta x) \end{pmatrix}_{(m\times m)} . \tag{6.27}$$

We note that, the reaction rate equation appears only at the solid particle surface, $r = 1$ which is at $j = m$ (by boundary condition (6.25)). The matrix for reaction equation for particle at position $x = i\delta x$ is in the form

$$\boldsymbol{f}_{pi} = -\frac{2}{\delta x}\begin{pmatrix} 0 \\ 0 \\ \vdots \\ 0 \\ G(c_i, \hat{c}_{si}^m, \hat{\phi}_i - \hat{\phi}_{si}) \end{pmatrix}_{m\times 1} \quad \text{for } i = 1, 2, \cdots, n \tag{6.28}$$

It follows that the subsystem of ODEs approximating (6.24)-(6.25) for $\hat{c}_s$ at position $x = i\delta x$, is given by

$$\boldsymbol{M}_{cs}\frac{d\boldsymbol{u}_{pi}}{dt} = \boldsymbol{A}_{cs}\boldsymbol{u}_{pi} + \boldsymbol{f}_{pi} \tag{6.29}$$

where

$$\boldsymbol{u}_{pi} = \begin{pmatrix} \hat{c}_{si}^1 \\ \hat{c}_{si}^2 \\ \vdots \\ \hat{c}_{si}^{m-1} \\ \hat{c}_{si}^m \end{pmatrix}_{(m\times 1)} \quad \text{for } i = 1, 2, \cdots, n \tag{6.30}$$

The system of solid concentration for all n particles is thus represented by

$$\boldsymbol{M}_p\frac{d\boldsymbol{u}_p}{dt} = \boldsymbol{A}_p\boldsymbol{u}_p + \boldsymbol{f}_p \tag{6.31}$$

where

$$\boldsymbol{M}_p = \begin{bmatrix} \boldsymbol{M}_{cs} & \cdots & \cdots & \cdots & \cdots \\ \cdots & \boldsymbol{M}_{cs} & \cdots & \cdots & \cdots \\ \cdots & \cdots & \ddots & \ddots & \vdots \\ \ddots & \ddots & \ddots & \boldsymbol{M}_{cs} & \vdots \\ \cdots & \cdots & \cdots & \cdots & \boldsymbol{M}_{cs} \end{bmatrix}_{(mn\times mn)} \tag{6.32}$$

and the differentiation matrix for all the n particles is given by the block tri-diagonal matrix

$$\boldsymbol{A}_p = \begin{bmatrix} \boldsymbol{A}_{cs} & \cdots & \cdots & \cdots & \cdots \\ \cdots & \boldsymbol{A}_{cs} & \cdots & \cdots & \cdots \\ \vdots & \vdots & \ddots & \ddots & \vdots \\ \ddots & \ddots & \ddots & \boldsymbol{A}_{cs} & \vdots \\ \cdots & \cdots & \cdots & \cdots & \boldsymbol{A}_{cs} \end{bmatrix}_{(mn\times mn)} . \tag{6.33}$$

and the source vector matrix for all the n particles is given by

$$\boldsymbol{f}_p = \begin{pmatrix} \boldsymbol{f}_{p1} \\ \boldsymbol{f}_{p2} \\ \vdots \\ \boldsymbol{f}_{p(n-1)} \\ \boldsymbol{f}_{pn} \end{pmatrix}_{(mn\times 1)} . \tag{6.34}$$

6.3.6 The development of $\boldsymbol{A}$, $\boldsymbol{M}$ and $\boldsymbol{f}$

Combining all the matrix elements of all variables for (7.16)-(7.21), we write (6.12)-(6.21),(6.32), (6.33) and (6.34) in the full matrix system (6.10) such that

$$\begin{bmatrix} \boldsymbol{M}_1 & \cdots & \cdots & \cdots \\ \cdots & \boldsymbol{0} & \cdots & \cdots \\ \cdots & \cdots & \boldsymbol{0} & \cdots \\ \cdots & \cdots & \cdots & \boldsymbol{M}_p \end{bmatrix} \frac{\partial \boldsymbol{u}}{\partial t} = \begin{bmatrix} \boldsymbol{A}_1 & \cdots & \cdots & \cdots \\ \cdots & \boldsymbol{A}_1 & \cdots & \cdots \\ \cdots & \cdots & \boldsymbol{A}_2 & \cdots \\ \cdots & \cdots & \cdots & \boldsymbol{A}_p \end{bmatrix} \boldsymbol{u} + \begin{bmatrix} \boldsymbol{f}_1 \\ \boldsymbol{f}_1 \\ \boldsymbol{f}_1 \\ \boldsymbol{f}_p \end{bmatrix} \begin{matrix} \text{System for electrolyte concentration } c \\ \text{System for electrolyte potential } \hat{\phi} \\ \text{System for solid potential } \hat{\phi}_s \\ \text{System for solid concentration } \hat{c}_s \end{matrix} \tag{6.35}$$

where the size of the vector $\boldsymbol{M}$ and $\boldsymbol{A}$ are $((3+m)n \times (3+m)n)$ and vector $\boldsymbol{u}$ is in the form (6.11).

6.4 ode15s

Owing to the fact that our system of equations contains both PDEs and ODEs the mass matrix $\boldsymbol{M}$ is clearly singular. This means that we must use a differential-algebraic solver. Here, we use the *ode15s* solver in MATLAB which is particlarly suitable for solving systems of DAEs (differential-algebraic equations). *ode15s* uses the backward

differentiation formulas which means it is an implicit scheme, with an adaptive time-step and it is also efficient at solving problems that are stiff [79]. However, our system is so large system. For example, takes $n = m = 100$ results in 10300 coupled DAEs. If ode15s attempts to compute all 10300-by-10300 entries in the Jacobian of $\boldsymbol{Au} + \boldsymbol{f}$ any standard desktop computer will simply run out of memory (RAM) and take an impractical amount of time to obtain convergence. Since there is no information on the Jacobian, the routine has to calculate the full Jacobian, numerically. However, one can avoid this situation by explicitly telling the solver that the Jacobian only contains 2650 nonzero entries – substantially less than the 10300×10300 possible nonzeros the finite-differencing code attempts to compute. We can achieve this in two different ways:

1. Provide a Jacobian matrix or a routine to calculate the Jacobian if the Jacobian is not constant. We set the 'Jacobian' option in the odeset structure to the matrix.

2. Provide a Jacobian pattern so that the routine is able to avoid expensive calls to the rate of change function. A Jacobian pattern is a sparse matrix of ones (only appear where the Jacobian is non-zero) and zeros. We set the 'Jpattern' option in the odeset structure to the matrix.

For this study, we adopt the second option by specifying the sparsity pattern of Jacobian matrix. By doing so, the efficiency of the solver is greatly improved. The sparsity structure for the system of ODEs $\boldsymbol{Au}+\boldsymbol{f}$ (6.35) with $n = m = 100$ is shown in Figure 6.1. Providing the sparsity pattern can drastically reduce the computational time needed.

Convergence The error tolerance for this problem is set to be 10^{-8}. The code is assessed for convergence by taking double the number of grid points and seeing whether the results obtained are similar to those computed with $n = 100$. And also by refining the error tolerance to 10^{-6} and seeing whether the results obtained are similar to those computed with error tolerance 10^{-8}. Hence, we believe that the numerical accuracy is good and reliable.

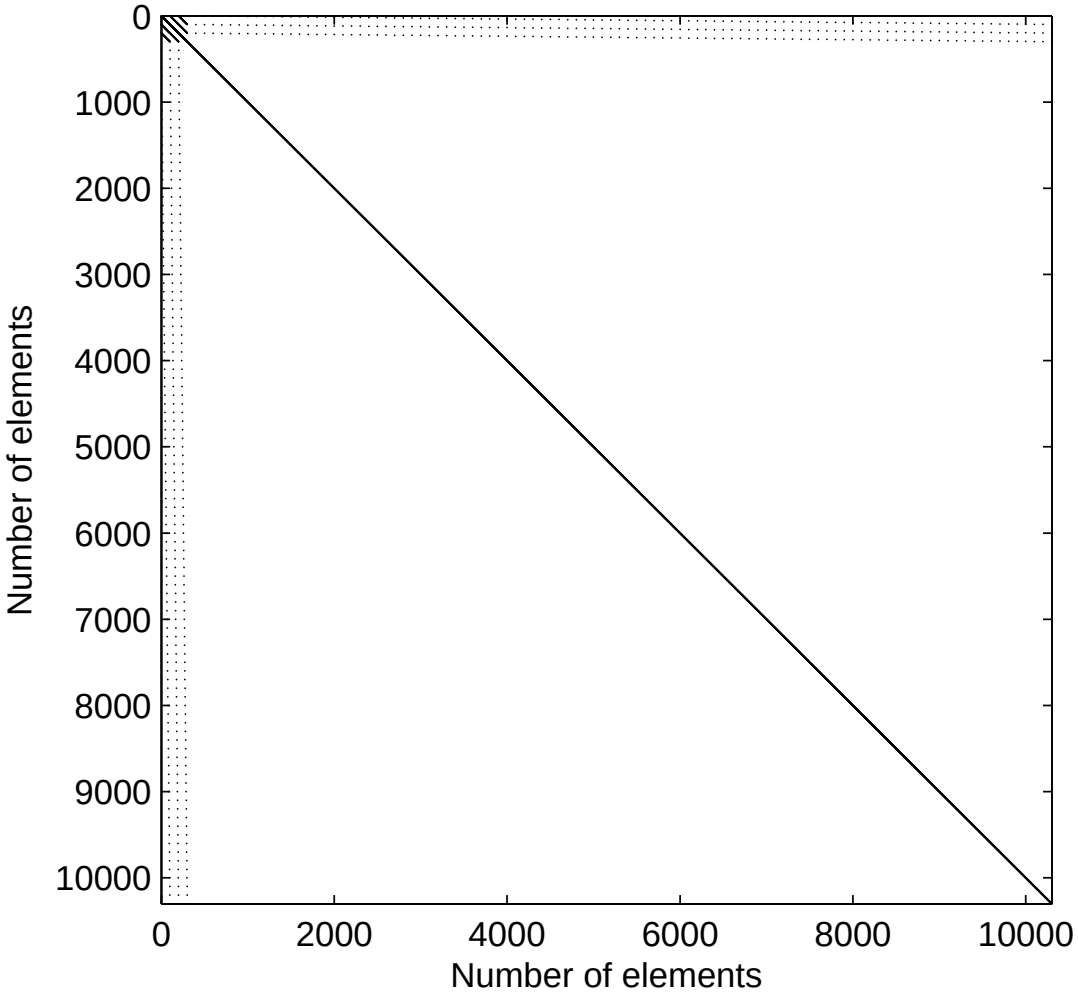

Figure 6.1: The plot of 10300-by-10300 sparse matrix of the Jacobian pattern for $n = 100$. The empty elements are the zeros. The elements 1-100 are for c, 101-200 are for ϕ, 201-300 are for ϕ_s and 301-10300 are for c_s^i.

6.5 Summary

By using finite difference approximations of the space derivatives, i.e. using a constant step space discretisation grid, initial value problems were consisting of a large system of coupled ordinary differential equations (ODEs) in time. MATLABs built-in solver for ODE-systems, *ode15s*, was employed to solve the problems. The procedure we describe offers an efficient, robust and versatile means of simulating the whole system that allows for much simpler coding of the underlying equations than alternative simulation procedures. The MOL technique is especially well-suited to simulating stiff (and hence difficult to solve) equations. It is well known that explicit solvers for parabolic PDEs are limited by a stability criterion that requires small time steps are taken. However, ode15s is designed to solve systems of differential equations using an implicit method and so overcomes this difficulties. Furthermore, the solver employs variable time step length in the integration, increasing calculation speed and accuracy significantly. The resulting numerical method provides a fast and efficient way of calculating solutions to multiscale battery problems such as described in Chapter 4,7, and 8.

Chapter 7

The Half cell Anode

7.1 Introduction

The battery model (4.47)-(4.49) and (5.40)-(5.44) describes the transport process within the full cell battery which consists of current collectors, negative electrode, separator and positive electrode. This model can also be used to describe half-cells which are used to conduct fundamental research on Lithium battery electrodes. The present study is conducted on a graphite anode half cell system.

In order to verify the resulting model is capable of representing the true behaviour of the electrochemical dynamics in the battery system, we compare our results to experimental galvanostatic discharge currents obtained in [85] for a half cell graphite anode. The objectives of the study are to assess the performance of the anodic material and to establish guidelines for their optimization by using the phenomenological moderately concentrated electrolyte model discussed in Chapter 3. The results allow an assessment of the effects of transport, and can be used to evaluate the performance of the system.

7.2 The half cell anode model

The transport model in the liquid electrolyte phase and in the solid phase of the half cell anode is identical to that for the full cell described in (4.47)-(4.49) and (5.40)-(5.44), respectively. The model for the half-cell anode simulates the region between the negative electrode current collector ($x^* = 0$) and the separator ($x^* = L$) where L is the thickness of the electrode as shown in Figure 1.3. We assume that the separator is extremely thin. During discharge, Lithium diffuses in the electrode particles to the solid electrolyte interface where it undergoes a charge transfer reaction. The Lithium ions emitted by this reaction, then diffuse in the electrolyte towards the separator and lithium electrode. For the anode half-cell, the concentration at the separator ($x^* = L$) is

the initial electrolyte concentration (c_0) and the flux of electrolyte concentration is zero at $x^* = 0$. Furthermore, we initially take the electrolyte and electrode are in a state of equilibrium where $c^*|_{t^*=0} = c_0$ and $c_s^*|_{t^*=0} = c_{s,max}$ corresponding to a fully charged half cell anode. Here $c_{s,max}$ is the maximum concentration of intercalated lithium in the graphite electrode. The electrolyte current density at the separator is equal to the total current flowing in the cell divides by its area, $j^*|_{x^*=L} = -I^*/A$. On the other boundary at the current collector, $j^*|_{x^*=0} = 0$. Since the total current in the cell is conserved (see (5.42)), the boundary conditions on the current density in the solid matrix phase follow directly from those on the electrolyte current. That is all the current at the separator is in the electrolyte phase and all the current is in the solid matrix phase at the current collector. The equations and boundary conditions for electrolyte concentration c^*, electrolyte potential $\hat{\phi}^*$ and electrode potential $\hat{\phi}_s^*$ in the half-cell anode can thus be summarized as follows

$$\epsilon_v(x^*)\frac{\partial c^*}{\partial t^*} = \frac{\partial}{\partial x^*}\left(D(c^*)\mathcal{B}(x^*)\frac{\partial c^*}{\partial x^*}\right) - \frac{\partial t_+^0}{\partial x^*}\frac{j}{F} + (1-t_+^0)b_{et}(x^*)G_a^*, \tag{7.1}$$

$$\frac{\partial j^*}{\partial x^*} = Fb_{et}(x^*)G_a^*, \quad \text{where} \quad j^* = -\mathcal{B}(x^*)\kappa(c^*)\left(\frac{\partial \hat{\phi}^*}{\partial x^*} - 2\frac{RT}{F}(1-t_+^0)\frac{\partial \log(c^*)}{\partial x^*}\right) \tag{7.2}$$

$$\frac{\partial j_s^*}{\partial x^*} = -Fb_{et}(x^*)G_a^*, \quad \text{where} \quad j_s^* = -\sigma_s\frac{\partial \hat{\phi}_s^*}{\partial x^*} \tag{7.3}$$

$$\left.\frac{\partial c^*}{\partial x}\right|_{x^*=0} = 0, \qquad c^*|_{x^*=L} = c_0, \tag{7.4}$$

$$j^*|_{x^*=0} = 0 \qquad j^*|_{x^*=L} = -\frac{I^*}{A} \tag{7.5}$$

$$j_s^*|_{x=0} = -\frac{I^*}{A}, \qquad j_s^*|_{x^*=L} = 0 \tag{7.6}$$

$$c^*|_{t^*=0} = c_0, \qquad c_s^*|_{t^*=0} = c_{max} \tag{7.7}$$

where I^* is the total charge flowing across the surfaces of the electrode particles and A is the cross-sectional area of electrode. It remains to specify the reaction rate G_a^* and pose equations for lithium concentration c_s^* in the electrode particles.

We note that in modelling graphite anode, film resistance or the solid electrolyte interface (SEI) layer resistance (R_e) has been considered by Doyle [28] to estimate the ohmic drop across the solid electrolyte interface (SEI) layer covering the graphite particles. Here, it is assumed that the voltage drop in graphite anodes is dominated by Lithium intercalation and the resistance of the SEI layer [48, 53]. In order to account for the latter effect, we modify the standard overpotential term in the Butler Volmer equation (4.49) by adding a voltage drop which is linearly proportional to the reaction current [59]. The modified Butler-Volmer equation has the form

$$G_a^* = k_0(c^*)^{1/2}(c_s^*|_{r^*=a_0})^{1/2}(c_{max}-c_s^*)^{1/2}\left(\exp\left(-\frac{F\eta^*}{2RT}\right) - \exp\left(\frac{F\eta^*}{2RT}\right)\right) \tag{7.8}$$

where

$$\eta^* = \hat{\phi}^* - \hat{\phi}_s^* + U_{eq}^*(c_s^*|_{r^*=a_0}) + FG_a^* R_e. \tag{7.9}$$

Here G_a^* is the lithium flux out of the surface of the particle per unit surface area and R_e is the reciprocal of the surface conductance per unit area (and has units Ωm^2).

Conservation of Lithium in a single spherical active material particle of radius a is described by the diffusion equation

$$\frac{\partial c_s^*}{\partial t^*} = \frac{1}{r^{*2}} \frac{\partial}{\partial r^*} \left(r^{*2} D_s^*(c_s^*) \frac{\partial c_s^*}{\partial r^*} \right) \tag{7.10}$$

$$\left. \frac{\partial c_s^*}{\partial r^*} \right|_{r^*=0} = 0, \tag{7.11}$$

$$-D_s^*(c_s^*) \left. \frac{\partial c_s^*}{\partial r^*} \right|_{r^*=a_0} = G_a^*(c^*, c_s^*|_{r^*=a_0}, \hat{\phi}^* - \hat{\phi}_s^*) \tag{7.12}$$

Equation (7.10)-(7.12) is applied on a continuum basis across the anode giving c_s^* a $2D$ spatial dependacy (i.e $c_s^* = c_s^*(x^*, r^*, t^*)$) where x^* is the particle position, r^* is the radial position within a particle and t^* is time. The other equations in the model (7.1)-(7.3) depend only upon the solid lithium concentration c_s^* at the particle surface through (7.8)-(7.9).

7.3 Nondimensionalisation

The full problem for the half cell is specified by equations (7.1) - (7.12). We note some remarks below before nondimensionalising.

Remarks.

- G_a^* the surface reaction rate is defined so that it is positive if lithium is being released from the particle into the electrolyte (*i.e.* discharge of an anode) and is negative if lithium is being inserted into the particle from the electrolyte (*i.e.* charge of an anode).
- We assume that all electrode particles are identical with radius a_0 so that, $a(x^*) = a_0$ and the volume fraction, $\epsilon_v(x^*)$ are constant. We take the permeability factor to be given by the Bruggeman relation [36] so that

$$\mathcal{B} = \epsilon_v^{1.5} \tag{7.13}$$

The BET surface area b_{et} (by considering a periodic cube contains one spherical particle of radius a where the particle just touches its neighbours) is the surface

area of the spherical particle divided by the volume of the periodic cube such that

$$b_{et} = \frac{\text{Surface area of particle}}{\text{Volume of periodic cube}} = \frac{4\pi a_0^2}{8a_0^3} = \frac{\pi}{2a_0}. \tag{7.14}$$

Electrochemical cells are constructed such that the distance between the current collectors is small in comparison to the other dimensions of the cell. Let us take the area of each of the planar current collectors to be A, the typical current density is $J_0 = I^*/A$, it follows that the magnitude of typical current by $J_0 A$, L is the thickness of the electrode and a_0 is the radius of particle.We nondimensionalize the half-cell system (7.1)-(7.12) as follows:

$$\begin{array}{lllll} I^* \sim J_0 A, & x^* \sim L, & r^* \sim a_0, & a^* \sim a_0, & c^* \sim c_0 \\ G_a^* \sim \dfrac{J_0}{b_{et} LF}, & c_s^* \sim c_{max}, & j^* \sim J_0, & D_s^* \sim D_{s0} & V \sim V_0, \\ \kappa \sim \dfrac{F^2 c_0 D_0}{(1-t_+)RT}, & t^* \sim \tau_0, & D \sim D_0, & b_{et} \sim b_{et}, & j_s^* \sim J_0, \\ V^* = U_{eq,0} + V_0 \hat{V}, & U_{eq^*} = U_{eq,0} + V_0 \hat{U}_{eq}, & \hat{\phi}^* \sim V_0, & \hat{\phi}_s^* = U_{eq,0} + V_0 \hat{\phi}_s & . \end{array} \tag{7.15}$$

Here, c_0 is the initial concentration of Lithium ions in the electrolyte, c_{max} is the maximum concentration of intercalated lithium in the electrodes, V_0 is the typical potential drop across the cell and D_0 is a typical diffusivity in the electrolyte, D_{s0} is the typical diffusivity of Lithium in the solid, τ_0 is the typical timescale for discharge of the cell. An estimate for the volume of the electrode is LA, and it follows that the number of moles of intercalated lithium is of $O(\epsilon_v c_s LA)$. The latter are consumed at a rate $J_0 A/F$ and so the typical timescale for discharge of the cell is

$$\tau_0 = \frac{LF c_{max}}{J_0},$$

this leads to the following dimensionless problem

$$\frac{\mathcal{Q}}{\mathcal{N}} \epsilon_v \frac{\partial c}{\partial t} = \frac{\partial}{\partial x}\left(D(c) \frac{\partial c}{\partial x} \right) + \Gamma G_a, \qquad 0 < x < 1 \tag{7.16}$$

$$\left.\begin{aligned} \frac{\partial j}{\partial x} &= G_a, \\ j &= -\frac{\kappa(c)}{\Gamma}\left(\lambda \frac{\partial \hat{\phi}}{\partial x} - 2(1-t_+^0) \frac{\partial \log(c)}{\partial x} \right), \end{aligned}\right\} 0 < x < 1 \tag{7.17}$$

$$\left.\begin{aligned} \frac{\partial j_s}{\partial x} &= -G_a \\ j_s &= -\Theta \frac{\partial \hat{\phi}_s}{\partial x} \end{aligned}\right\} 0 < x < 1 \tag{7.18}$$

$$\left.\frac{\partial c}{\partial x}\right|_{x=0} = 0, \qquad j|_{x=0} = 0, \tag{7.19}$$

$$\hat{\phi}|_{x=1} = 0, \qquad c|_{x=1} = 1, \qquad j|_{x=1} = -\bar{I}, \tag{7.20}$$

$$j_s|_{x=0} = -\bar{I}, \qquad j_s|_{x=1} = 0, \qquad \left.\hat{\phi}_s\right|_{x=0} = \hat{V}. \tag{7.21}$$

$$\begin{aligned} G_a = \Upsilon c^{1/2}(c_s)^{1/2}(1-c_s)^{1/2} \Bigg[& \exp\left(-\frac{\lambda}{2}(\hat{\phi} - \hat{\phi}_s + \hat{U}_{eq}(c_s|_{r=1}) + \mathcal{R}_e G_a)\right) \\ & - \exp\left(\frac{\lambda}{2}(\hat{\phi} - \hat{\phi}_s + \hat{U}_{eq}(c_s|_{r=1}) + \mathcal{R}_e G_a)\right)\Bigg], \end{aligned} \tag{7.22}$$

$$\mathcal{Q}\frac{\partial c_s}{\partial t} = \frac{1}{r^2}\frac{\partial}{\partial r}\left(r^2 D_s(c_s)\frac{\partial c_s}{\partial r}\right), \qquad 0 < r < 1, \;\; 0 < x < 1 \tag{7.23}$$

$$D_s(c_s)\left.\frac{\partial c_s}{\partial r}\right|_{r=1} = -\mathcal{Q}G_a, \qquad \left.\frac{\partial c_s}{\partial r}\right|_{r=0} = 0 \tag{7.24}$$

$$c|_{t=0} = 1, \qquad c_s|_{t=0} = 1. \tag{7.25}$$

in which the dimensionless parameters in the system are defined by

$$\begin{aligned} &\Gamma = \frac{LJ_0(1-t_+)}{D_0 F c_0}, \qquad \lambda = \frac{FV_0}{RT}, \qquad \mathcal{N} = \frac{a_0^2 D_0}{D_{s0}L^2}, \quad \mathcal{R}_e = \frac{J_0 R_e}{V_0 b_{et} L} \\ &\Upsilon = \frac{b_{et} k c_{max} c_0 L}{J_0}, \quad \mathcal{Q} = \frac{a_0 J_0}{b_{et} L F c_{max} D_{s0}}, \quad \Theta = \frac{J_0 L}{\sigma_s V_0} \qquad . \end{aligned} \tag{7.26}$$

Discussion of dimensionless parameters In the above equations, Γ measures the ratio of the actual ion flux to the maximum sustainable flux of ions in the electrolyte; $\mathcal{N}$ is the ratio of the timescale for diffusion of intercalated lithium into a particle to that for diffusion of lithium ions across the electrode; Θ measures the ratio of the typical voltage in the problem to the typical voltage drop across the solid due to Ohmic losses from current flows through the electrode; Υ gives the ratio of the exchange current density to the typical current density at the surface of an electrode particle; λ gives the ratio of a typical voltage drop across cell to the thermal voltage (and is roughly 39 if we assume that the equilibrium potential drop in graphite across electrode V_0 is about 1V); the ratio of the timescale for diffusion of intercalated lithium into a particle to timescale for intercalation into a particle (as determined by the current density) is given by $\mathcal{Q}$. We have chosen to nondimensionalise the applied current so that the dimensionless variable $\bar{I}$ is of order $O(1)$. Thus, J_0 is determined by $J_0 = I^*(\bar{I})/A$ where $\bar{I}$ is the dimensionless discharge current.

7.4 Model - experimental comparisons for the natural graphite electrode

We compare our results to experimental data for a natural graphite anode half-cell taken from [85]. The electrolyte used is 1M lithium hexafluorophosphate ($LiPF_6$) in 1:1 EC:DEC electrolyte. According to the literatures, the transport properties for a graphite anode vary by several orders of magnitude depending on the electrode materials being used. Table 7.1 lists the parameter values from different authors for three parameters which vary significantly, namely diffusion coefficient in the electrode particles, reaction rate constant and exchange current density.

Parameter	Value	Units	Reference
Lithium diffusivity in solid, $D_s^*(c_s^*)$	$10^{-11} - 10^{-13}$ $(0.1 < y < 0.95)$	$m^2 s^{-1}$	[91],[87]
	$10^{-13} - 10^{-14}$ $(0.05 < y < 0.95)$		[102]
	$10^{-14} - 10^{-15}$ $(0 < y < 0.3)$		[99]
Reaction rate constant, k	10^{-12}	$m^{2.5} mol^{-0.5} s^{-1}$	[85]
	10^{-11}		[72]
	10^{-15}		[15]
Exchange current density, i_0	2.15	Am^{-2}	[37]
	36		[32]

Table 7.1: The values suggested in literature for the properties of graphite anode for Lithium-ion cells.

The diffusion coefficient of Lithium within carbonaceous materials $D_s(c_s)$ is critical to determining the charge/discharge characteristics [38]. The values for the diffusion coefficients change with the Lithium fraction y in Li_yC_6. Lithium intercalates into natural graphite up to a composition of $y = 1$ (fully intercalated) and giving a capacity of $372mAh/g$ while for petroleum coke it is only possible to intercalate up to about $y = 0.5$ [87, 62]. Chabot *et al.* [15] found that the lithium diffusivity in the active material of natural graphite is between 3.9×10^{-14} up to about $3.9 \times 10^{-13} m^2 s^{-1}$ in high performance materials.

We remark that the units of the reaction rate constants vary with the forms of the Butler-Volmer equation being used. Thus, extra care should be taken in determining the value of the reaction rate constant. We now look at the exchange current density which relates to the reaction rate constant in (4.40). The values of this parameter, taken from two different sources, differ by a fraction of 10. Large value may corresponds to a highly reversible charge-transfer process at the surface of insertion compounds. These comparisons show that we have to be extra careful in order to extract the correct data for the transport properties.

Parameter	Value	Units	Reference
Electrolyte Parameters			
Diffusivity of Lithium ions, D_0	2.6×10^{-10}	$m^2 s^{-1}$	[32]
Electrode thickness, L	5×10^{-5}	m	[85]
Volume fraction, ϵ_v	0.4764	-	-
Initial salt concentration, c_0	1000	$molm^{-3}$	[85]
Transference number, t_+^0	0.363	-	[32]
Electrode Parameters			
Reaction rate constant, k	3×10^{-12}	$m^{2.5} mol^{-0.5} s^{-1}$	[85]
Diffusion coefficient in the solid, D_{s0}	9×10^{-14}	$m^2 s^{-1}$	[85]
Particle radius, a_0	1.1×10^{-5}	m	[85]
Conductivity in the solid, σ_s	100	Sm^{-1}	[85]
Maximum concentration in the solid, c_{max}	18000	$molm^{-3}$	[85]
Other Parameters			
Faraday constant, F	96487	$Cmol^{-1}$	[23]
Universal gas constant, R	8.3144	$Jmol^{-1}K^{-1}$	[23]
Temperature, T	298	K	[23]
SEI layer resistance, R_e	2.5×10^{-2}	Ωm^2	[85]

Table 7.2: Parameter values used in the model.

The electrode specific information used in this work is listed in Table 7.2. In [85, 28], the contact resistance R_e is used as a fitting parameter at different discharge currents. In the nondimensionalisation, we take $V_0 = 1$Volt to be the typical cell voltage, J_0 to be $13Am^{-2}$ (corresponding to a $1C$ discharge), the dimensionless parameters calculated from the parameter values listed in Table 7.2 are

$$\begin{aligned} &\Gamma \sim 0.026, \quad \lambda \sim 38.9, \qquad \mathcal{N} \sim 421, \qquad \mathcal{R}_e \sim 7 \times 10^{-5} \\ &\Upsilon \sim 0.17, \quad \mathcal{Q} \sim 0.214, \quad \Theta \sim 6.5 \times 10^{-6} \qquad . \end{aligned} \tag{7.27}$$

We note that $\mathcal{R}_e$ is small, hence the dimensionless reaction rate equation (7.22) can be approximated to

$$\begin{aligned} G_a \quad \approx \quad & \Upsilon c(c_s)^{1/2}(1-c_s)^{1/2} \left[\exp\left(-\frac{\lambda}{2}(\hat{\phi} - \hat{\phi}_s + \hat{U}_{eq}(c_s|_{r=1})) \right) \right. \\ & \left. - \exp\left(\frac{\lambda}{2}(\hat{\phi} - \hat{\phi}_s + \hat{U}_{eq}(c_s|_{r=1})) \right) \right], \end{aligned} \tag{7.28}$$

and this significantly reduces the difficulty of the numerical procedure.

We take the diffusivity in the electrode particles $D_s(c_s)$ to be constant and equal to that used by Doyle and Fuentes [32] in whose results gave reasonable agreement to experimental data from [85]. We note however, that a concentration-dependant diffusion coefficient is reported by some authors ([87],[49],[102]). The conductivity in the electrolyte, $\kappa(c^*)$, and the diffusion coefficient, $D(c^*)$ were fitted to experimental data by

Riemers [90] and are given by equations (3.72) and (3.71), respectively. Here, the equilibrium potential has been reported by Thomas [89] (determined at a very low discharge rate $C/25$) and fitted to the equation

$$\begin{aligned} U^*_{eq}(y) &= 0.124 + 1.5\exp(-70y) - 0.0351\tanh\left(\frac{y-0.286}{0.083}\right) \\ &\quad -0.0045\tanh\left(\frac{y-0.9}{0.1119}\right) - 0.035\tanh\left(\frac{y-0.99}{0.05}\right) - 0.0147\tanh\left(\frac{y-0.5}{0.034}\right) \\ &\quad -0.102\tanh\left(\frac{y-0.194}{0.142}\right) - 0.022\tanh\left(\frac{y-0.98}{0.0164}\right) - 0.011\tanh\left(\frac{y-0.124}{0.0226}\right) \\ &\quad +0.0155\tanh\left(\frac{y-0.105}{0.029}\right) \end{aligned} \tag{7.29}$$

where y represents the amount of lithium intercalated in the formula $\mathrm{Li}_y\mathrm{C}_6$ and U_{eq} is measured in Volts. The expression, however, is not fitted to the equilibrium potential curve shown in [85]. This may be due either to a typographical error or a mistake during the fitting process. Therefore, to reduce the degree of error, we extract the experimental equilibrium potential data ourselves and fitted to the interpolation approximation using Matlab (this is plotted by a dashed curve in Figure 7.1).

7.4.1 Results and Discussions

The experimental data used for the comparison was reported by Shim and Striebel [81]. The parameters used in the model in order to compare to the experimental results are listed in Table 7.2.

Figure 7.1 shows the comparison between experimental and model discharge curves. The model compares reasonably well to the experimental data, especially at early stages of the discharge. However, the potential is seen to underestimate the finishing potential drop especially at high discharge rate. This could be related to the assumption that the lithium diffusion coefficient in the electrode particles D_s is constant. The diffusivity data in [91] suggests that $D_s(c_s)$ is a fairly rapidly decreasing function of c_s.

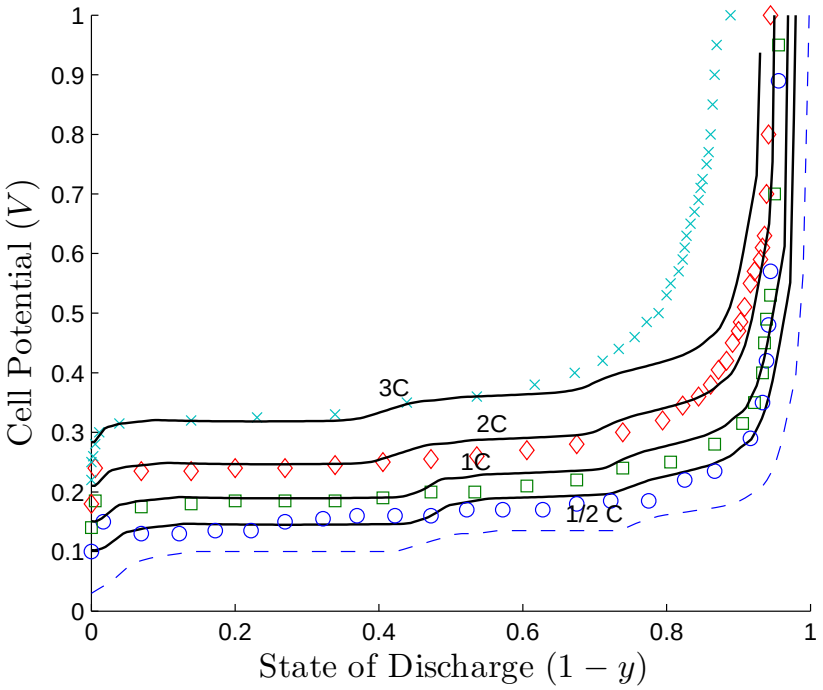

Figure 7.1: The comparison of model-experimental data for the graphite half cell discharge curve at different currents. Solid lines represent the numerical results and symbols represent experimental data at various discharge currents. The dashed curve represents our fit to the equilibrium potential curve.

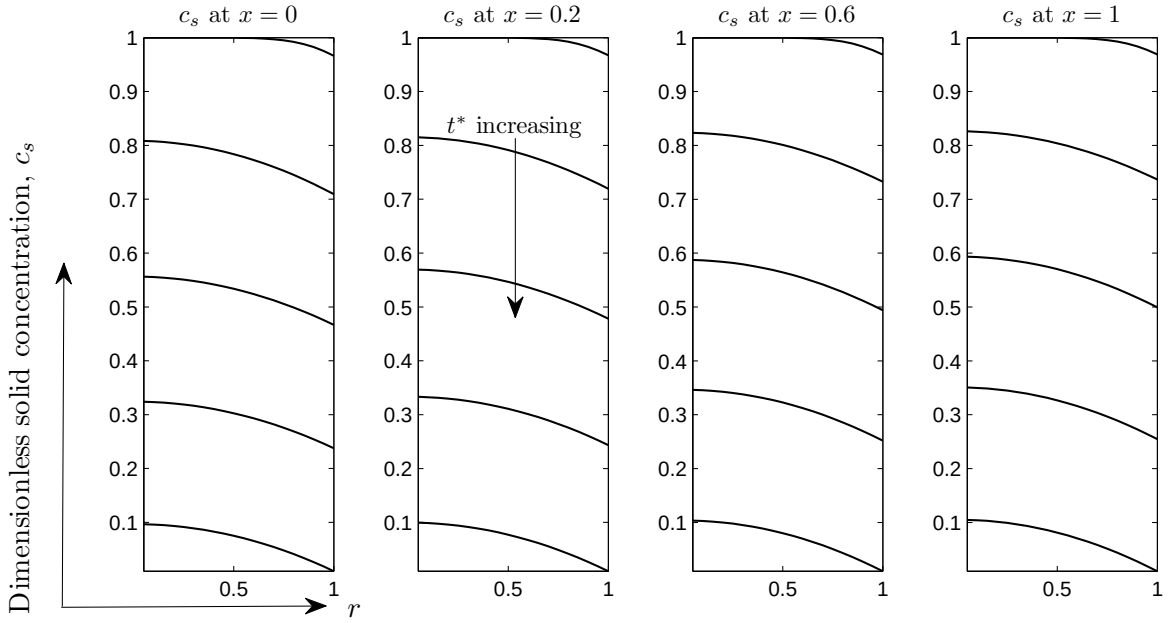

Figure 7.2: The dimensionless concentration profiles of the intercalated Lithium in the solid at different positions across the cell for the discharge rate $1C$. The profiles are measured at $t^* = 104s, 208s, 312s, 416s, 520s$.

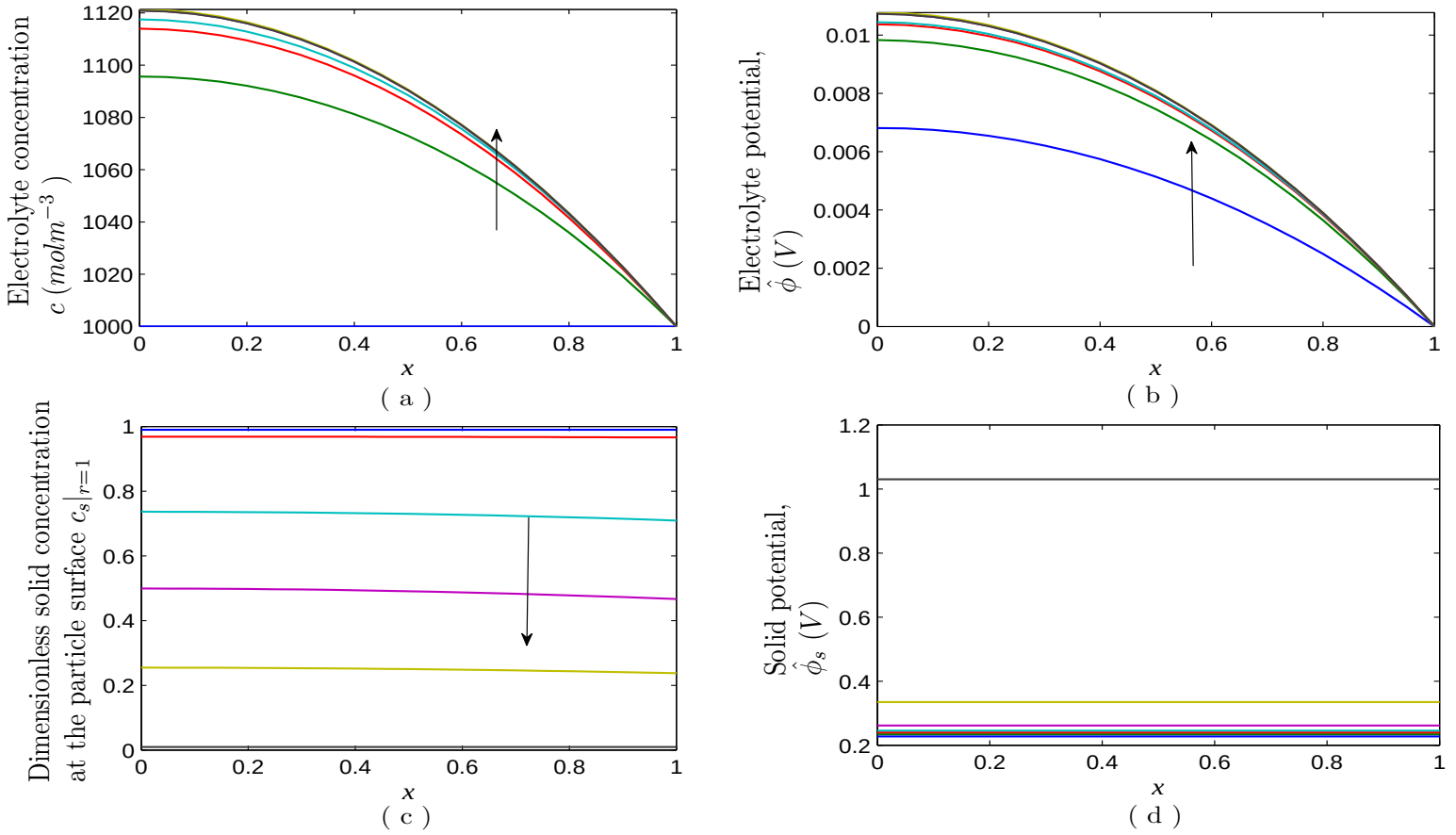

Figure 7.3: (a) The concentration profile of Lithium ions in the electrolyte; (b) The potential in the electrolyte; (c) The solid concentration at the particle surface and (d) The potential in the solid at $1C$ discharge rate. $\uparrow$ is the direction of increasing time. The profiles are measured at $t^* = 104s, 208s, 312s, 416s, 520s$.

The important factors for optimizing the performance of the cell are good utilization of the active electrode material and good transport properties in the electrolyte. Figure 7.3 shows the concentration of Lithium ions in the electrolyte, the concentration of lithium at the particle surface across the spatial variable x and the electrolyte and solid potentials. As time increases, the results illustrate that electrolyte concentration, c increases only a very slightly from its initial concentration (see Figure 7.3 (a)). In addition, the electrolyte potential $\hat{\phi}$ only changes by a very small amount (see Figure 7.3 (b)). These variables do not appear to significantly alter the half-cell discharge. Notably the $\hat{\phi}$ values are very small compared to the potential in the electrode $\hat{\phi}_s$, thus the Butler Volmer equation (7.22) predominantly depends upon the concentration in the solid and the solid potential $\hat{\phi}_s$. Figure 7.3 (d) shows the solid potential profile is approximately uniform and constant across the electrode as the dimensionless parameter Θ (appearing in (7.18)) is extremely small. This allows us to approximate the electrode potential by $\hat{\phi}_s = \hat{\phi}_s(t)$ (i.e. it is independent of space). We thus conclude the charge-discharge behaviour is limited by the solid-state transport and intercalation of lithium.

To demonstrate the dependence of the solid-phase concentration profiles on distance across the electrode in more detail, the lithium concentration profiles c_s (at 1C discharge rate) in the electrode particles at different positions ($x = 0, 0.2, 0.6, 1$) are shown in Figure 7.2. The particle closest to the current collector at $x = 0$ is discharged very slightly faster than the particle nearest the separator. However, the concentration at different positions x are almost identical (see Figures 7.3 (c) and 7.2). The profiles show that the concentration in the solid is driven to zero as time increases. The abrupt loss of capacity in Figure 7.1 occurs as $c_s|_{r=1}$ is zero, and hence the Lithium remaining in the particles in $0 < r < 1$ is effectively inaccessible after this time.

7.4.1.1 An approximation solution

Based on the discussion above, we now approximate the functions c, $\hat{\phi}_s$ and $c_s|_{r=1}$ as functions of time only and $\hat{\phi} \approx 0$. If we integrate (7.17) from $x = 0$ to $x = 1$ and apply the boundary conditions (7.19(b)) and (7.20(c)) we get

$$\int_{x=0}^{x=1} G_a dx = -\bar{I} \tag{7.30}$$

where

$$\begin{aligned} G_a &= \Upsilon c(c_s|_{r=1})^{1/2}(1 - c_s|_{r=1})^{1/2} \left[\exp\left(-\frac{\lambda}{2}(-\hat{\phi}_s + \hat{U}_{eq}(c_s|_{r=1}))\right)\right. \\ &\quad \left. - \exp\left(\frac{\lambda}{2}(-\hat{\phi}_s + \hat{U}_{eq}(c_s|_{r=1}))\right)\right] \end{aligned} \tag{7.31}$$

Since G_a depends only on functions of time, it is also spatially independent and the integration in (7.30) is thus trivial and yields on substituting for G_a from (7.31)

$$-\frac{\bar{I}}{\Upsilon c(\,c_s|_{r=1})^{1/2}(1-\,c_s|_{r=1})^{1/2}} = \exp\left(-\frac{\lambda}{2}(-\hat{\phi}_s+\hat{U}_{eq}(c_s|_{r=1}))\right)-\exp\left(\frac{\lambda}{2}(-\hat{\phi}_s+\hat{U}_{eq}(c_s|_{r=1}))\right). \quad (7.32)$$

We can simplify (7.32) by noting that the term in the exponential is dominated by the $\hat{\phi}_s - \hat{U}_{eq}$ (because the size of $\hat{\phi}$ is an order 10^{-3}) and by using the trigonometric hyperbolic identity $\sinh(x) = \dfrac{\exp(x)-\exp(-x)}{2}$, to obtain

$$-2\sinh\left(\frac{\lambda}{2}(\hat{U}_{eq}(c_s|_{r=1})-\hat{\phi}_s)\right) = -\frac{\bar{I}}{\Upsilon c(\,c_s|_{r=1})^{1/2}(1-\,c_s|_{r=1})^{1/2}} \quad (7.33)$$

which gives an approximate solution for $\hat{\phi}_s$

$$\hat{\phi}_s(t) = \hat{U}_{eq}(c_s|_{r=1}) - \frac{2}{\lambda}\,\mathrm{arcsinh}\left(\frac{\bar{I}}{\Upsilon c(c_s|_{r=1})^{1/2}(1-c_s|_{r=1})^{1/2}}\right) \quad (7.34)$$

The analytic solution (7.34) requires information about $c_s|_{r=1}$ which is determined by solving the diffusion equation (7.23) - (7.24) for a single representation particle. On solving for $c_s|_{r=1}$ and substituting in (7.34), we can use (7.21(c)) to determine $\hat{V}(t)$

$$\hat{V}(t) = \hat{\phi}_s(t). \quad (7.35)$$

Summary To summarise a very good approximation of the solution may be calculated by solving for $c_s(r,t)$ from (7.23) - (7.24). The result of this calculation is used to obtain $c_s|_{r=1}$ which is then substituted into (7.34) to obtain the voltage of the electrode $\hat{\phi}_s(t)$ and hence the potential drop $\hat{V}(t)$, from (7.35) across half cell.

The comparison between these approximate discharge curves and discharge curves calculated by solution to the full model is shown in Figure 7.4. The results show very good agreement. In summary a simple model, in which the limiting effect is lithium diffusion within the electrode particles provides an extremely good approximation of the discharge.

7.4.1.2 Concentration-dependent of diffusion coefficient

In what follows we use the approximation discussed above to reduce the cost of computational run time. Since the assumption of constant diffusion coefficient in the electrode particles underestimates the drop in cell voltage as the cell discharges, we investigate

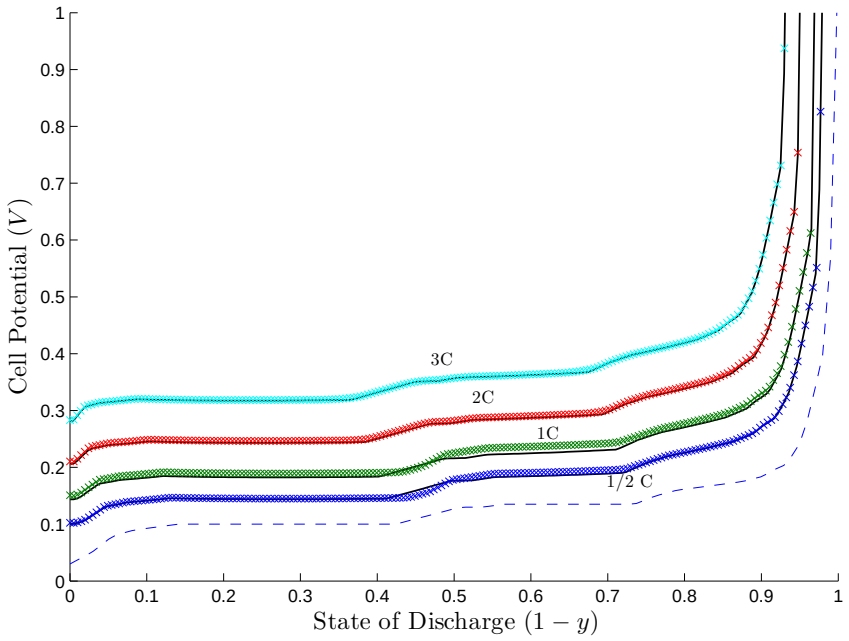

Figure 7.4: The comparison of analytic-numerical solution for the graphite half cell discharge curves at different currents. Solid lines represent the analytic solutions and symbols represent the numerical solution. The dashed curve represents the equilibrium potential curve.

the effects of non-linear diffusion on the problem. The values of diffusion for the same materials, reported by different literatures vary by several orders of magnitude. Conduction in graphite is strongly dependent upon the degree of crystallinity. As the fraction (let say f) of amorphous phases (fraction of crystalline phases, $1 - f$) increases, and diffusivity increases [68].

Modelling of concentration-dependent diffusivity in graphite by Verbrugge and Koch [91] given good agreement to their experimental data . The non-linear diffusion equation that they use to model their data was calibrated from data provided by Takami [87] for which the diffusion coefficient changes (exponentially) by two orders of magnitude ($10^{-14} - 9 \times 10^{-11} m^2 s^{-1}$) as the fractional occupancy y, in Li_yC_6, varies between 0 to 1. Levi and Aurbach [49] and Zhang [102] reported that the diffusion coefficient of graphite is between $10^{-14} - 10^{-13} m^2 s^{-1}$. These inconsistencies probably result from the different crystal structure and of their samples [87, 49]. Figure 7.5 compares the diffusion coefficients with respect to composition of y in Li_yC_6 reported by these different authors.

Using the data provided by Verbrugge and Koch [91] in our model, results in an over prediction of the cell potential (see Figure 7.7). At the beginning of discharge the particles are filled with intercalated lithium, and the diffusion coefficient is low. Toward the end of discharge, the intercalated lithium concentration is lower, and the diffusion coefficient rises. Because the intercalated lithium concentration is lowest at the particle

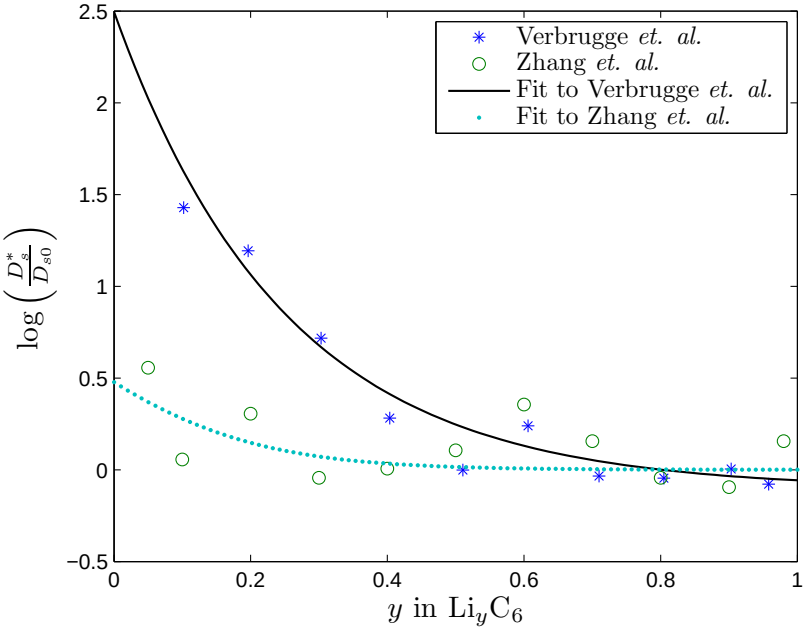

Figure 7.5: Experimental data of composition-dependant diffusion coefficient by Zhang *et al.* [102] and Verbrugge *et al.* [91]. The solid lines and dots are fitting to the experimental data by Verbrugge *et al.* and Zhang *et al.* respectively.

surface and highest at the center of the particle, the diffusion coefficient is always largest at the particle surface and smallest at the center of the particle. The large difference magnitude of D_s and the slow diffusion of lithium in the lithium rich region near the centre of the particle results in lithium depletion occurs near the surface ($r = 1$) in a short time as shown in Figure 7.6 and hence to c_s at the surface being driven to zero after a relatively short time. By using the less extreme data of Zhang [102] and Levi [49] for the diffusion coefficient we obtain results that accurately describe the experimental data. Comparison between discharge curves calculated using the diffusion coefficient obtained from fitting to the data from [91] and from [102] is made in Figure 7.7.

Based on the above analysis, we use the diffusion coefficient given by Zhang for the model comparison to the discharge curve given by Srinivasan and Newman [84]. The following equation was used to fit to the data measured by Zhang [102]

$$D_s(c_s) = 7 \times 10^{-14}(1 + 1.5\exp(-8c_s)) \tag{7.36}$$

where the dimensionless c_s is the composition of y in $\mathrm{Li}_y\mathrm{C}_6$. The results are then compared with the experimental data and are shown in Figure 7.8 at various discharge rates, where excellent agreement is seen. Since the particle surface concentration is homogeneous across the electrode (see Figure 7.3 (c)), we simulate (7.23) for one particle instead of many particles.

The abrupt loss of capacity at $3C$ discharge rate caused by the depletion of Lithium

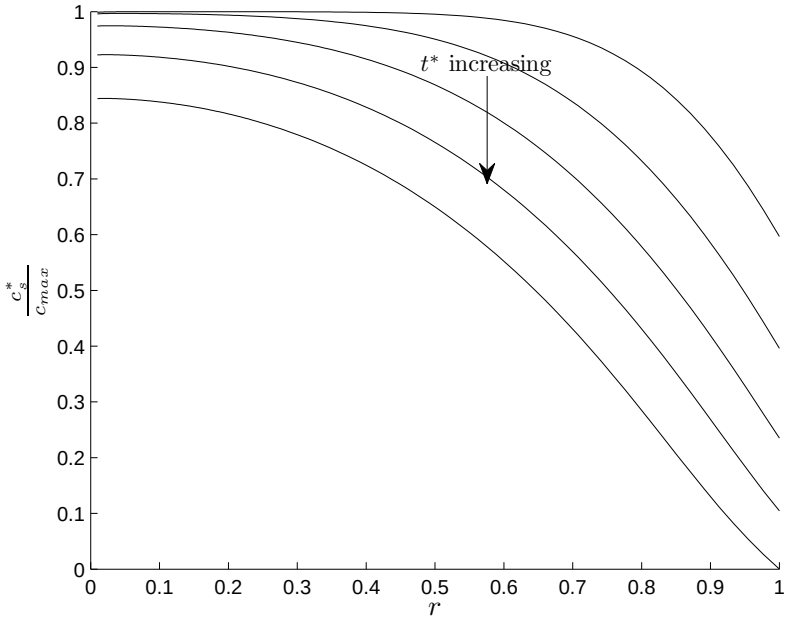

Figure 7.6: The concentration of Lithium within the electrode particle with diffusion coefficients from fitting to the data from Verbrugge *et al.* [91] as shown in Figure 7.5 at $3C$ discharge rate. The profiles are measured at $t^* = 15s, 30s, 45s, 60s, 75s$.

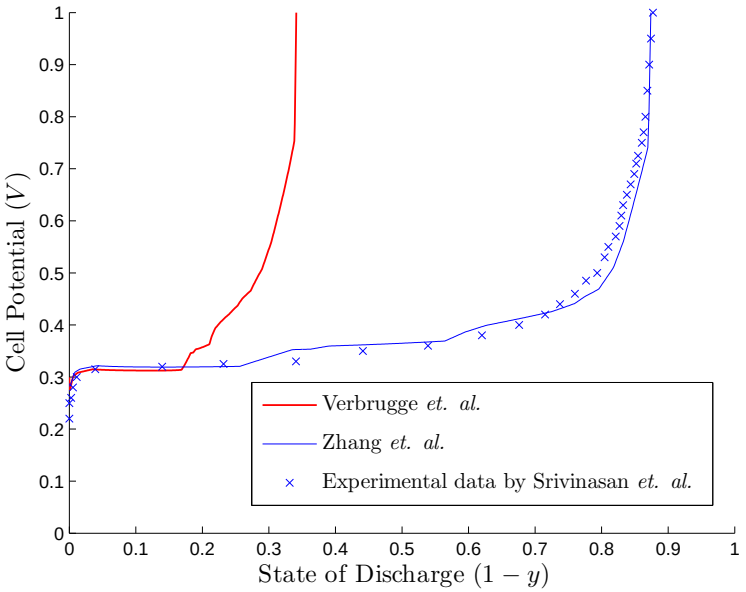

Figure 7.7: Discharge curves plot with the diffusion coefficient data given by Verbrugge *et al.* (red) and Zhang *et al.* (blue) at $3C$ discharge rate. The large difference magnitude of $D_s(c_s)$ (see Figure 7.5) results in lithium depletion at the surface in a relatively short time (see Figure 7.6).

in active material at the particle surface is shown in Figure 7.9. As expected, a higher

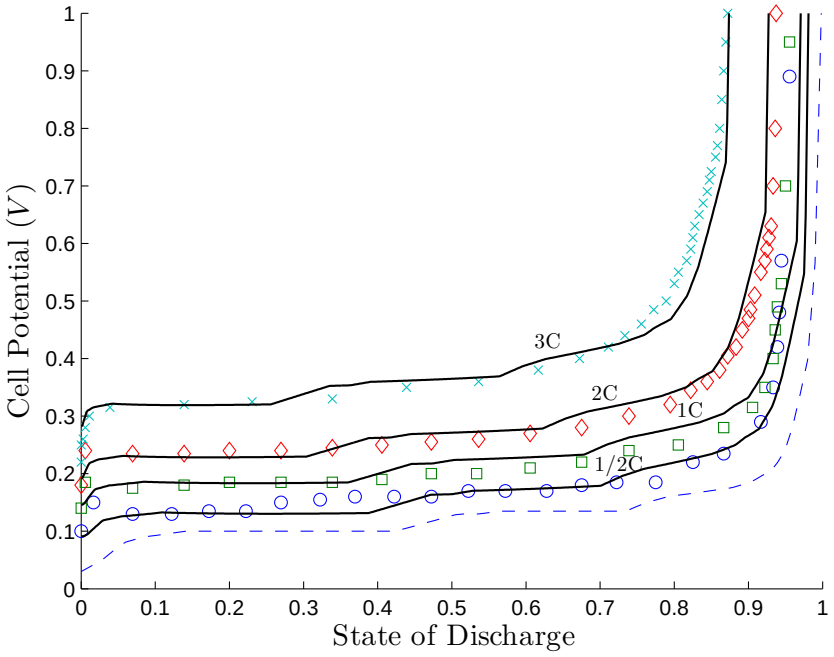

Figure 7.8: The comparison of non linear diffusion coefficient-experimental data for the graphite half cell discharge curves at different currents. The curves are obtained by analytic approximation solution (7.34) where the diffusion equation in the solid (see (7.23)-(7.24)) is solved numerically. The nonlinear diffusion coefficient (the fitting to the data from Zhang *et al.* [102]) is given by equation (7.36). Solid lines represent the analytic solutions and symbols represent experimental data at various discharge currents. The dashed curve represents the equilibrium potential curve.

current density leads to a lower utilization of active material and therefore lower capacity.

7.5 Summary

The battery model has been verified in predicting the cell potential and assessing the battery performance, especially at initial stages of discharge. The assumption of a constant diffusion coefficient D_s for Lithium in the electrode particles, underestimated the voltage increase that occurs close to the end of the discharge. The numerical results show that the limiting factor for the lithium carbide half cell performance is the solid state diffusion in the electrode particles. The numerical results also show that the electrolyte phase has a negligible effect on the half cell discharge and that the electrode particles discharge almost synchronously. This allowed us to derive an analytic approximation for the potential drop $V(t)$ across the cell. The influence of concentration-dependant diffusion of lithium in the electrode particles is clarified and our results give a much more accurate comparison to experimental data than that achieved by Newman and Srinivasan [84].

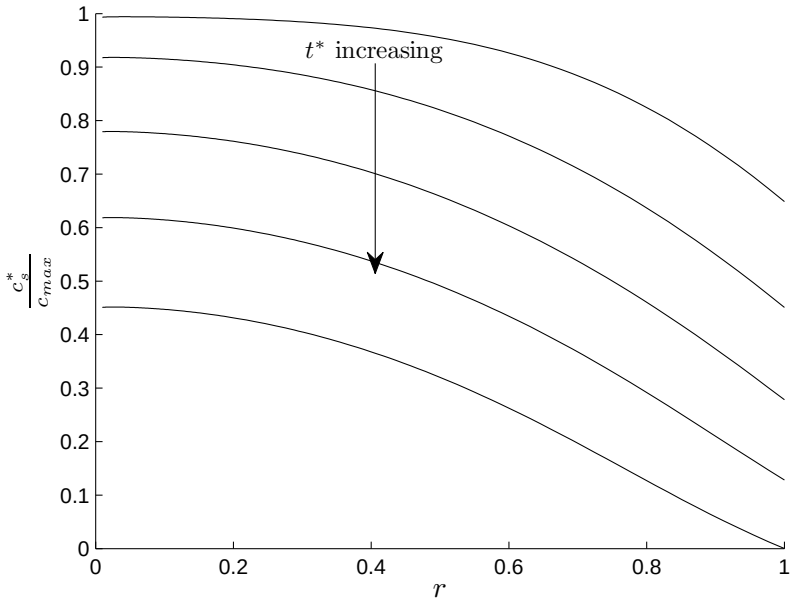

Figure 7.9: The dimensionless concentration of Lithium within the electrode particle at $3C$ discharge rate where $D_s(c_s)$ is calculated using data from Zhang *et al.* [102] (see formula (7.36)). The profiles are measured at $t^* = 30s, 60s, 90s, 120s, 150s$.

Chapter 8

Half cell cathode

8.1 Introduction

In the previous chapter we demonstrated that the model accurately predicts the cell voltage for a half cell graphite anode for a range of discharge rates. In this chapter, we investigate the ability of the model to predict the behaviour of a half-cell cathode. The cathode materials commonly used in lithium ion batteries are $LiCoO_2$, $LiMnO_4$ and $LiFePO_4$. The present study will consider the $LiFePO_4$ cathode half-cell. The nature of the rate limitations within composite electrodes of $LiFePO_4$ is complicated. Initially, they were attributed to the poor electronic conductivity, which resists electron transport within the particles. However, the electronic conduction network has been improved with carbon coating resulting in a substantial increase in the use of $LiFePO_4$ as a cathode materials nowadays [33, 43]. Ion transport has been improved by controlling the composition and the structure of the composite electrode. This can for example be achieved by using carbon black, as a binder, and leaving some open porosity for the electrolyte [46]. $LiFePO_4$ is a phase separating material, as evidenced by its flat discharge curve characteristics (the potential is almost independent of degree of discharge until the particle is fully discharged [65] at which point it drops abruptly).

Srinivasan and Newman [84] modelled Lithium transport in cathode particles by a two-phase "shrinking core" model and compared results of their mathematical model to their own experiments. Their model showed reasonable agreement to the experimental data where the particles were assumed to be distributed between two sizes. Farrell and Dargaville [23] have embedded a shrinking-core based model on a three-scale battery model which again compares reasonably to the experimental data of Srinivasan and Newman [84]. The transport limitations in the solid was found to be the main factor of capacity loss. However, in their further work [24], they state that a "shrinking core" model is not an accurate description of the phase transformation in $LiFePO_4$ and remarks that the good agreement between the "shrinking core" model and the experimental

discharge curves [84] is obtained because the electrical resistance (in the solid particles) and electrolyte resistance (in the thick, $62\mu m$ cathodes), limit the discharge rather than lithium transport within the cathode particles [24].

Owen *et al.* [46] found that the performance of $LiFePO_4$ in a composite nano-structured electrode is significantly improved by carbon coating and inferred that Lithium diffusion in the solid is not limiting for nanoscale electrode particles. In their modelling of this problem (which is quite simplistic), at a high discharge rate, they assumed that the electrolyte resistance restricts the discharge as each electrode particle is either fully charged or discharged and solid state limitations are negligible. This led them to conclude that at high discharge rates the electrolyte diffusion limits the cell discharge as a consequence of electrolyte depletion in certain regions of the cell halting discharge. Here, we investigate a nanostructured electrode such as that considered by Owen *et al.* [46] and compare our results to their experiments. We model diffusion of Lithium in the electrode particles by a linear diffusion equation with a very large diffusivity claiming that since diffusion in the nanoparticles is not rate limiting, the choice of diffusion model does not significantly affect our results. We could have, of course, used an infinitely fast diffusion model (such as postulated in Richardson *et al.* [74]) without materially affecting the result.

8.2 Transport data and parameter values used in the simulation

The diffusion timescale of Lithium across a solid electrode particles is extremely fast in comparison to the diffusion timescale of Lithium ions (in the electrolyte) across the entire width of the cell provided particle sizes are less than $1\mu m$ (hence we take D_s to be constant). The cell is filled with 1M $LiPF_6$ in 1:1 EC:DMC electrolyte. The half-cell cathode model is similar to that given in (4.47)-(4.49) and (5.43)-(5.44) for the full cell. Here $x^* = 0$ denotes the position of the separator and $x^* = L_c$ that of the cathodic current collector (thickness of cathode). Hence, the battery model for half-cell cathode is

$$\epsilon_v(x^*)\frac{\partial c^*}{\partial t^*} = \frac{\partial}{\partial x^*}\left(D(c^*)\mathcal{B}(x)\frac{\partial c^*}{\partial x^*}\right) - \frac{\partial t_+^0}{\partial x^*}\frac{j^*}{F} + (1-t_+^0)b_{et}G_c^*, \tag{8.1}$$

$$\frac{\partial j^*}{\partial x^*} = Fb_{et}^*(x^*)G_c^*,$$

$$\text{where} \quad j^* = -\mathcal{B}(x)\kappa(c^*)\left(\frac{\partial \hat{\phi}^*}{\partial x^*} - \frac{2RT}{F}(1-t_+^0)\frac{\partial \log(c)^*}{\partial x^*}\right) \tag{8.2}$$

$$\frac{\partial j_s^*}{\partial x^*} = -Fb_{et}^*(x^*)G_c^*, \quad \text{where} \quad j_s^* = -\sigma_s\frac{\partial \hat{\phi}_s^*}{\partial x^*} \tag{8.3}$$

$$c^*|_{x^*=0} = c_0, \qquad \left.\frac{\partial c^*}{\partial x^*}\right|_{x^*=L_c} = 0, \tag{8.4}$$

$$\left.\hat{\phi}^*\right|_{x^*=0} = 0, \qquad j^*|_{x^*=L_c} = 0, \tag{8.5}$$

$$j_s^*|_{x^*=0} = 0, \qquad j_s^*|_{x^*=L_c} = -\frac{I^*}{A}. \tag{8.6}$$

Note that the half cell potential, V^*, is usually modelled by the expression

$$V^* = \hat{\phi}_s^*|_{x*=L_c} - \hat{\phi}^*|_{x^*=0} - R_c I^* \tag{8.7}$$

This comprises two parts: the potential difference between the electrode (where it contacts the current collector) and the electrolyte at the separator; and the ohmic drop at the current collector electrode interface caused by contact resistance, R_c. Since we set the potential, $\hat{\phi}^*$ at the separator to be zero (see (8.5(a))), and hence the half cell potential becomes

$$V^* = \hat{\phi}_s^*|_{x^*=L_c} - R_c I^*. \tag{8.8}$$

The solid state diffusion of Lithium in the spherical cathode particles is modelled by the diffusion equation

$$\frac{\partial c_s^*}{\partial t^*} = \frac{D_s}{r^{*2}}\frac{\partial}{\partial r^*}\left(r^{*2}\frac{\partial c_s^*}{\partial r^*}\right) \tag{8.9}$$

$$\left.\frac{\partial c_s^*}{\partial r^*}\right|_{r^*=0} = 0, \tag{8.10}$$

$$-D_s\left.\frac{\partial c_s^*}{\partial r^*}\right|_{r^*=a(x^*)} = G_c^*(c^*, c_s^*|_{r^*=a(x^*)}, \hat{\phi}^* - \hat{\phi}_s^*). \tag{8.11}$$

Here r^* is distance from the centre of the particle, $a(x^*)$ is the radius of the spherical electrode particles as a function of position x in electrode, c_s^* is the solid concentration and G_c^* is the flux (per unit area) of Lithium out from the surface of the particle which is determined by the reaction rate at the particle surface which in turn is usually described by the following Butler-Volmer equation

$$G_c^* = k_0(c^*)^{1/2}(c_s^*|_{r^*=a(x^*)})^{1/2}(c_{max} - c_s^*|_{r^*=a(x^*)})^{1/2}\left(\exp\left(-\frac{F\eta^*}{2RT}\right) - \exp\left(\frac{F\eta^*}{2RT}\right)\right) \tag{8.12}$$

where the overpotential $\eta^* = \hat{\phi}^* - \hat{\phi}_s^* + U_{eq}^*(c_s^*|_{r^*=a(x^*)})$. G_c^* is defined so that during discharge, it is negative as Lithium is inserted into the cathode particles from the electrolyte. In order to simulate discharge we take the initial concentration in the electrode particles to be small, that is

$$c_s^*|_{t^*=0} = c_{s0} \tag{8.13}$$

where $c_{s0} = 0.02c_{max}$ (see, for example [84]).

We assume that all electrode particles are identical with radius a_0 so that, $a(x^*) = a_0$ and the volume fraction, $\epsilon_v(x^*)$ are constant. We take the permeability factor to be given by the Bruggeman relation [36] so that

$$\mathcal{B} = \epsilon_v^{1.5} \tag{8.14}$$

The BET surface area b_{et} (by considering a periodic cube contains one spherical particle of radius a where the particle just touches its neighbours) is the surface area of the spherical particle divided by the volume of the periodic cube such that

$$b_{et} = \frac{\text{Surface area of particle}}{\text{Volume of periodic cube}} = \frac{4\pi a_0^2}{8a_0^3} = \frac{\pi}{2a_0}. \tag{8.15}$$

8.2.1 Nondimensionalisation

The nondimensionalisation for half cell cathode system is identical to that discussed in Section 7.4 with the exception that now

$$x^* \sim L_c, \quad G^* \sim \frac{J_0 a_0}{b_{et,0} L_c F}. \tag{8.16}$$

For other scaling, refer (7.15). The nondimensionalisation leads to the following system of dimensionless equations

$$\frac{\mathcal{Q}}{\mathcal{N}}\epsilon_v \frac{\partial c}{\partial t} = \frac{\partial}{\partial x}\left(\mathcal{B}D(c)\frac{\partial c}{\partial x}\right) + \Gamma b_{et} G_c, \qquad 0 < x < 1 \tag{8.17}$$

$$\left.\begin{aligned} \frac{\partial j}{\partial x} &= b_{et} G_c, \\ j &= -\frac{\mathcal{B}}{\Gamma}\kappa(c)\left(\lambda\frac{\partial \hat{\phi}}{\partial x} - 2(1-t_+)\frac{\partial \log(c)}{\partial x}\right), \end{aligned}\right\} 0 < x < 1 \tag{8.18}$$

$$\left.\begin{aligned} \frac{\partial j_s}{\partial x} &= -b_{et} G_c \\ j_s &= -\frac{1}{\Theta}\frac{\partial \hat{\phi}_s}{\partial x} \end{aligned}\right\} 0 < x < 1 \tag{8.19}$$

$$c|_{x=0} = 1, \quad \hat{\phi}|_{x=0} = 0, \quad j_s|_{x=0} = 0, \tag{8.20}$$

$$\left.\frac{\partial c}{\partial x}\right|_{x=1} = 0, \quad j|_{x=1} = 0, \quad j_s|_{x=1} = -\bar{I}, \quad \left.\hat{\phi}_s\right|_{x=1} = \hat{V} - \mathcal{R}\bar{I} \tag{8.21}$$

$$c|_{t=0} = 1, \quad c_s|_{t=0} = 0.02. \tag{8.22}$$

$$G_c = \Upsilon c^{1/2}(c_s)^{1/2}(1-c_s)^{1/2}\left[\exp\left(-\frac{\lambda}{2}(\hat{\phi}-\hat{\phi}_s+\hat{U}_{eq}(c_s|_{r=1}))\right)\right.$$
$$\left.-\exp\left(\frac{\lambda}{2}(\hat{\phi}-\hat{\phi}_s+\hat{U}_{eq}(c_s|_{r=1}))\right)\right], \tag{8.23}$$

$$\mathcal{Q}\frac{\partial c_s}{\partial t} = \frac{1}{r^2}\frac{\partial}{\partial r}\left(r^2\frac{\partial c_s}{\partial r}\right), \qquad 0<r<1,\ 0<x<1 \tag{8.24}$$

$$\left.\frac{\partial c_s}{\partial r}\right|_{r=1} = -\mathcal{Q}G_c, \qquad \left.\frac{\partial c_s}{\partial r}\right|_{r=0}=0 \tag{8.25}$$

where the dimensionless parameters in the above system are defined by

$$\Gamma=\frac{LJ_0(1-t_+)}{D_0Fc_0}, \qquad \lambda=\frac{FV_0}{RT}, \qquad \mathcal{N}=\frac{a_0^2D_0}{D_{s0}L^2}, \quad \mathcal{R}=\frac{R_cJ_0A}{V_0}$$
$$\Upsilon=\frac{b_{et}kc_{max}c_0L}{J_0}, \quad \mathcal{Q}=\frac{a_0J_0}{b_{et}LFc_{max}D_{s0}}, \quad \Theta=\frac{J_0L}{\sigma_sV_0}. \tag{8.26}$$

For the interpretation of the dimensionless parameters above, we refer to Section 7.4.

Parameter Values The parameters used in the model are listed in Table 8.1. The electrolyte diffusion is taken to be at $10^{-11}m^2s^{-1}$ based on the value calculated by Owen [46], which is one order magnitude lower to the diffusion coefficient of pure $LiPF_6$ solution reported at $10^{-10}m^2s^{-1}$ by Riemers *et al.* [90]. This result suggests that the tortuosity and porosity of the composite electrode structure (where the particle sizes $< 1\mu m$) is responsible for the slower effective diffusion coefficient in the electrolyte ([46],[70]). Values for the lithium diffusion coefficient in $LiFePO_4$ have been reported by Prosini to range from $10^{-16}-10^{-14}m^2s^{-1}$ [71]. Srinivasan and Newman [84] takes the value ($10^{-18}m^2s^{-1}$) for the lithium diffusion coefficient. In the simulation, we took it to be the largest value presented by Prosini *et al.* [71] which is $10^{-14}m^2s^{-1}$. However, if we chose it to be $10^{-16}m^2s^{-1}$, we obtain the similar results. The equilibrium potential used in this model is fitted to the experimental discharge curve data provided by Srinivasan and Newman [84] where the cell is discharged at a very slow rate. The equilibrium potential curve is plotted in Figure 8.1 where the equation is given by

$$U_{eq}^*(c_s) = 3.114559 + 4.438792\ \arctan(-71.7352\,c_s+70.85337)$$
$$-4.240252\ \arctan(-68.5605\,c_s+67.730082). \tag{8.27}$$

U_{eq} is measured in Volts and c_s is the composition of y in Li_yFePO_4 (here $c_s=\dfrac{c_s^*}{c_{max}}$ and is dimensionless).

The conductivity, $\kappa(c^*)$ and the effective diffusivity, $D(c)$ were fitted to the experimental data of Riemers *et al.* [90] and are given by equation (3.72) and (3.71).

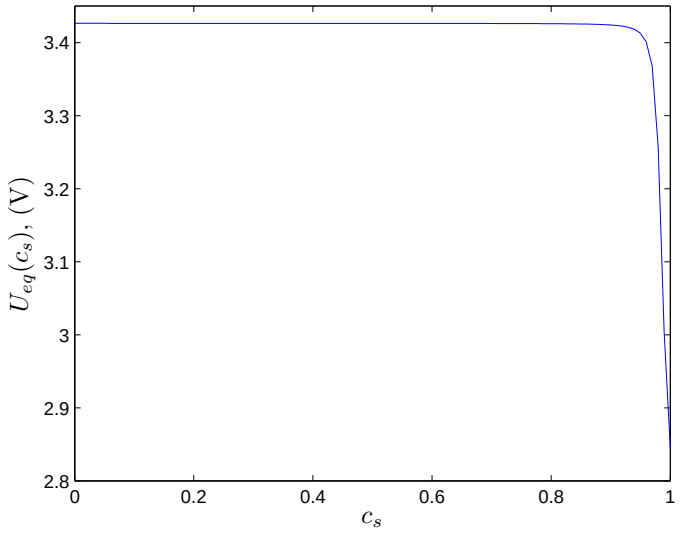

Figure 8.1: The equilibrium potential of the $LiFePO_4$ electrode as a function of c_s (the state of discharge, $c_s = c_s^*/c_{max}$) (see equation (8.27)).

Parameter	Value	Units	Reference
Electrolyte Parameters			
Diffusivity of Lithium ions, D_0	2.6×10^{-11}	$m^2 s^{-1}$	[46]
Electrode thickness, L_c	6.2×10^{-5}	m	[84]
Volume fraction, ϵ_v	0.4764	-	-
Initial salt concentration, c_0	1000	$mol m^{-3}$	[84]
Transference number, t_+^0	0.3	-	[46]
Electrode Parameters			
Reaction rate constant, k	3×10^{-12}	$m^{2.5} mol^{-0.5} s^{-1}$	[85]
Diffusion coefficient in the solid, D_{s0}	9×10^{-14}	$m^2 s^{-1}$	[71]
Particle radius, a_0	5×10^{-8}	m	[46]
Conductivity in the solid , σ_s	5×10^{-1}	$S m^{-1}$	[54]
Maximum concentration in the solid, c_{max}	18805	$mol m^{-3}$	[46]
Other Parameters			
Faraday constant, F	96487	$C mol^{-1}$	[23]
Universal gas constant, R	8.3144	$J mol^{-1} K^{-1}$	[23]
Temperature, T	298	K	[23]
Cross-sectional area of cathode , A	1×10^{-4}	m^2	[23]
Weight of $LiFePO_4$, w	7.6×10^{-3}	g	[23]
Density of $LiFePO_4$, ρ	3.6	$g cm^{-3}$	[23]
Contact resistance, R_c	6.5×10^{-3}	Ω	[23]

Table 8.1: Parameter values used in the model for $LiFePO_4$ half-cell cathode.

Following the parameter values listed in Table 8.1, the size of dimensionless parameters listed in (8.26) are given by

$$\begin{aligned} &\Gamma = 0.6242, \qquad \lambda = 77.88, \qquad \mathcal{N} = 2.7 \times 10^{-4}, \\ &\Upsilon = 30, \qquad \mathcal{Q} = 3 \times 10^{-6}, \qquad \Theta = 0.21. \end{aligned} \tag{8.28}$$

The values are calculated at $1.6C$ discharge rate in which the discharge current is $J_0 = 17Am^{-2}$ which is taken to be the base case in the simulation ($\bar{I} = 1$) and we assume the potential drop across electrode $V_0 = 2$ Volt. To run the simulation for the other discharge currents, all the dimensionless parameters remain the same except $\bar{I}$. For example; the discharge current $J_0 = 34Am^{-2}$, we set $\bar{I} = 2$ (the ratio of the discharge current to the base discharge current).

Numerical Procedure The numerical procedure implemented here is identical to that discussed in Chapter 6 and will not be repeated here.

8.3 Model-experimental comparison

In this section, we attempt to validate the results from the model developed in Chapter 3.3 with experimental data from Owen *et al.* [46]. We choose to validate against the data from [46] for several reasons. Firstly, the cathodes used by their experiments are nanostructured (size particles $< 1\mu m$) and secondly they are discharged at very high rates. This allows us to investigate the effects of electrolyte depletion on the discharge curves. The experimental results still show significant capacity even at very high discharge rates; for instance at 1110 mA/g (8C) the capacity of 28 mAh/g (20% of the total capacity) is achieved. The $LiFePO_4$ pellets are $3wt\%$ carbon coated, which gives increased electrical conductivity of the $LiFePO_4$ material on the particle scale and means that electrical conductivity (in the solid phase) is not thought to be limiting. The nanostructuring of the electrode means that transport of Lithium in the solid at the individual particle scale is very rapid and hence phase separation is negligible. The state of discharge is defined by reference to the maximum capacity ($140mAhg^{-1}$) obtained during a very slow discharge rate $C/7$.

	Discharge current	
C-rate	mAg^{-1}	$mAcm^{-2}$
$0.3C$	42	0.39
$0.81C$	112	0.86
$1.6C$	224	1.7
$3.2C$	448	3.39
$7.93C$	1110.2	7.44

Table 8.2: The discharge current rates in mAg^{-1} and $mAcm^{-2}$ units.

The results from the model compare very well to experimental data given by Owen *et al.* [46] (see Figure 8.2). The rate of current discharge for each discharge curve is listed in Table 8.2. The abrupt loss of capacity as the discharge rate increases is due to the depletion of the electrolyte near the end of discharge (see Figure 8.3). Although we remark that the smoothing of the real data curves for very large discharge rates

($8C$) in comparison to the model prediction may be because we have taken the (solid) resistance of the electrode to be small in our model (see Figure 8.2). The electrolyte depletion prevents the active material in the solid being discharged in those region in which the electrolyte has become depleted. Furthermore, when the electrolyte concentration approaches zero, the electrolyte conductivity drops (see Figure 3.3), significantly hampering discharge. Figure 8.3 shows how the electrolyte concentration approaches zero during discharge. Rapid depletion of Lithium ions in the electrolyte for the large value of dimensionless parameter Γ (appearing in (8.17)). Simultaneous with this electrolyte depletion, the Lithium intercalation process at particle surface increases very fast and gradually becomes saturated with lithium (see Figure 8.4). Figure 8.4 shows that two regions appear, one in which the electrode particles are fully discharged (full of lithium) and one in which they are not. The current tends to flow into the particles nearest the separator until they are completely discharged (full of lithium), causing the reaction to occur preferentially at the front of the electrode. Following this, a layer of discharged material then progressingly penetrates further into the electrode until all the underlying electrode material eventually becomes saturated. The discharge is thus limited both in the depletion region, due to the low lithium ion concentration, and in the saturation region where the particles are discharged. As these regions approach each other during the discharge, the electrode reaction becomes confined to a narrowing zone (see Figure 8.5), until it finally becomes impossible to discharge the electrode further.

The solid concentration across the electrode shown in Figure 8.4(a) and 8.4(b) are discharged at the rates $0.8C$ and $3.2C$ respectively. The curves represent the state of discharge of the cell with the corresponding discharge voltage plotted in Figure 8.2. The concentration curve at the last time step; this is at the position where c first drops to zero. The profiles of the lithium concentration in the electrode particles at different position are plotted in Figure 8.6. These show that the particles discharge uniformly, because diffusion of lithium in the particle is rapid compared to the diffusion of lithium ions (in the electrolyte) across the electrode.

At higher discharge current ($8C$), the low rate of transport in the electrolyte phase (see Figure 8.7) is the main factor causing the sharp drop of cell potential at a low value of electrode utilization. The concentration gradient is much steeper than the concentration profile at $3.2C$ (see Figure 8.3(b)). The electrolyte concentration goes to zero quite near the current collector, making electrode particles far from the separator impossible to access, and causing the reaction front to stop close to the separator as shown in Figure 8.8.

We emphasize here, other solid state models [84, 85, 23] explain the loss of capacity by saturation of the phase transformation. It was suggested that for thin electrodes containing large particles (about $1 - 5\mu m$) of active material the effect of particle size, solid state diffusion becomes increasingly significant compared to the limitation of electrolyte diffusion in the electrolyte phase [46]. In this work, the $LiFePO_4$ electrode is

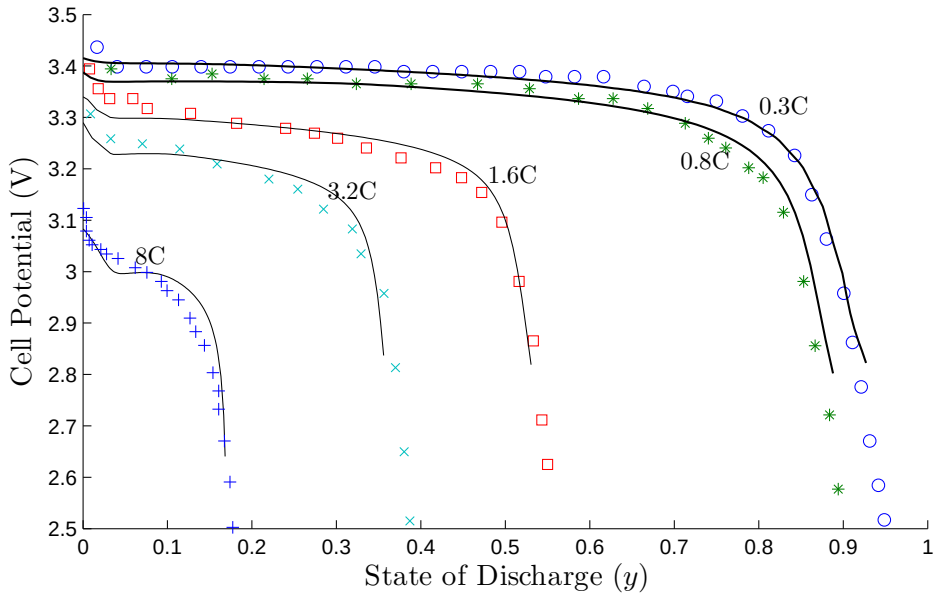

Figure 8.2: The comparison of model with the experimental data for the $LiFePO_4$ half cell discharge curves at different currents. Solid lines represent the analytic solutions and symbols represent experimental data at various discharge currents.

nano-structured and it is this that ensures that diffusion in the particle is not important due to the short diffusion timescale across a particle (lithium diffusion in the particles can be important in electrodes manufactured with large $LiFePO_4$ particles).

8.4 The effects of parameter variations on the discharge of a nanostructured half-cell cathode

In this section, we examine the effects of parameter variations specifically the solid conductivity on the discharge of a nanostructured half-cell cathode. Here we take other parameters to remain the same (refer Table 8.1 for the parameter values) and vary the solid conductivity taking it to be larger, slightly lower and significantly lower than the maximum conductivity of the electrolyte (κ_{max}). The maximum conductivity of the electrolyte ($LiPF_6$) can be extracted from Figure 3.3 (see Section 3.4), and is $\kappa_{max} = 1.1AV^{-1}m^{-1}$.

The study is useful in analysing the discharge of a nanostructured cathode and provides guidance for its design. Here we simulate the distribution of current density in the solid and in the electrolyte, solid concentration and the distribution of reaction rate at the particle surface across half-cell cathode at $1.6C$ discharge rate. Note that the plots are all dimensionless. The results are shown for three different ratios of the solid electrical conductivity ratios σ_s to the maximum conductivity in the electrolyte κ_{max}. These

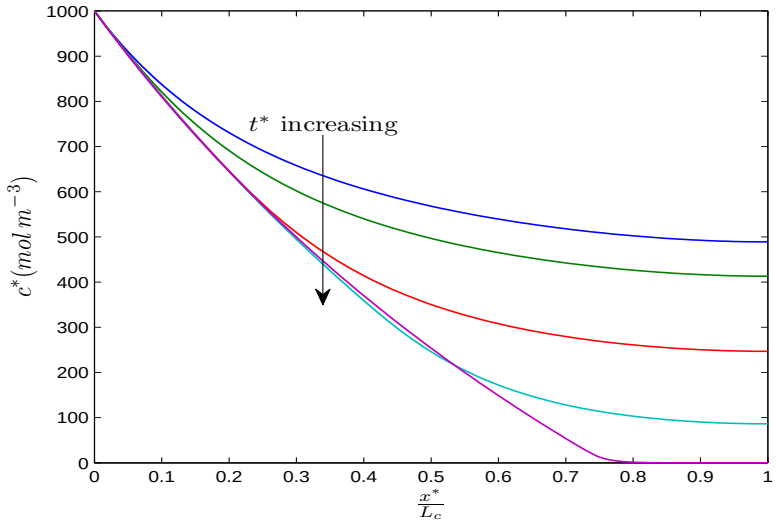

(a) $0.8C$

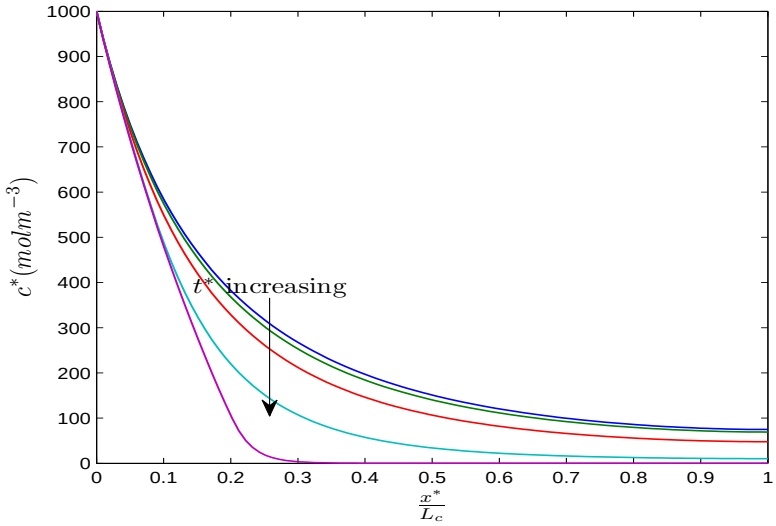

(b) $3.2C$

Figure 8.3: The concentration of solution in the electrolyte across the electrode at (a) $0.8C$ and (b) $3.2C$ discharge rate. The profiles are measured at (a) $t^* = 393s, 785s, 1178s, 1571s, 1963s$ and (b) $t^* = 162s, 325s, 487s, 585s, 650s$.

ratios are defined as follows: Case (a) $\sigma_s = 10\kappa_{max}$; Case (b) $\sigma_s = 10^{-2}\kappa_{max}$; Case (c) $\sigma_s = 10^{-4}\kappa_{max}$.

Figure 8.10 shows the solid concentration at the electrode particle surfaces (i.e $r = 1$ is dimensionless units) for different times. With $\sigma_s = 10\kappa_{max}$, the particles close to the separator are the first to discharge fully as shown in Figure 8.10(a). This indicates that the rate of intercalation in particles in this region is greater than that elsewhere. In Figure 8.10(b) the ratio of conductivity of the solid and electrolyte phase is $\sigma_s = 10^{-2}\kappa_{max}$ and the intercalation waves move from both separator and current collector.

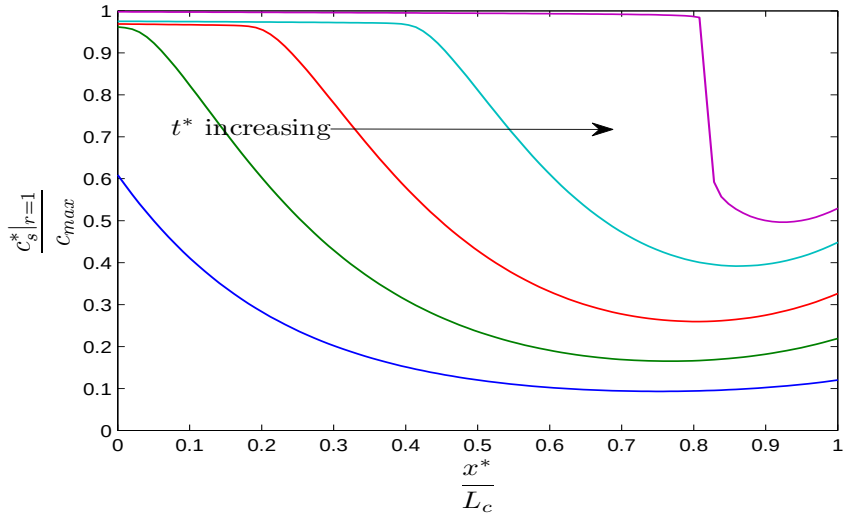

(a) $0.8C$

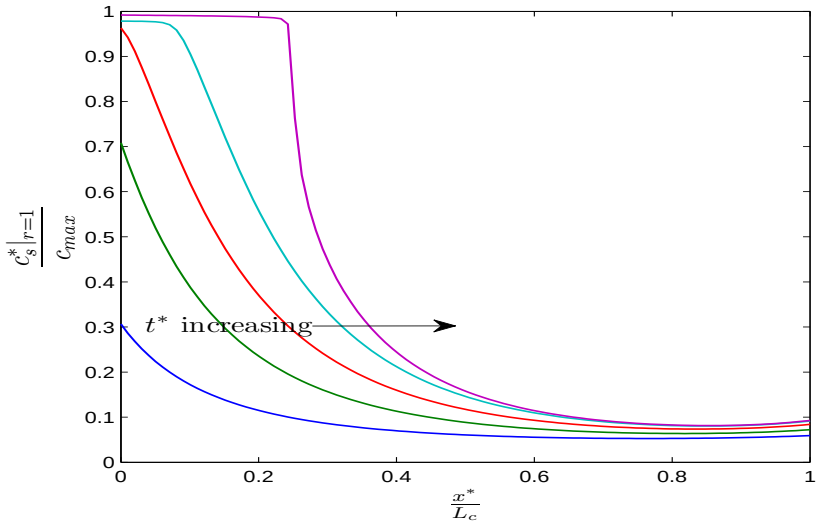

(b) $3.2C$

Figure 8.4: The concentration of Lithium in the solid at the electrode particle surfaces as a function of position in the electrode at (a) $0.8C$ and (b) $3.2C$ discharge rate. The profiles are measured at (a) $t^* = 393s, 785s, 1178s, 1571s, 1963s$ and (b) $t^* = 162s, 325s, 487s, 585s, 650s$.

When the conductivity ratio is $\sigma_s = 10^{-4}\kappa_{max}$, the intercalation wave moves in from the current collector (see Figure 8.10(c)) in reverse to the direction of propagation in Figure 8.10(a). This figure demonstrates that current tends to flow into particles near the current collector until they are completely discharged.

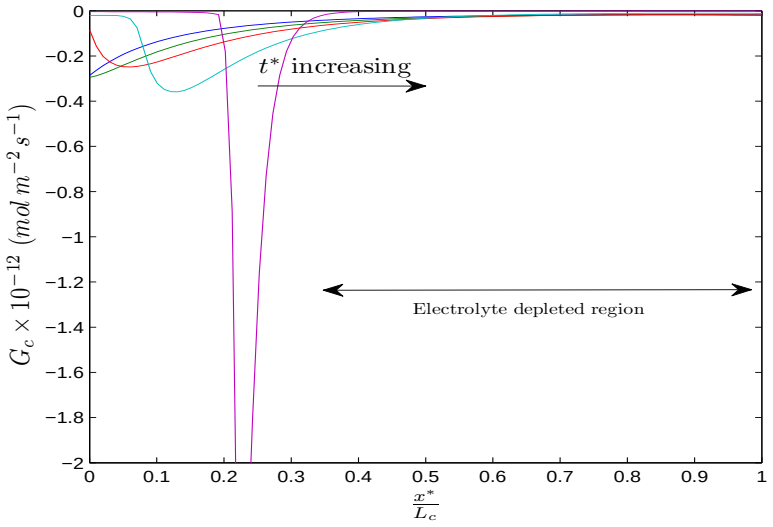

Figure 8.5: The reaction rate (per unit surface area) at the particle electrolyte interface as a function of position in the electrode for discharge at $3.2C$. The profiles are measured at $t^* = 162s, 325s, 487s, 585s, 650s$.

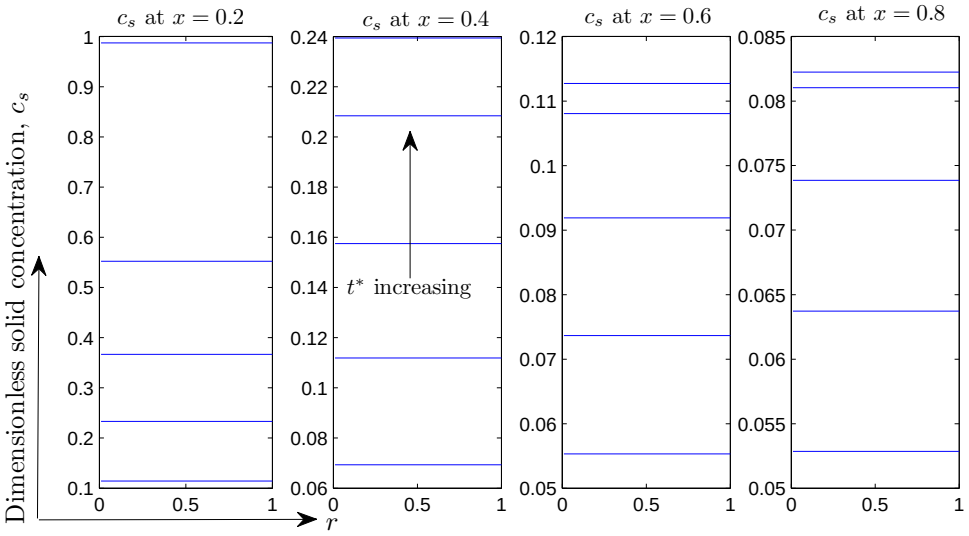

Figure 8.6: The dimensionless concentration in the electrode particle as a function of radius at different positions in the electrode for discharge at $3.2C$. The profiles are measured at $t^* = 162s, 325s, 487s, 585s, 650s$.

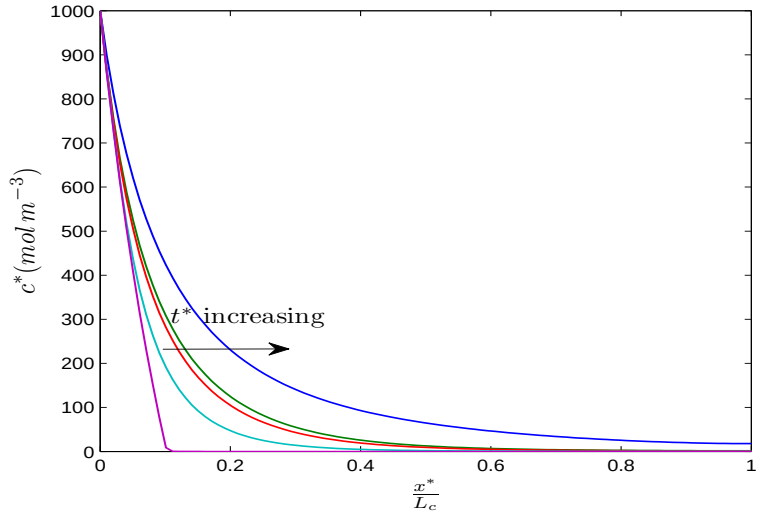

Figure 8.7: The concentration of solution in the electrolyte across the electrode at $8C$ discharge rate. The profiles are measured at $t^* = 33s, 48s, 58s, 62s, 65s$.

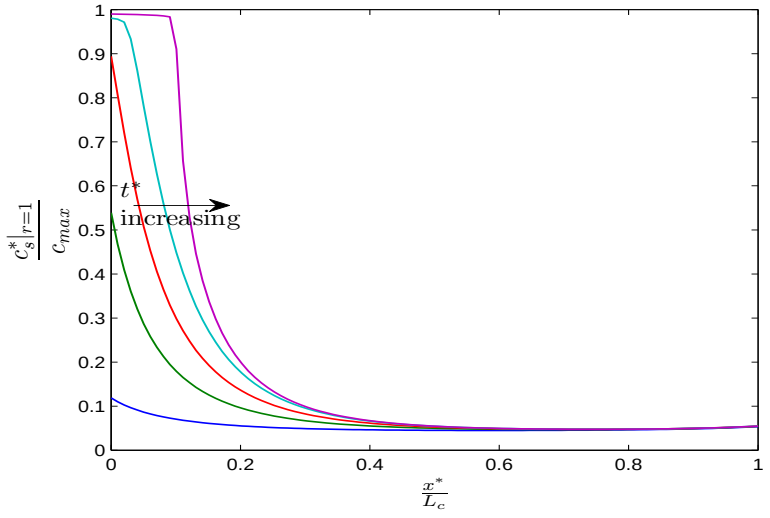

Figure 8.8: The concentration of Lithium in the solid at the electrode particle surfaces as a function of position in the electrode at $8C$ discharge rate. The profiles are measured at $t^* = 33s, 48s, 58s, 62s, 65s$.

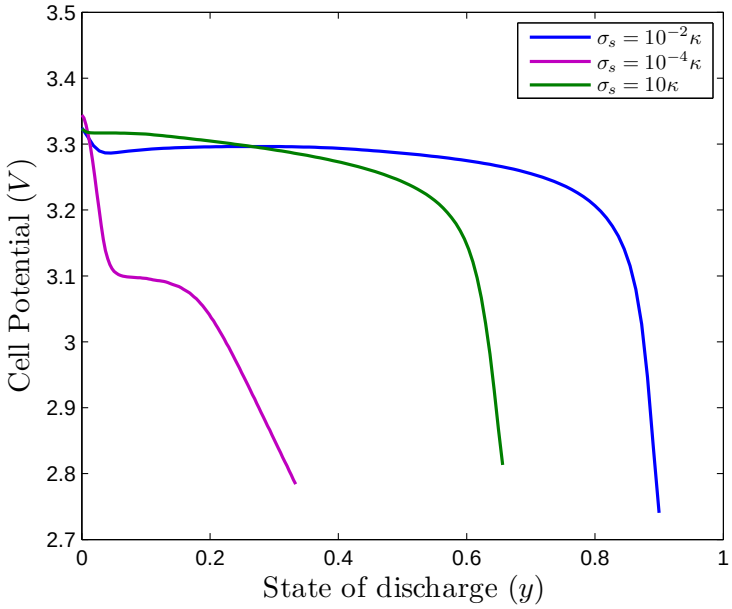

Figure 8.9: The voltage curves for different conductivity ratios in the solid (σ_s) and electrolyte (κ_{max}) phases. The cell is discharged at $1.6C$.

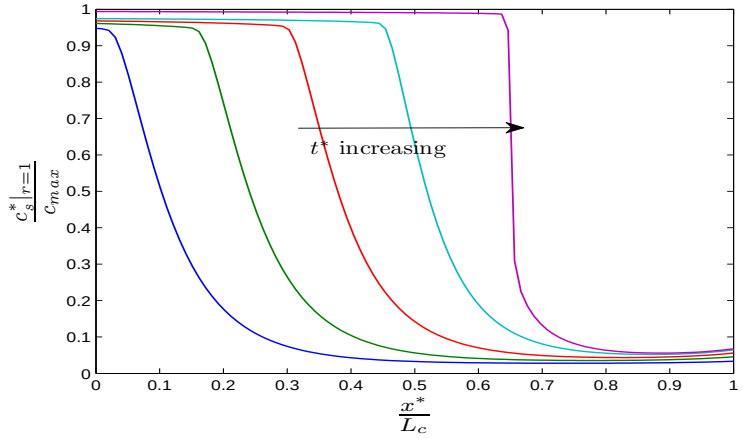

(a) $\sigma_s = 10\kappa_{max}$. $t^* = 290s, 580s, 870s, 1160s, 1450s$.

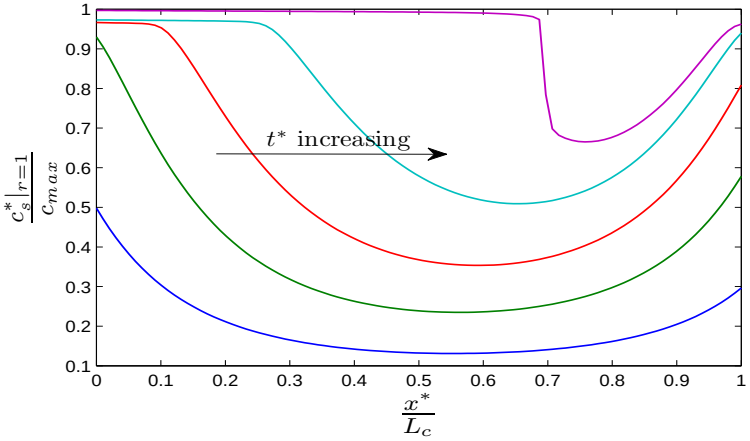

(b) $\sigma_s = 10^{-2}\kappa_{max}$. $t^* = 398s, 796s, 1194s, 1592s, 1990s$.

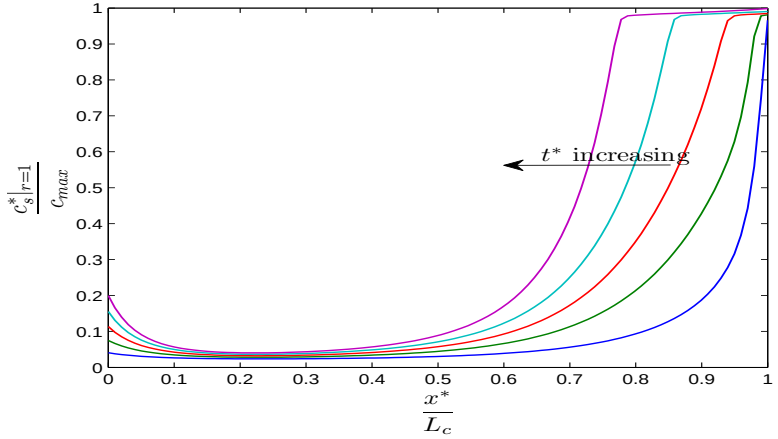

(c) $\sigma_s = 10^{-4}\kappa_{max}$. $t^* = 142s, 284s, 426s, 568s, 710s$.

Figure 8.10: The dimensionless solid concentration profiles at the electrode particle surfaces as a function of position in the electrode for different conductivity ratios in the solid (σ_s) and electrolyte (κ_{max}) phases. The cell is discharged at $1.6C$.

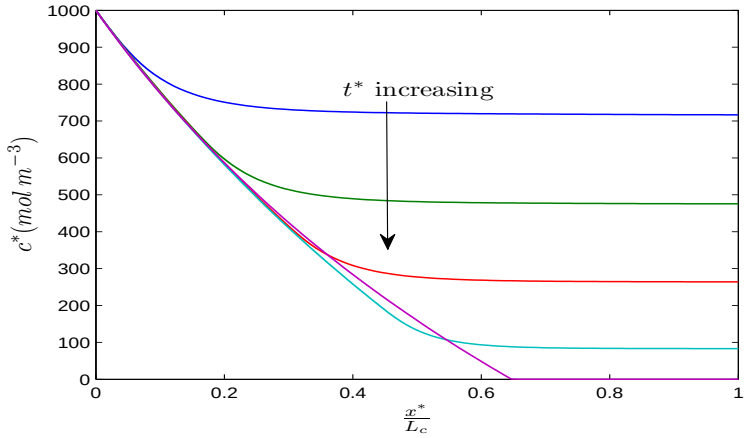

(a) $\sigma_s = 10\kappa_{max}$. $t^* = 290s, 580s, 870s, 1160s, 1450s$.

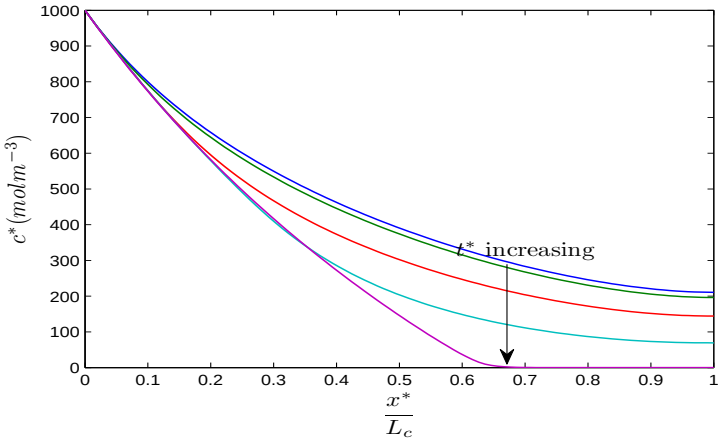

(b) $\sigma_s = 10^{-2}\kappa_{max}$. $t^* = 398s, 796s, 1194s, 1592s, 1990s$.

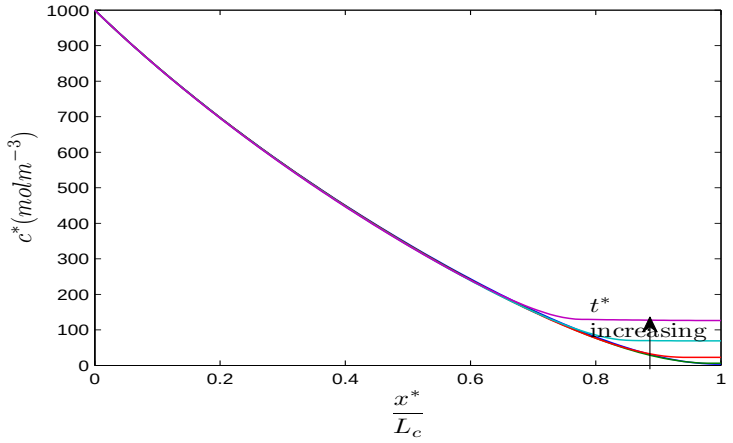

(c) $\sigma_s = 10^{-4}\kappa_{max}$. $t^* = 142s, 284s, 426s, 568s, 710s$.

Figure 8.11: The electrolyte concentration profiles across the electrode for different conductivity ratios in the solid (σ_s) and electrolyte (κ_{max}) phases. The cell is discharged at $1.6C$.

It is clearly seen that in Case (a), the electrolyte depletion near the current collector region stops the discharge before the cell can fully discharge as shown in Figure 8.11(a). In Case (b), the discharge proceeds for much longer but eventually ends, as for Case (a), when the electrolyte near the current collector becomes depleted as shown in Figure 8.11(b). On the other hand, for Case (c), the cell voltage drops very significantly (see Figure 8.9) as the intercalation wave propagates in from current collector because the resistance in the electrode is so high that current flow to the unlithiated particles near the separator causes a large ohmic loss as shown in Figure 8.11(c). In Figure 8.9, we plot the discharge curves for all 3 cases; Case (a) is limited by electrolyte depletion, Case (c) is limited by the high solid resistance while the intermediate case (Case (b)) has a significantly better discharge curve than either of the others. In some sense this is rather surprising as it suggests that making the conductivity of the electrode too good actually limits its performance.

Figure 8.12 shows that the diffusion of lithium in the solid is not important in Case (a) (see Figure 8.12(a)) and Case (c) (see Figure 8.12(b)) as the particles discharge uniformly within the solid particles. In Case (b), although it shows that the profiles are not uniform (see Figure 8.12(c)), the profiles only change by a very small amount and do not significantly affect the discharge.

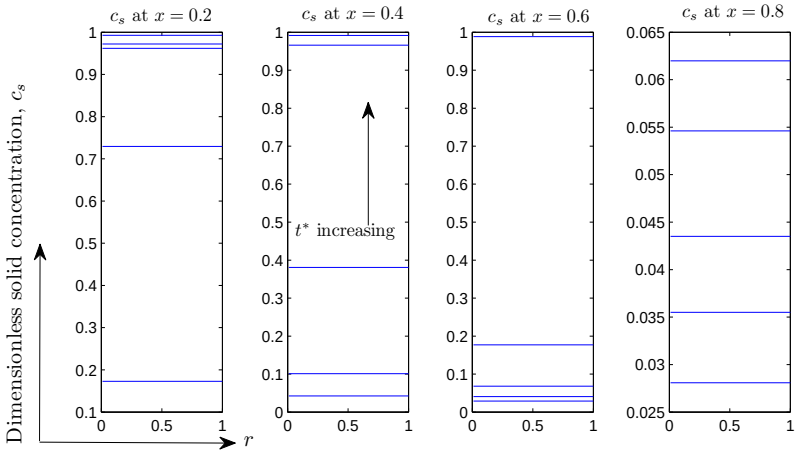

(a) $\sigma_s = 10\kappa_{max}$. $t^* = 290s, 580s, 870s, 1160s, 1450s$.

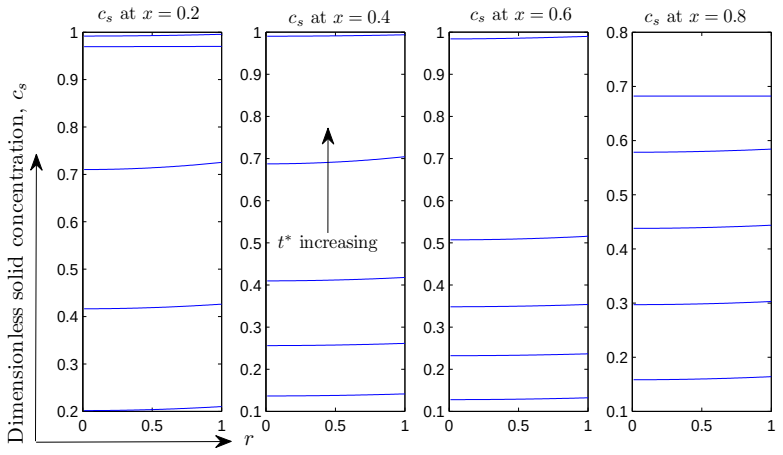

(b) $\sigma_s = 10^{-2}\kappa_{max}$. $t^* = 398s, 796s, 1194s, 1592s, 1990s$.

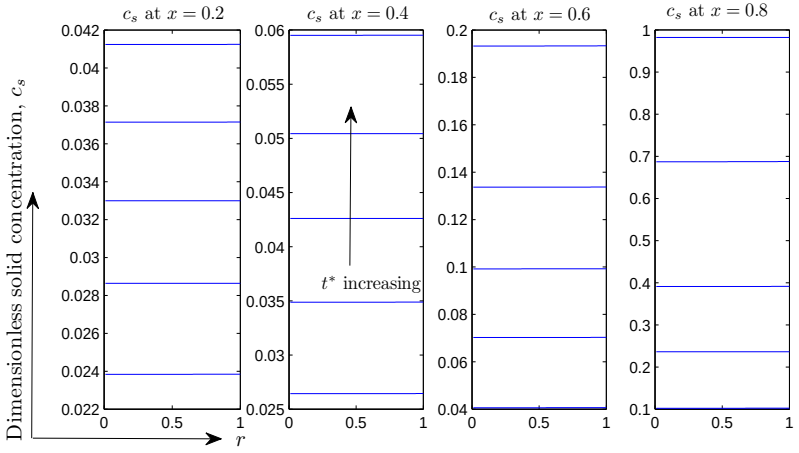

(c) $\sigma_s = 10^{-4}\kappa_{max}$. $t^* = 142s, 284s, 426s, 568s, 710s$.

Figure 8.12: The dimensionless solid concentration profiles in the electrode particles as a function of radius at different positions when the cell is discharged for the 3 different cases. The cell is discharged at $1.6C$.

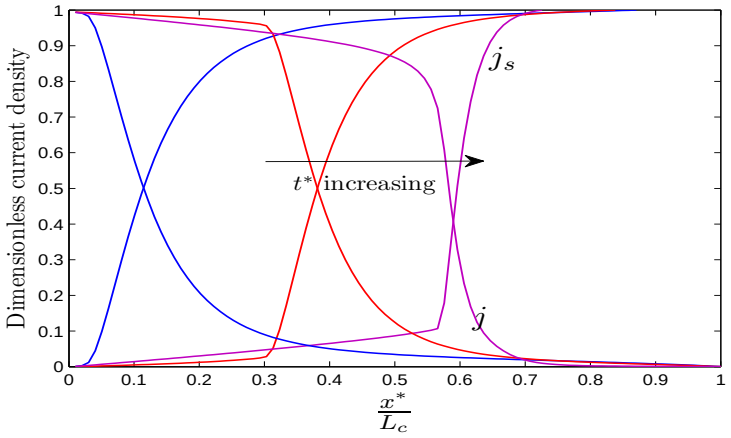

(a) $\sigma_s = 10\kappa$. $t^* = 290s, 870s, 1450s$.

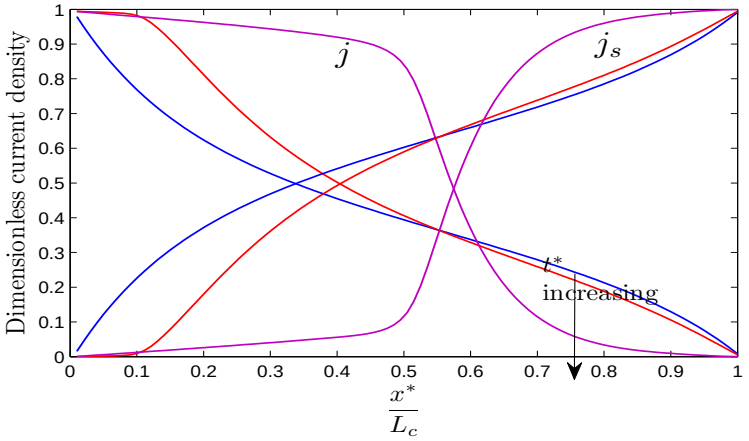

(b) $\sigma_s = 10^{-2}\kappa$. $t^* = 398s, 1194s, 1990s$.

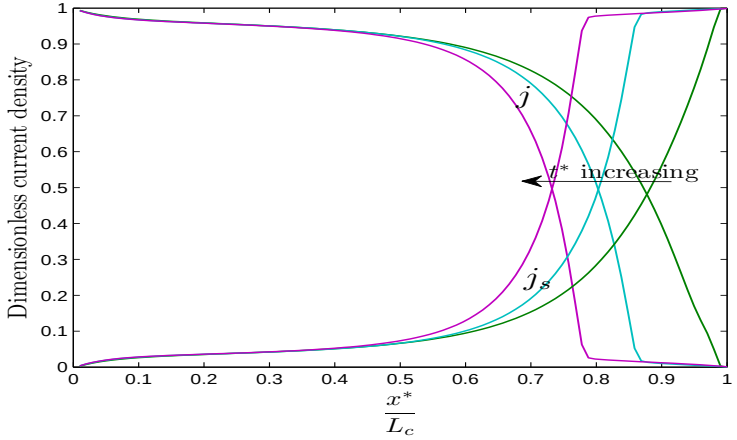

(c) $\sigma_s = 10^{-4}\kappa$. $t^* = 284s, 568s, 710s$.

Figure 8.13: The distribution of dimensionless current density in the solid (j_s) and in the electrolyte (j) across the cathode for different conductivity ratios in the solid (σ_s) and electrolyte (κ) phases. The cell is discharged at $1.6C$.

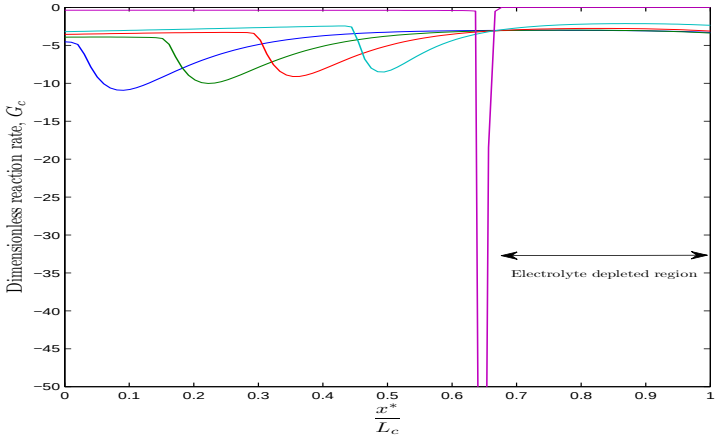

(a) $\sigma_s = 10\kappa_{max}$. $t^* = 290s, 580s, 870s, 1160s, 1450s$.

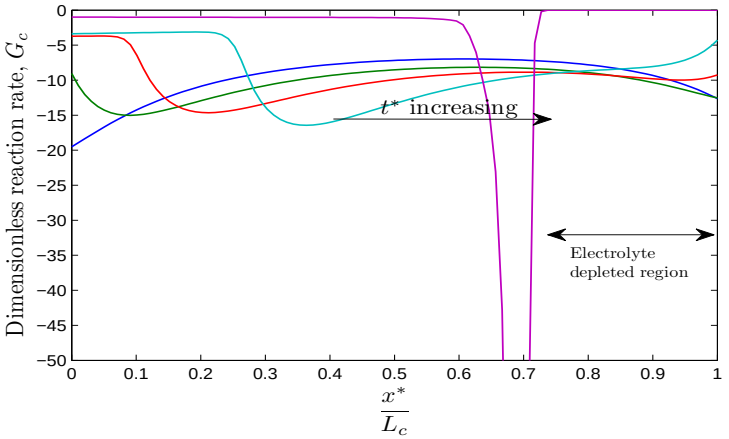

(b) $\sigma_s = 10^{-2}\kappa_{max}$. $t^* = 398s, 796s, 1194s, 1592s, 1990s$.

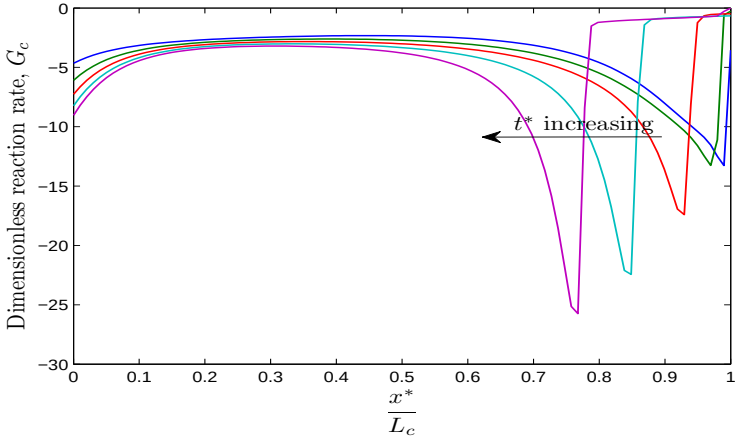

(c) $\sigma_s = 10^{-4}\kappa_{max}$. $t^* = 142s, 284s, 426s, 568s, 710s$.

Figure 8.14: The dimensionless reaction rate (G_c) across the cathode for different conductivity ratios in the solid (σ_s) and electrolyte (κ_{max}) phases. The cell is discharged at $1.6C$.

Figure 8.13 shows the distribution of current density in the solid (j_s) and in the electrolyte (j) across the cathode in the 3 different cases. For $\sigma_s = 10\kappa_{max}$, the current density profiles propagate in from the separator (see Figure 8.13(a)). In Figure 8.13(b), for $\sigma_s = 10^{-2}\kappa_{max}$, the current density profiles propagate in from both separator and current collector and for $\sigma_s = 10^{-4}\kappa_{max}$ (see Figure 8.13(c)), the current density profiles propagate in from the current collector. Figure 8.14 shows the reaction rate distribution across the cathode in the 3 different cases. The reaction rate peaks move from the separator towards the current collector in Case (a) (see Figure 8.14(a)) while the trend is reversed in Case (c) (see Figure 8.14(c)). In Case (b), the peaks can be seen to propagate in from both separator and current collector (see Figure 8.14(b))).

Figure 8.15 shows the curves for the current density in the electrolyte when the cell is discharged at $1.6C$ for $400s$ under different conductivity ratios in the solid and electrolyte phases. When $\sigma_s = 10\kappa_{max}$, the crucial region of the current distribution is near the separator. The current drops in this region indicate that the current travels only a short distance from separator before being intercalated in the electrode particle. When $\sigma_s = 10^{-2}\kappa_{max}$, the current distribution is more uniform; showing that a significant numbers of Lithium ions are intercalated in the regions near the separator and near the current collector. However, when $\sigma_s = 10^{-4}\kappa_{max}$, the significant drop in current occurs near the current collector. As the conductivity in the solid is very small, it is difficult for current to travel far from current collector.

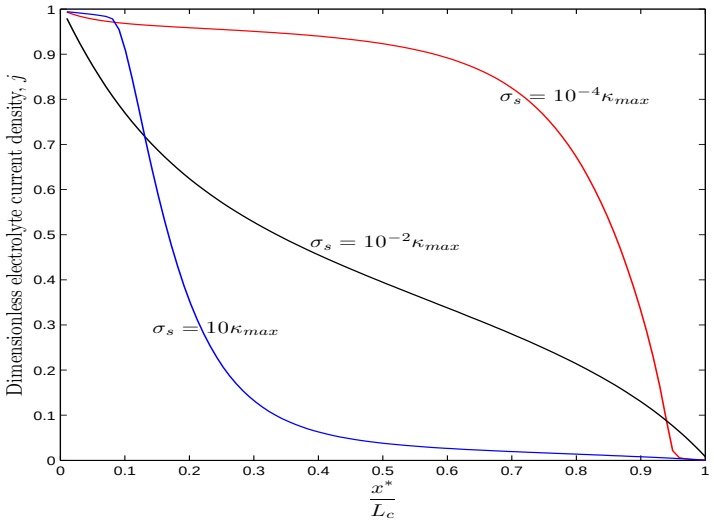

Figure 8.15: Distribution of the dimensionless electrolyte current density (j) across the electrode when the cell is discharged at $1.6C$ for $400s$ with different conductivity ratios in the solid (σ_s) and electrolyte (κ_{max}) phases.

Figure 8.16 shows the distribution of reaction rates when the cell is discharged at $1.6C$ for $400s$ for the three different cases. For Case (a) $\sigma_s = 10\kappa_{max}$, the peak in reaction rate occurs near the separator ; for Case (b) $\sigma_s = 10^{-2}\kappa_{max}$, the reaction peaks occur

at both the separator and the current collector; and, for Case (c) $\sigma_s = 10^{-4}\kappa_{max}$, the reaction peak occurs near the current collector.

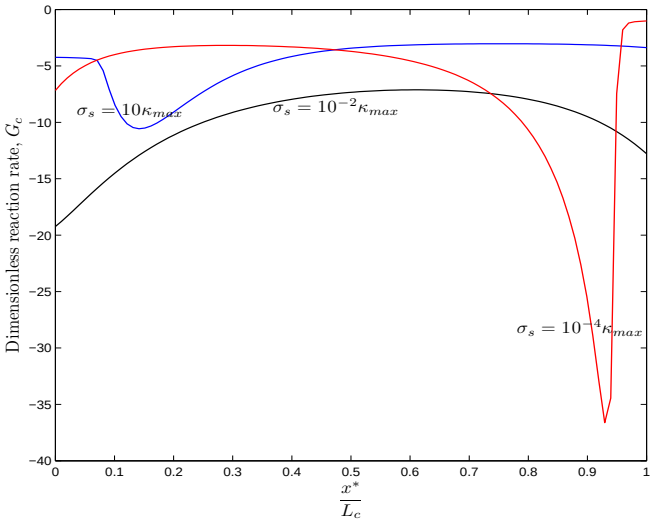

Figure 8.16: The dimensionless reaction rate across cathode when the cell is discharged at $1.6C$ for $400s$ with different conductivity ratios in the solid (σ_s) and electrolyte (κ_{max}) phases.

8.5 Summary

A half cell model is presented for a $LiFePO_4$ cathode. The model treats the electrolyte using moderately concentrated solution theory. The simulation results presented in this chapter compare well to the experimental data from Owen *et al.* [46] across a range of discharge rates. We show that at high discharge rates, the ionic diffusivity in the $LiPF_6$ electrolyte limits the discharge of a the half cell as a result of the formation of lithium depleted regions in the electrolyte.

In this study, we also investigate the effects that varying the ratio of conductivity in the solid to that the maximum conductivity in the electrolyte has on discharge. The results show that if the ratio is large, the current distribution propagate in from the separator; if the ratio is slightly low, the current distribution propagate in from both the separator and current collector; and if the ratio is very low, the current distribution propagate in from the current collector. Interestingly, the best discharge curve is obtained for the intermediate value of the conductivity ratio between electrolyte and solid phases (10^{-2}) as shown in Figure 8.9. High solid conductivity leads to electrolyte depletion while low solid conductivity results in high resistance in the solid and a poor discharge curve. This study may have bearing on the efficient design of electrodes for high discharge applications.

Chapter 9

Conclusions and Future Works

9.1 Conclusions

A general introduction to the electrochemical process occurring in a battery was presented in Chapter 1 together with a review of battery modelling over the past few decades including the framework set out by Newman [59].

In Chapter 2, we discussed solutions to a detailed model of a lithium-ion battery based on a dilute electrolyte model and fast diffusion in the electrode particles. The extremely small size of electrode particles led us to use the homogenisation battery model derived in [74]. We derived quasi static asymptotic solutions to this homogeneous model based on flat discharge curves for the electrode materials. These asymptotic solutions were found to compare favourably to numerical solutions.

Interaction between ions in more concentrated solutions leads to non-ideal behaviour and in Chapter 3 we discuss an electrolyte model for moderately concentrated electrolyte (based on the Stefan Maxwell equations) that was originally presented in [60]. We note a source of confussion is the factor premultiplying the concentration term in Ohm's law is accounted for by the fact that potentials in this model are measured with respect to a lithium electrode rather than the absolute potential. The transport properties appearing in the model are then fitted to experimental data. Homogenisation techniques are applied to the electrolyte model in a battery and it is shown how to derive a macroscopic model parameter (the porosity) that accounts for the microscopic structure of the electrodes. Hence the model could be used to compare the cell performance of different microstructures with different shapes and sizes of particle.

In Chapter 5, we discussed the modelling of electrode particle of graphite anode particles (LiC_6) and Lithium iron phosphate ($LiFePO_4$) cathode particles. The models described are based on diffusion equations for lithium in the electrode particles. So for

example the multiple phase transition that occur as lithium intercalate in LiC_6 are described by a nonlinear diffusion model (as shown in Chapter 7) which provides a good phenomenological description of the behaviour.

A numerical procedure based on the method of lines (MOL) was developed in Chapter 6 to solve the multiscale battery problem consisting of macroscopic electrolyte equations and microscopic diffusion equations for lithium transport in the electrode particles. This procedure is discussed. The MOL technique is well-suited to relatively stiff equations and works by converting the set of PDEs into a large set of coupled ODEs system. An implicit differential algebraic solver; namely ode15s is used to solve this large system of ODEs. The resulting code is fast, efficient and stable. Furthermore, it can be readily adapted for use in more complicated scenarios; such as electrodes with different sizes and shapes of particle.

The model was verified against experiment in Chapters 7 and 8. In Chapter 7, we discussed the half cell discharge on an Li_xC_6 anode. This is limited by diffusion of lithium in the electrode particles. In order to accurately reproduce the discharge curves we needed to account for the strong dependence of diffusivity within the particles on lithium concentration. An analytic asymptotic solution for the potential drop V across the cell was derived in the limit that the diffusion timescale in the electrolyte is small in comparison to the lithium diffusion timescale in the electrode particles. In this limit, it is shown that the electrode particles discharge synchronously.

In Chapter 8, we formulated a model for nanostructured $LiFePO_4$ half cell cathode in which we assumed that the diffusion within the electrode particles is sufficiently fast that discharge is limited solely by the electrolyte and the conductivity of the electrode. The numerical results of this model compared very favourably against real data from a half cell $LiFePO_4$ cathode measured by Owen *et al.* [46]. We then investigated how varying the electrode conductivity in the simulation affected the discharge curves (see Figure 8.9). We found that the best discharge curve was obtained at an intermediate values of the electrolyte conductivity. This seems to be because the discharge is affected by electrolyte depletion if the conductivity in the solid is large and by high solid resistance if the conductivity in the solid is too small. We believe that the results may prove useful in electrode design.

9.2 Future works

The research can be further developed in a number of ways;

The effect of different sizes of particles In this study, we assume that the electrode particles are all spheres of uniform sizes. However, in actual batteries, the particles may be of different sizes (and of shapes) and hence will encounter different diffusion and surface reaction rates. The model remains unchanged, except that different size particles may have different BET surface area if they are packed similarly. However, lithium diffusion in large particles is slower than in small particles, and this may lead to nonuniform current distribution. Our numerical procedure is capable of simulating this problem with only minor modifications. Thus, it would be interesting to investigating the effect of varying the distribution of particle sizes in space upon the cell performance.

The effect of changes in particle shape and packing upon cell performance Here we have always assumed the electrode particles to be spherical in order to simplify the theoretical treatment. To date, no comprehensive numerical investigation has been performed to investigate the effects of changes in particle shape and packing upon cell performance. Once again the numerical procedure gives here should be capable of being adapted to non-spherical particles although this involves the introduction of extra dimensions. So for example a general ellipsoidal particle requires treatment in those spatial directions r_1, r_2, r_3 but one with an axis of symmetry only requires treatment in two spatial; directions r_1 and r_2.

References

[1] Aihara Y., Bando T., Nakagawa H., Yoshida H., Hayamizu K., Akiba E., Price W. S., "Ion Transport Properties of Six Lithium Salts Dissolved in γ-Butyrolactone Studied by Self-Diffusion and Ionic Conductivity Measurements." *J. Electrochem. Soc.*, **151**(1), A119-A122 (2004).

[2] Allen J.L., Jow T.R., Wolfenstine J. (2007), "Kinetic study of the electrochemical $FePO_4$ to $LiFePO_4$ phase transition". *Chem. Mater.*. **19**(8), 2108-2111.

[3] Allen J.L., Jow T.R., Wolfenstine J. (2008), "Analysis of the $FePO_4$ to $LiFePO_4$ phase transition". *J. Solid State Electrochem.* **12**(7), 1031-1033.

[4] Atkins, P., and de Paula, J., (2001), "Physical Chemistry". *OUP*, Seventh Edition.

[5] Bai P., Cogswell D.A., Bazant M.Z. (2011), "Suppression of phase separation in $LiFePO_4$ nanoparticles during battery discharge". *Nano Letters*, 11(11), 4890-4896.

[6] Bazant M., (2011), "V. Electrostatics Lecture, 24: Diffuse Charge in Electrolytes" for MIT Student.

[7] Bockris J.O'M., Reddy A. K. N., Gamboa-Aldeco M., (2000), "Modern Electrochemistry 2A.", *Kluwer Academic/Plenum Publishers*, Second Edition.

[8] Bothe D., (2011), "On the Maxwell-Stefan approach to multicomponent diffusion". *Springer Basel*, 81-93.

[9] Botte G.G., Subramaniam V.R., White R.E., (2000), "Mathematical modeling of secondary lithium batteries.", *Electrochemica Acta*, **45**(15), 2595-2609.

[10] Bruce P.G., Scrosati B., Trascon J.M., (2008), "Nanomaterials for rechargeable lithium batteries.", *Angew. Chem. Int. Ed.*, **47**(16), 2930-2946.

[11] Bruce P. G., (2008), "Energy storage beyond the horizon: Rechargeable lithium batteries." *Solid State Ionics*, **179**(21), 752-760.

[12] Bruna M., (2013), Unpublished work, Personal Communications.

[13] Buqa H., Goers D., Holzapfel M., Spahr M.E., Novak P., (2005), "High Rate Capability of Graphite Negative Electrodes for Lithium-Ion Batteries". *J. Electrochem. Soc.*. **152**(2), A474-A481.

[14] Carmelo S., Domenico D., Giovanni F., Anna S., (2009), "Experimental identification and validation of an electrochemical model of a Lithium-Ion Battery." Proceedings of the *American Control Conference*.

[15] Chabot V., Farhad S., Chen Z., Fung A.S., Yu A., Hamdullahpur F., (2013). "Effect of electrode physical and chemical properties on lithium-ion battery performance." *Int. J. Energy Research*, **37**(14), 17231736.

[16] Chandrasekaran R., (2010). "Modeling of electrochemical energy storage and energy conversion devices." PhD Thesis., Georgia Institute of Technology.

[17] Chen G., Song X., Richardson T. J. (2007), "Metastable Solid Solution Phases in the LiFePO4/FePO4 System". *J. Electrochem. Soc.*, **154**(7), A627-A632.

[18] Chueh W.C., Gabaly F.E., Sugar J.D., Bartelt N.C., McDaniel A.H., Fenton K.R., Zavadil K.R., Tyliszczak T., Lai W. & McCarty K.F., (2013), "Intercalation Pathway in Many-Particle LiFePO4 Electrode Revealed by Nanoscale State-of-Charge Mapping." *Nano Letters* **13**(3), 866-872.

[19] Ciucci F., Lai W.,(2011), "Derivation of Micro/Macro Lithium Battery Models from Homogenization." *Transp. Porous Med.* **88**(2), 249-270.

[20] Cole J.D., (1995), "Limit process expansions and homogenization." SIAM J.Appl. Maths. 55(2), 410-424.

[21] Damian Burch, (2009)."Intercalation Dynamics in Lithium-Ion Batteries." *Massachusetts Institute of Technology*, PhD Thesis.

[22] Daniel C., "Materials and Processing for Lithium-ion Batteries." *Journal of Metals*, **60**(9), 43-48.

[23] Dargaville S., Farrell T.W., Troy W. (2010) "Predicting active material utilisation in $LiFePO_4$ electrodes using a multi-scale mathematical model." *J. Electrochem. Soc.*, **157**(7), A830-A840.

[24] Dargaville S. (2013), "Mathematical Modelling of LiFePO4 Cathodes." *Queensland University of Technology*, PhD Thesis.

[25] Darling R., Newman J(1997) "On the short-time behavior of porous intercalation electrodes." *J. Electrochem. Soc.*, **144**(9), 3057-3063.

[26] Delmas C., Maccario M., Croguennec L., Le Cras F., Weill F., (2008), "Lithium deintercalation in LiFePO4 nanoparticles via a domino-cascade model." *Nature materials: Macmillan Publishers Ltd.*, **7**(8), 665-671.

[27] Doeff M.M, Edman L., Sloop S.E, Kerr J., De Jonghe L.C., (2000). "Transport properties of binary salt polymer electrolytes". *J. Power Source*, **89**(2). 227-231.

[28] Doyle M, Fuller T.F., and Newman J. (1993) "Modeling of galvanostatic charge and discharge of the lithium-polymer-insertion cell". *J. Electrochem. Soc.*, **140**(6), 1526-1533.

[29] Doyle C.M. (1995). "Design and Simulation of Lithium Rechargeable Batteries.", *Lawrence Berkeley National Laboratory* , PhD thesis.

[30] Doyle M, Newman J., Gozdz A.S., Schmutz C.N., Trascon J.M., (1996) "Comparison of modeling predictions with experimental data from plastic lithium ion cells". *J. Electrochem. Soc.*, **143**(6), 1890-1903.

[31] Doyle M, and Newman J. (1997) "Analysis of capacity rate data for lithium batteries using simplified models of the discharge process." *J. Appl. Elecrochem.*, **27**(7), 846-856.

[32] Doyle M., Fuentes Y. (2003). "Computer Simulations of a Lithium-Ion Polymer Battery and Implications for Higher Capacity Next-Generation Battery Designs." *J. Electrochem. Soc.*, **150**(6), A706-A713.

[33] Ellis B.L., Lee K.T., Nazar L.F., (2010), "Positive electrode materials for Li-ion and Li-batteries." *Chem. Mater.*, *22*(3), 691-714.

[34] Fauteux D. (1988), "Lithium electrode/PEO-based polymer electrolyte interface behavior between $60^{O}C$ and $120^{O}C$".*J. Electrochem. Soc.*, **135**(9), 2231-2237.

[35] Ferguson T.R., Bazant M.Z.,(2014), "Phase transformation dynamics in porous battery electrodes." *Electrochimica Acta*, **146**, 89-97.

[36] Fuller T.F., Doyle M., Newman J., (1994). "Simulation and optimisation of the dual lithium ion insertion cell." *J. Electrochem. Soc.*, **141**(1), 1-10.

[37] Fuller T.F., Doyle M. and Newman J., (1994). "Relaxation phenomena in lithium-ion insertion cells." *J. Electrochem. Soc.*, **141**(4), 982-990.

[38] Funabiki A., Inaba M., Ogumi Z., Yuasa S., Otsuji J., Tasaka A., (1998), "Impedance study of the electrochemical lithium intercalation into natural graphite powder." *J. Electrochem. Soc.*, *145*(1), 172-178.

[39] Garcia, R.E., Chiang Y.M., Carter W.C., Limthongkul P., Bishop C.M., (2005) "Microstructural modeling and design of rechargeable Lithium-ion batteries." *J. Electrochem. Soc.*, **152**(1), A255-A263.

[40] Gogi K. Singh G.K., Ceder G., Bazant M.Z., (2008). "Intercalation dynamics in rechargeable battery materials: General theory and phase-transformation waves in $LiFePO_4$". *Electrochimica Acta*, **53**(26), 7599-7613.

[41] Golmon S., Maute K., Dunn M.L, (2009). "Numerical Modeling of electrochemical-mechanical interactions in lithium polymer batteries". *Computer and Structure*, **87**(23), 1567-1579.

[42] Gully A., Liu H., Srinivasan S., Sethurajan A. K., Schougaard S., Protasa B., (2014), "Effective Transport Properties of Porous Electrochemical Materials A Homogenization Approach." *J. Electrochem. Soc.*, *161*(8), E3066-E3077.

[43] Joachin H., Kaun T.D., Zaghib K., (2009), PrakashaJ., "Electrochemical and Thermal Studies of Carbon-Coated LiFePO4 Cathode." *J. Electrochem. Soc.*, *156*(6), A401-A406.

[44] Johansen J.F., Farrell T.W., Please C.P., (2006). "Modelling of primary alkaline battery cathodes: A simplified model". *J. Power Source*, **156**(2), 645-654.

[45] John F., (1982), "Partial Differential Equations', **Springer-Verlag**, 4th edition.

[46] Johns P.A., Roberts M.R., Wakizaka Y., Sanders J.H., Owen J.R., (2010) "How the electrolyte limits fast discharge in nanostructured batteries and supercapacitors." Electrochem. Comm., 11(11), 2089-2092.

[47] Kang Xu., (2004). "Nonaqueous Liquid Electrolytes for Lithium-Based Rechargeable Batteries." *Chem. Rev.*, **104**(10), 4303-4417.

[48] Lee H. H., Wan C. C., Wang Y. Y., (2004), "Thermal Stability of the Solid Electrolyte Interface on Carbon Electrodes of Lithium Batteries." *J. Electrochem. Soc.*, **151**(4), A542-A547.

[49] Levi M.D., Aurbach D.,(1997), "Diffusion Coefficients of Lithium ions during intercalation into graphite derived from the simultaneous measurements and modeling of electrochemical impedance and potentiostatic intermittent titration characteristics of thin graphite electrodes." *J. Phys. Chem.*, *101*(23), 4641-4647.

[50] Ma Y.,Doyle M, Fuller T.F., Doeff M.M., De Jonghe L.C., Newman J., (1995) "The measurement of a complete set of transport properties for a concentrated solid polymer electrolyte solution". *J. Electrochem. Soc.*, **142**(6), 1859-1868.

[51] Mackenzie D., (2010)., "Fill'er Up with . . . Lithium." *SIAM News*, **43**(2).

[52] Malik R., Abdellahi A., Ceder G.,(2013), "A Critical Review of the Li Insertion Mechanisms in LiFePO4 Electrodes." *Journal of The Electrochem. Soc.*, **160**(5), A3179-A3197.

[53] Methekar R. N., Northrop P. W. C., Chen K., Braatz R. D., Subramanian V.R. (2011). "Kinetic Monte Carlo Simulation of Surface Heterogeneity in Graphite Anodes for Lithium-Ion Batteries: Passive Layer Formation." *J. Electrochem. Soc.*, **158**(4), A363-A370.

[54] Ming W. , Jun L. J., Ming H. X., Han W., Rong W. C.,(2012), "The effect of local current density on electrode design for lithium-ion batteries." *J. Power Sources*, **207**, 127-133.

[55] Nalin A.C., Reinhardt K., Jake C., Jasim A., Aleksandar K., (2010). "Modelling, estimation, and control challenges for lithium-ion batteries". *American Control Conference*(ACC), IEEE.

[56] Newman J., (1968), "Numerical Solution of Coupled, Ordinary Differential Equations". *Ind. Eng. Chem. Fundamentals*, 2nd Ed. **7**(3). 514-517.

[57] Newman J., Tiedemann W., (1975), "Porous-electrode theory with battery applications". *AlChE Journal*, **21**(1), 251.

[58] Newman J.S., (1991), "Electrochemical systems.", *Prentice Hall*, New Jersey, 2nd edition.

[59] Newman J. Thomas K.E., Hafezi H., Wheeler D.R., (2003), "Modeling of lithium-ion batteries". *J. Power Sources*, **119**, 838-843.

[60] Newman J., Thomas-Alyea K.E. (2004) "Electrochemical Systems". *Wiley Inter-Science*, Third Edition.

[61] Ning G., White R.E., Popov B.N. (2006), "A generalized cycle life model of rechargeable Li-ion batteries". *Electrochimica Acta*, **51**(10), 2012-2022.

[62] NuLi Y., Yang J., Jiang Z., (2006), "Intercalation of lithium ions into bulk and powder highly oriented pyrolytic graphite." *J. Physics & Chemistry of Solids*, **67**(4), 882-886.

[63] Orvanosos B., Ferguson T.R., Yu H.C., Bazant M.Z., Thornton K. (2014), "Particle-level modeling of the charge-discharge behavior of nanoparticulate phase-separating Li-ion battery electrodes". *J. Electrochem. Soc.*, **161**(4), A535-A546.

[64] Owen J.R., (1997), "Rechargeable lithium batteries." Chem. Soc. Rev. 26(4), 259-267.

[65] Padhi A.K., Nanjundaswamy K.S., Goodenough J.B., (1997) "Phospho-olivines as positive electrode materials for rechargeable lithium batteries". *J. Electrochem. Soc.*, **144**(4), 1188-1194.

[66] Padhi A.K., Nanjundaswamy K.S., Goodenough J.B.. (1997), "Mapping of transition metal redox energies in phosphates with NASICON structure by lithium intercalation". *J. Electrochem. Soc.*, **144**(8),2581-2586.

[67] Palacin M.R. (2009). "Recent advances in rechargeable battery materials: a chemist's perspective". *Chemical Society Reviews.* **38**(9), 2565-2575.

[68] Park M., Zhang X., Chung M., Lessa G.B., Sastry A.M.,(2010), "A review of conduction phenomena in Li-ion batteries." *J. Power Source*, *195*(24), 79047929.

[69] Perrson K., Sethuraman V.A., Hardwick L.J., Hinuma Y., Meng Y.S., Ven A.V., Srivinasan V., Kostecki R., Ceder G., (2010), "Lithium diffusion in graphitic carbon." *J. Phys. Chem. Lett.*, **1**(8), 1176-1180.

[70] Phillip J.A., (2011), "Investigations of Rate Limitation in Nanostructured Composite Electrodes and Experiments Towards a 3D Li-ion Microbattery", *Uni. of Southampton*, PhD Thesis.

[71] Prosini P.P., Lisi M., Zane D., Pasquali M., (2002) "Determination of the chemical diffusion coefficient of lithium in LiFePO4." *Solid State Ionics*, **148**(1-2), 45-51.

[72] Ramadass P., Haran B., Parthasarathy M. G., White R.E. , Popov B.N., (2004). "Development of First Principles Capacity Fade Model for Li-Ion Cells." *J. Electrochem. Soc.*, **151**(2), A196-A203.

[73] Richardson G., King J.R. (2006). "Time-dependant modelling and asymptotic analysis of electrochemical cell". *J. Eng. Math.* **59**(3), 239-275.

[74] Richardson G., Denuault G. and Please C.P., (2012). "Multiscale modelling and analysis of lithium-ion battery charge and discharge." *J. Eng. Math.* **72**(1), 4172.

[75] Richardson G., (2012), Personal Communication

[76] Roscher M.A., Bohlen O., Vetter J.,(2011), "OCV hysteresis in Li-ion batteries including two-phase transition materials." *Int. J. Electrochem.*, ID:984320.

[77] Safari M., Delacourt C., (2011) "Simulation-based analysis of ageing phenomena in a commercial graphite/$LiFePO_4$ cell". *J. Electrochem. Soc.*, **158**(12), A1436-A1447.

[78] Samson E., Lemaire G., Marchand J., Beaudoin J.J., (1999), "Modeling chemical activity effects in strong ionic solutions." *Computational Materials Science*, **15**(3), 285-294.

[79] Shampine, L. F., Reichelt M. W., (1997), "The MATLAB ODE Suite," *SIAM Journal on Scientific Computing*, **18**(1), 1-22.

[80] Shen J. D., and Sun K. (2012), "Microstructural design considerations for Li-ion battery systems." *Solid State and Materials Science* **16**(4), 153-162.

[81] Shim J., Striebel K. A.,(2003), "Cycling performance of low-cost lithium ion batteries with natural graphite and LiFePO4." *J. Power Sources*, *119*, 955958.

[82] Shukla A.K., Kumar T.P., (2008), "Materials for Next- Generation Lithium Batteries," *Curr. Sci.*, **94**(3), 314-331.

[83] Smith K.A., Rahn C.D., Wang C.Y., (2007), "Control oriented 1D electrochemical model of lithium ion battery." *Energy Conversion and Management*, **48**(9), 2565-2578.

[84] Srivinasan V., Newman J., (2004), "Discharge model for the lithium iron-phosphate electrode". *J. Electrochem. Soc.*, **151**(10). A1517-A1529.

[85] Srivinasan V., Newman J., (2004), "Design and optimization of a natural graphite/-iron phosphate Lithium-ion cell". *J. Electrochem. Soc.*, **151**(10), A1530-A1538.

[86] Stephenson D.E., Walker B.C., Skelton C.B., Gorzkowski E. P., Rowenhorst D.J., Wheeler D.R., (2011) "Modeling 3D microstructure and ion transport in porous Li-ion battery electrodes." *J. Electrochem. Soc.*, **158**(7). A781-A789.

[87] Takami N., Satoh A., Hara M., Ohsaki T., (1995), "Structural and Kinetic Characterization of Lithium Intercalation into Carbon Anodes for Secondary Lithium Batteries." *J. Electrochem. Soc.*, **142**(2), 371-379.

[88] Tarascon J.M., Armand M.,(2001), "Issues and challenges facing rechargeable lithium batteries." *Nature: Macmillan Magazines Ltd.*, *414*

[89] Thomas K.E., (2002), "Thermal Modeling of Batteries with Porous Insertion Electrodes." **University of Berkeley**, PhD Thesis.

[90] Valoen L.O., Reimers J.N. (2005), "Transport properties of $LIPF_6$-based Li-ion battery electrolytes".*J. Electrochem. Soc.*, **152**(5), A882-A891.

[91] Verbrugge M. W., Koch B. J., (2003), "Electrochemical Analysis of Lithiated Graphite Anodes." *J. Electrochem. Soc.*, **150**(3), A374-A384.

[92] Wang C.Y., Gu W.B., Liaw B.Y., (1998), "Micro-macroscopic coupled modeling of batteries and fuel cells." *J. Electrochem. Soc.* **145**(10), 3407-3417.

[93] Whitaker S., (1998), "The Method of Volume Averaging (Theory and Applications of Transport Porous Media).", *Springer, Berlin*, 1st edition.

[94] White R.E., (1978), "On Newmans Numerical Technique for Solving Boundary Value Problems." *Ind. Eng. Chem. Fundam.*, **17**(4), 367-369.

[95] Whittingham M.S., (2004) "Lithium Batteries and Cathode Materials." *Chem. Rev.* **104**(10), 4271-4301.

[96] Wilson J.R., Cronin J.S., Barnett S.A. & Harris S.J., (2011) "Measurement of three-dimensional microstructure in a $LiCoO_2$ positive electrode." *J. Power Sources*, **196**(7), 3443-3447.

[97] Wua H., Cuia Y.,(2012), "Designing nanostructured Si anodes for high energy lithium ion batteries."*NanoToday* *7*(5), 414-429.

[98] Xiao J., Xu W., Wang D., Choi D., Wang W., Li X., Graff G.L., Liu J., Zhang J.G., (2010), "Stabilization of Silicon Anode for Li-Ion Batteries." *Journal of The Electrochemical Society*, **157**(10), A1047-A1051.

[99] Yu P., Popov B.N., Ritter J.A., White R.E., (1999) "Determination of the Lithium Ion Diffusion Coefficient in Graphite". *J. Electrochem. Soc.*, **146**(1), 8-14.

[100] Zeng Y., Bazant M.Z. (2012), "Cahn-Hilliard Reaction model for isotropic Li-ion battery particles". *Chem. Mater.*. **19**, 2108-2111.

[101] Zeng Y. Bazant M.Z. (2014), "Phase separation dynamics in isotropic ion-intercalation particles". *SIAM J. App. Math.*, **74**(4), 980-1004 .

[102] Zhang X. (2009). "Multiscale modeling of Li-ion cels: Mechanics, heat generation and electrochemical kinetics". *University of Michigan*, PhD thesis.

[103] Zhu M., Park J., Sastry A. M.,(2011)."Particle Interaction and Aggregation in Cathode Material of Li-Ion Batteries: A Numerical Study." *Journal of The Electrochemical Society*, **158**(10), A1155-A1159.